DEFECT REDUCTION STUDY OF MOLECULAR BEAM EPITAXIALLY GROWN CdTe THIN FILMS BY EX-SITU ANNEALING

A Thesis Submitted to

the Graduate School of Engineering and Sciences of

Izmir Institute of Technology

in Partial Fulfillment of the Requirements for the Degree of

MASTER OF SCIENCE

ın Physics

by

Emine BAKALİ

October 2015

İZMİR

We approve the thesis of **Emine BAKALİ**

Examining Committee Members:

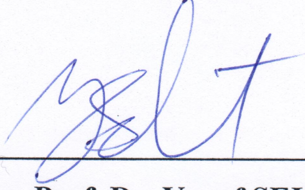

Assoc. Prof. Dr. Yusuf SELAMET
Department of Physics, Izmir Institute of Technology

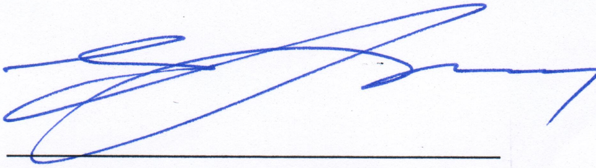

Assist. Prof. Dr. Enver TARHAN
Department of Physics, Izmir Institute of Technology

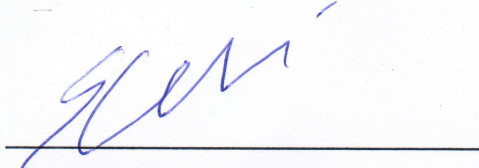

Prof. Dr. Erdal ÇELİK
Department of Metallurgical and Materials Engineering, Dokuz Eylül University

23 October 2015

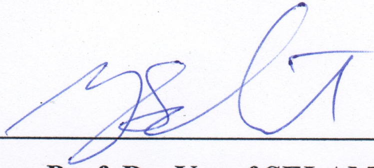

Assoc. Prof. Dr. Yusuf SELAMET
Supervisor, Department of Physics
Izmir Institute of Technology

Prof. Dr. Nejat BULUT
Head of the Department of Physics

Prof. Dr. Bilge KARAÇALI
Dean of the Graduate School of
Engineering and Sciences

ACKNOWLEDGMENTS

I wish to express my sincere gratitude to Prof. Yusuf SELAMET, my respective advisor, who has always been sincere, helpful in making me solve the different problems. To study with his, interesting, enjoyable and full of surprises.

I would like to thank to Prof. Enver TARHAN for many useful suggestions, advice and dictations about this theses and Raman Spectroscopy.

I would like to acknowledge to Prof. Orhan ÖZTÜRK for being elder brother and forcing me to be brave.

I like to thank to Prof. George PETTERSON and Prof. John RENO for teaching me MBE.

I am very thankful Elif BILGILISOY, who helped me etch pit decorations in this thesis and she helped me every problem about this study. Also she companion me. I want to thank Gündoğdu ŞAHIN for teaching me using of Raman spectroscopy. I want to thank Hasan AYDIN, who taught me using of AFM.

I would like to thank to Mr. Gökhan ERDOĞAN and Ms. Duygu OĞUZ KILIÇ, they taught me using of SEM. Also I would like to acknowledge all of IZTECH MAM members for sharing knowledge all thinks.

I acknowledge members of my defense committee; Prof. Yusuf SELAMET, Prof. Erdal ÇELİK and Prof. Enver TARHAN.

I would like to acknowledge to Elif ÖZÇERİ, who introduce me Lab and taught me basics of lab.

I would like to thank to my office friends; Sevil ALTUĞ, Hakan ALABOZ, Nazir İBRAHİM. They have helped me always.

I would like to thank my group members; Alper YANILMAZ, Atike İNCE YARDIMCI, Mustafa POLAT, Sinem DUMAN, Begüm Yavaş, Nesli TEKGÜZEL YAĞMURCUKARDEŞ, Merve KARAKAYA and Ozan ARI.

I would like to acknowledge to SSM and ASELSAN as a financial support.

ABSTRACT

DEFECT REDUCTION STUDY OF MOLECULAR BEAM EPITAXIALLY GROWN CdTe THIN FILMS BY EX-SITU ANNEALING

Molecular Beam Epitaxy (MBE) grown CdTe thin films were annealed in this study to decrease the number density of defects. For annealing, a system was designed and constructed. During anneals; anneal temperature, anneal time, anneal cycle and hydrogen gas effects were analyzed. The effects of annealing parameters were analyzed by Scanning Electron Microscope (SEM), Atomic Force Microscope (AFM), Everson Etch method, resonance Raman spectroscopy and Photoluminescence measurement.

In our studies, dislocation density decreased for 5 min. annealing when annealing temperature increased. Dislocation density decreased with increasing annealing time. Besides, dislocation density decreased when cycle number increased. Te precipitation decreased with annealing. Raman mode at 144 cm^{-1} was investigated and that mode was decided as Te E mode. Also I_{2LO}/I_{LO} ratio decreased with increasing annealing temperature and annealing time. I_{2LO}/I_{LO} ratio were approached to 1 at 80°K due to so called ‘resonance Raman scattering’. Extra peaks were also observed by Raman scattering. On the surface, small pits occurred when annealing temperature increased. Surface roughness decreased with increasing cycle number.

ÖZET

MOLEKÜLER DEMET EPİTAKSİYEL BÜYÜTÜLEN CdTe İNCE FİLMLERİNİN TAVLAMA İLE KUSUR AZALTMA ÇALIŞMASI

Büyütme sırasında oluşan kusurları azaltmak için, Moleküler Demet Epitaksi (MBE) ile büyütülen CdTe ince filmler tavlandı. Tavlama için bir sistem tasarlandı. Tavlamalar sırasında; tavlama sıcaklığı, tavlama süresi, tavlama devri ve hidrojen gazı etkileri incelendi. Tavlama parammetreleri etkileri Taramalı Uç Mikroskobu (SEM), Atomik Kuvvet Mikroskobu (AFM), Everson eç metodu, resonans Raman Spektroskopisi ve fotoluminesans ölçümleri ile incelendi.

Araştırmalar sonucunda 5 dakika boyunca tavlanan örneklerde dislokasyon yoğunluğu tavlama sıcaklığı artarken düşmüştür. Dislokasyon yoğunluğu tavlama süresi arkarken düşmüştür. Ayrıca tavlama devri artarken dislokasyon yoğunluğu düşmüştür. Te çökeltisi tavlamalar sonuda azalmıştır. 144 cm^{-1} deki raman modu Te E moduna ait olduğu kararlaştırılmıştır. I_{2LO}/I_{LO} oranı tavlama sıcaklığı ve tavlama süresi artarken düşmüştür ve rezonans Raman saçılmasında I_{2LO}/I_{LO} oranı 80°K de 1'e yaklaşmıştır. Raman saçılmalarında yeni pikler gözlemlenmiştir. Sıcaklık artarken örnek yüzeyinde küçük çukurlar oluşmuştur. Yüzey pürüzlülüğü tavlama devri artığında düşmüştür.

I have dedicated

This study

To My FAMILY

TABLE OF CONTENTS

LIST OF FIGURES viii

CHAPTER 1. INTRODUCTION 1

CHAPTER 2. EXPERIMENTAL TECHNIQUES 6

2.1. CdTe Thin Films Growth by MBE 6

2.2. CdTe Thin Films Annealing by Home Made Quartz System 8

2.3. Raman Characterization 13

2.4. SEM Characterization 16

2.5. AFM Characterization 17

2.6. Defect Decoration Method 18

CHAPTER 3. RESULTS AND DISCUSSION 19

3.1. Annealing Under Vacuum 19

3.1.1. Effects of Annealing Temperature 19

3.1.2 Effects of Annealing Time 41

3.1.3 Effects of Annealing Cycle 51

3.2. Annealing Under Hydrogen Atmosphere 66

CHAPTER 4. CONCLUSIONS 73

REFEREENCES 75

APPENDIX A. MORE RAMAN SPECTRA 78

LIST OF FIGURES

Figure **Page**

Figure 1. Dislocation density as a function of DCRC FWHM of HgCdTe/CdTe/GaAs [4]. 1

Figure 2. a) R_oA_j as a function of EPD, b) 1/f noise current at 1 Hz as a function of EPD at 78K, c) Quantum efficiency as a function of EPD at 78 K and d) Short circuit current density at 78 K as a function of EPD [5]. 2

Figure 3. A schematic representation of MBE a) top view and b) side view. 7

Figure 4. During the growth sample of G3AA-CT9 time versus temperature graph. 8

Figure 5. A photograph of the designed annealing system. 9

Figure 6. The Si sample heater. 9

Figure 7. The temperature calibration graph. First point correspond In melting point, second point, third point, and fourth point corresponds melting points of Se, Zn, Al respectively. 10

Figure 8. Mass flowmeter of H_2 gas calibration. 10

Figure 9.Temperature profile of CT9-2-AN10. 11

Figure 10. Temperature profile of CT9-2-AN30 sample. 11

Figure 11. Schematic diagram of Raman Spectroscopy system. 13

Figure 12. As grown CT9-2 sample's Raman spectra at different temperature. 14

Figure 13. After the background correction as-grown CT9-2 sample's Raman spectra at different temperature. 15

Figure 14. Fitted Raman spectra of CT9-2-an13 sample at 80 K. 15

Figure 15. Schematic diagram of SEM system. 16

Figure 16. Schematic diagram of AFM system. 17

Figure 17. Everson etch steps. 18

Figure 18. SEM micrograph of annealed for 5 min. a) as-grown CT9-2, b) CT9-2-AN2 annealed at 190ºC c) CT9-2-AN9 annealed at 390ºC, d) CT9-2-AN6 annealed at 400ºC, e) CT9-2-an7 annealed at 410ºC, f) CT9-2-AN8 annealed at 420ºC, and g) CT9-2-AN3 annealed at 485ºC samples. 20

Figure 19. Etched by Everson method a) CT9-2-AN2-E, b) CT9-2-AN17-E, c) CT9-2-AN9-E, d) CT9-2-AN6-E, e) CT9-2-AN7-E, f) CT9-2-AN8-E, g) CT9-2-AN4-E and h) CT9-2-AN3-E samples. 21
Figure 20. Dislocation densities as a function of annealing temperature. Annealing was for 5 min. 22
Figure 21. Raman shifts as a function of annealing temperature. Raman measurement were done at 80 K. 22
Figure 22. Raman shifts of phonon modes as a function of measurement temperature for 5 min annealed samples at 7 different temperature. 23
Figure 23. Variation of FWHM value of Te A_1, 144, LO and 2LO phonon modes of for 5 min. annealed samples. 24
Figure 24. Plot of CdTe phonon modes $I_{Te\ A1}/I_{LO}$ ratios as a function of annealing temperature of annealed for 5min. 24
Figure 25. Graph of I_{144}/I_{LO} ratio as a function of annealing temperature. Raman measurement was done with cooling from 296 K to 80 K. 25
Figure 26. 3D graph of CdTe Raman spectroscopy result's 2LO/LO ratios changing with annealing temperature and Raman measurement temperature. 26
Figure 27. CT9-2-AN19 annealed at 350°C; a) 2D AFM image, b) 3D AFM image. CT9-2-AN21 annealed at 415°C c) 2D AFM image, d) 3D AFM image. CT9-2-AN23 annealed at 500°C e) 2D AFM image, f) 3D AFM image. CT9-2-AN22 annealed at 550°C g) 2D AFM image, h) AFM 3D image. 27
Figure 28. Surface roughness for 5 min. annealed samples as a function of annealing temperature obtained from 10x10 um^2 and 1x1 um^2 area. 28
Figure 29. Etched by Everson method a) CT9-2-AN19-E, b) CT9-2-AN20-E, c) CT9-2-AN21-E, d) CT9-2-AN25-E, e) CT9-2-AN26-E, f) CT9-2-AN23-E, g) CT9-2-AN24-E and h) CT9-2-AN22-E. 29
Figure 30. Dislocation densities as a function of annealing temperature. Annealing was for 5 min. 30
Figure 31. Raman shifts as a function of annealing temperatures. Raman measurement were done at 80 K and annealing time was 5 min. 30

Figure 32. Raman shifts of Te A_1, 144 cm^{-1}, LO and 2LO phonon modes as a function of measurement temperature for 5 min. annealed samples at 7 different temperature. 31
Figure 33. Variation of FWHM value of Te A_1, 144 cm^{-1}, LO and 2LO phonon modes for 5 min. annealed samples. 31
Figure 34. Plot of optic phonon modes $I_{Te\ A1}/I_{LO}$ ratios as a function of annealing temperature of annealed for 5min. 32
Figure 35. Graph of I_{144}/I_{LO} ratio as a function of annealing temperature. Raman measurement was done with cooling from 296 K to 80 K. 33
Figure 36. 3D graph of CdTe Raman spectroscopy result's 2LO/LO ratios changing with annealing temperature and Raman measurement temperature. 33
Figure 37. SEM micrograph of annealed for 20 min. a) CT9-2-AN35 at 180°C, b) CT9-2-AN36 at 300°C, c) CT9-2-AN37 at 350°C and d) CT9-2-AN28 at 420°C samples. 34
Figure 38. Annealed at 190°C for 20 min. CT-2-AN35 sample's a) 2D AFM image, b) 3D AFM image. Annealed at 300°C for 20 min. CT9-2-AN36 sample's c) 2D AFM image, d) 3D AFM image. Annealed at 350°C for 20 min. CT9-2-AN37 sample's e) 2D AFM image, f) 3D AFM image. Annealed at 420°C for 20 min. CT9-2-AN28 sample's g) 2D AFM image and h) 3D AFM image. 35
Figure 39. Surface roughness of for 20 min. annealing as a function of annealing temperature from 10x10 um^2 and 1x1 um^2 area. 36
Figure 40. Etched by Everson method a) CT9-2-AN35-E, b) CT9-2-AN36-E, c) CT9-2-AN37-E and d) CT9-2-AN28-E. 36
Figure 41. Dislocation densities as a function of annealing temperature. Annealing was for 20 min. 37
Figure 42. Raman shifts as a function of annealing temperature. Raman measurement were done at 80 K and annealing time was 20 min. 38
Figure 43. Raman shifts of Te A_1, 144 cm^{-1}, LO and 2LO phonon modes as a function of measurement temperature for 20 min annealed samples at 7 different temperature. 38

Figure 44. Variation of FWHM value of Te A_1, 144 cm^{-1}, LO and 2LO phonon modes for 20 min. annealed samples. 39
Figure 45. Plot of optic phonon modes $I_{Te\ A1}/I_{LO}$ ratios as a function of annealing temperature of annealed for 20 min. 39
Figure 46. Graph of I_{144}/I_{LO} ratio as a function of annealing temperature. Raman measurement was done with cooling from 296 K to 80 K. 40
Figure 47. 3D graph of CdTe Raman spectroscopy result's 2LO/LO ratios changing with annealing temperature and Raman measurement temperature. 40
Figure 48. SEM micrograph of annealed at 400°C a) CT9-2-AN6 for 5 min., b) CT9-2-AN10 for 10 min. and c) CT9-2-AN11 for 20 min. 41
Figure 49. Etched by Everson method a) CT9-2-AN6-E, b) CT9-2-AN10-E, c) CT9-2-AN11-E samples. 42
Figure 50. Dislocation densities as a function of annealing time. Annealing was at 400°C. 42
Figure 51. Raman shifts as a function of annealing time of annealed samples at 400°C. Raman measurements were done at 80 K. 43
Figure 52. Raman shifts of Te A_1, 144 cm^{-1}, LO and 2LO phonon modes as a function of measurement temperature of annealed samples at 400 °C. 43
Figure 53. Variation of FWHM value of Te A_1, 144 cm^{-1}, LO and 2LO phonon modes of annealed samples at 400°C. 44
Figure 54. Plot of optic phonon mode's $I_{Te\ A1}/I_{LO}$ ratios as a function of annealing time of annealed at 400°C. 45
Figure 55. Graph of I_{144}/I_{LO} ratio as a function of annealing time. Raman measurements were done with cooling from 296 K to 80 K. 45
Figure 56. 3D graph of CdTe Raman spectroscopy result's 2LO/LO ratios changing with annealing time and Raman measurement temperature. 46
Figure 57. SEM micrograph of annealed samples at 420°C a) CT9-2-AN32 for 10 min. and b) CT9-2-AN28 for 20 min. 46
Figure 58. a) AFM 2D images from 10x10um^2 area of CT9-2-AN32 and b) AFM 2D from 10x10 um^2 area image of CT9-2-AN28 samples. 47
Figure 59. Surface roughness of annealed samples at 420°C as a function of annealing time from 10x10 um^2 and 1x1 um^2 area. 47

Figure 60. Dislocation densities as a function of annealing time. Annealing was at 420°C. 48
Figure 61. Raman shifts as a function of annealing time of annealed samples at 420°C. Raman measurement were done at 80 K. 48
Figure 62. Raman shifts of Te A_1, 144 cm^{-1}, LO and 2LO phonon modes as a function of measurement temperature of annealed samples at 420 °C. 49
Figure 63. Variation of FWHM value of Te A_1, 144 cm^{-1}, LO and 2LO phonon modes of annealed samples at 420°C. 49
Figure 64. Plot of optic phonon mode's $I_{Te\ A1}/I_{LO}$ ratios as a function of annealing time of annealed at 420°C. 50
Figure 65. Graph of I_{144}/I_{LO} ratio as a function of annealing time. Raman measurement was done with cooling from 296 K to 80 K. 50
Figure 66. 3D graph of CdTe Raman spectroscopy result's 2LO/LO ratios changing with annealing time and Raman measurement temperature. 51
Figure 67. SEM micrograph of cyclic annealed at 420°C with keeping total anneal time 20 min. a) 1 cycle CT9-2-AN28, b) 2 cycle CT9-2-AN29, c) 4 cycle CT9-2-AN30, and d) 8 cycle CT9-2-AN31 samples. 52
Figure 68. AFM images of cyclic annealed at 420°C samples from 10x10 um^2 area with keeping total annealing time 20 min. a) CT9-2-AN28 for 1 cycle, b) CT9-2-AN29 for 2 cycle, c) CT9-2-AN30 for 4 cycle and d) CT9-2-AN31 for 8 cycle. 53
Figure 69. Surface roughness of annealed samples at 420°C as a function of annealing number of cycle from 10x10 um^2 and 1x1 um^2 area. 53
Figure 70. Etched by Everson method for cyclic annealed samples with keeping total time at 20 min. a) CT9-2-AN28-E, b) CT9-2-AN29-E, c) CT9-2-AN30-E and d) CT9-2-AN31-E samples. 54
Figure 71. Dislocation densities as a function of annealing cycle. Annealing was at 420°C and total annealing time was 20 min. 54
Figure 72. Raman shifts as a function of number of annealing cycle at 420°C. Total annealing time was 20 min. Raman measurement temperature were done at 80 K. 55

Figure 73. Raman shifts of Te A_1, 144 cm^{-1}, LO and 2LO phonon modes as a function of measurement temperature of cyclic annealed samples at 420 ^oC for 20 min total annealing time. 56
Figure 74. Variation of FWHM value of Te A_1, 144 cm^{-1}, LO and 2LO phonon modes of cyclic annealed samples during 20 min. at 420^oC. 56
Figure 75. Plot of optic phonon mode's $I_{Te\ A1}/I_{LO}$ ratios as a function of annealing cycle of annealed at 420^oC during 20 min. 57
Figure 76. Graph of I_{144}/I_{LO} ratio as a function of annealing cycle. Raman measurement was done with cooling from 296 K to 80 K. 57
Figure 77. 3D graph of CdTe Raman spectroscopy result's 2LO/LO ratios changing with annealing cycle and Raman measurement temperature. 58
Figure 78. Photoluminescence spectra of cycle annealed samples at 80 K. Total anneal time was 20 min. Laser source was 488 nm. 58
Figure 79. SEM micrograph of cyclic annealed samples at 420^oC with keeping total annealing time 10 min. a) CT9-2-AN32 for 1 cycle, b) CT9-2-AN33 for 2 cycle, and c) CT9-2-AN34 for 4 cycle. 59
Figure 80. AFM images of cyclic annealed samples at 420^oC with keeping total anneal time 10 min. from 10x10 um^2 area a) CT9-2-AN32 for 1 cycle, b) CT9-2-AN33 for 2 cycle and c) CT9-2-AN34 for 4 cycle. 60
Figure 81. Surface roughness of annealed samples at 420^oC as a function of annealing number of cycle from 10x10 um^2 area. 60
Figure 82. Etched by Everson method for cyclic annealed samples with keeping total time 10 min. a) CT9-2-AN32-E for cycle, b) CT9-2-AN33-E for 2 cycle, and d) CT9-2-AN34-E for 4 cycle. 61
Figure 83. Dislocation densities as a function of annealing time. Annealing was at 420^oC. 61
Figure 84. Raman shifts as a function of number of annealing cycle at 420^oC. Total annealing time was 10 min. Raman measurement were done at 80 K. 62
Figure 85. Raman shifts of Te A_1, 144 cm^{-1}, LO and 2LO phonon modes as a function of measurement temperature of cyclic annealed samples at 420 ^oC for 10 min total annealing time. 62

Figure 86. Variation of FWHM value of Te A_1, 144 cm^{-1}, LO and 2LO phonon modes of cyclic annealed samples for 10 min. at 420^oC. 63
Figure 87. Plot of optic phonon mode's $I_{Te\ A1}/I_{LO}$ ratios as a function of annealing cycle of annealed at 420^oC during 10 min. 63
Figure 88 . Graph of I_{144}/I_{LO} ratio as a function of annealing cycle. Raman measurement was done with cooling from 296 K to 80 K. 64
Figure 89. 3D graph of CdTe Raman spectroscopy result's 2LO/LO ratios changing with annealing cycle and Raman measurement temperature. 64
Figure 90. Photoluminescence spectra of cycle annealed samples at 80 K. Total annealing time was 10 min. Laser source was 488 nm. 65
Figure 91. SEM micrograph of annealed samples at 300^oC under 700 sccm H_2 atmosphere a) CT9-2-AN14 for 6 hours, b) CT9-2-AN13 for 12 hours and c) CT9-2-AN15 for 48 hours. 66
Figure 92. AFM 2D image of annealed samples at 300^oC under 700 sccm H_2 atmosphere from 10x10 um^2 area a) CT9-2-AN14 for 6 hours, b) CT9-2-AN13 for 12 hours and c) CT9-2-AN15 for 48 hours. 67
Figure 93. Surface roughness of annealed at 300 ^oC as a function of annealing temperature from 10x10 um^2 area. 67
Figure 94. SEM micrograph of Etched samples a) CT9-2-AN14-E, b) CT9-2-AN13-E and c) CT9-2-AN15-E. 68
Figure 95. Dislocation densities as a function of annealing time. Annealing was at 300^oC under 700 sccm H_2 atmosphere. 68
Figure 96. Raman shifts as a function of annealing time of annealed samples at 300^oC with 700 sccm H_2 gas. Raman measurements were done at 80 K. 69
Figure 97. Raman shifts of Te A_1, 144 cm^{-1}, LO and 2LO phonon modes as a function of measurement temperature of annealed samples at 300 ^oC under H_2 atmosphere. 70
Figure 98. Variation of FWHM value of Te A_1, 144 cm^{-1}, LO and 2LO phonon modes of annealed samples at 300^oC under H_2 atmosphere. 70
Figure 99. Plot of optic phonon mode's $I_{Te\ A1}/I_{LO}$ ratios as a function of annealing time of annealed at 300^oC under H_2 atmosphere. 71
Figure 100. Graph of I_{144}/I_{LO} ratio as a function of annealing time. Raman measurement was done with cooling from 296 K to 80 K. 71

Figure 101. 3D graph of CdTe Raman spectroscopy result's 2LO/LO ratios changing with annealing time and Raman measurement temperature. 72
Figure 102. Temperature dependent Raman spectra of CT9-2-AN20............................ 78
Figure 103. Raman spectrum ofCT9-2-AN21 at 296 K... 78
Figure 104. Raman spectrum ofCT9-2-AN21 at 250 K... 79
Figure 105. Raman spectrum ofCT9-2-AN21 at 200 K... 79
Figure 106. Raman spectrum ofCT9-2-AN21 at 150 K... 79
Figure 107. Raman spectrum ofCT9-2-AN21 at 120 K... 80
Figure 108. Raman spectrum ofCT9-2-AN21 at 100 K... 80
Figure 109. Raman spectrum ofCT9-2-AN21 at 80 K... 80
Figure 110. Raman spectrum ofCT9-2-AN30 at 296 K... 81
Figure 111. Raman spectrum ofCT9-2-AN30 at 250 K... 81
Figure 112. Raman spectrum ofCT9-2-AN30 at 200 K... 81
Figure 113. Raman spectrum ofCT9-2-AN30 at 150 K... 82
Figure 114. Raman spectrum ofCT9-2-AN30 at 120 K... 82
Figure 115. Raman spectrum ofCT9-2-AN30 at 100 K... 82
Figure 116. Raman spectrum ofCT9-2-AN30 at 80 K... 83
Figure 117. Raman Shift of 2LO mode of CT9-2-AN14. 83

CHAPTER 1

INTRODUCTION

CdTe is the most widely used buffer layer for HgCdTe growth by MBE on alternative substrates such as Si, Ge and GaAs. HgCdTe (MCT) is the most widely used infrared detector material[1]. Although CdZnTe has lower dislocation (10^4-10^5 cm^{-2}) densities compare to other alternative substrates for MCT, it has limitations in infrared Focal Plane Arrays (FPA). These are; high production costs, fragility, differences in coefficient of thermal expansion from the Si based materials used widely in technology and having smaller wafer areas then those of Si due to their inferior bulk growth processes compared to those of bulk Si [2]. Si has been used widely due to low cost and large area availability. However, there exist a large lattice mismatch between Si and MCT and buffer layer should be used between them. For that reason, CdTe is used generally as a buffer layer. As an indication of the quality, Etch Pith Density (EPD) is calculated to be as low as 10^6 cm^{-2} for CdTe (211)/Si(211) [3]. As an alternative substrate, GaAs has attracted a growing attention recently, its lattice mismatch with MCT is (14.6%) less than that of Si (19.3%). Additionally, polarity of the epilayer can be adjusted more easily when GaAs substrates are used during the growth. Crystal quality of GaAs substrate materials investigated with either EPD or DCRC FWHM [4] display as high quality as those of Si (Figure 1).

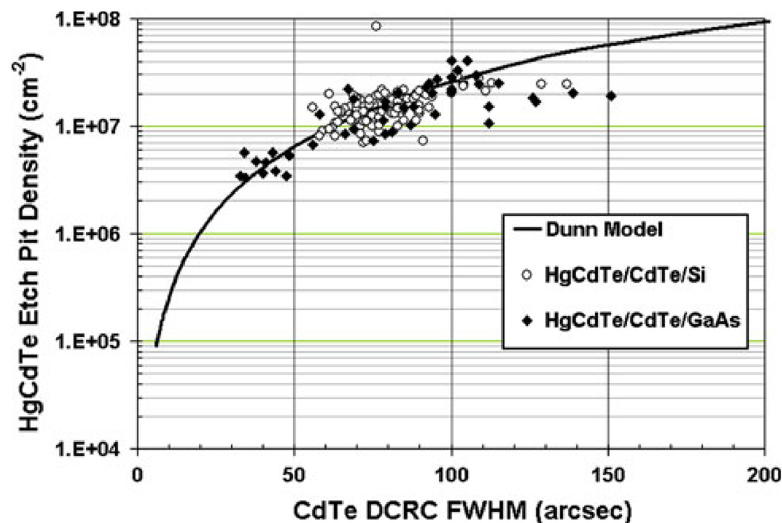

Figure 1. Dislocation density as a function of DCRC FWHM of HgCdTe/CdTe/GaAs [4].

Effects of dislocations on long wave infrared (LWIR) detector performance was investigated by Johnson et.al.[5]. They found that, dislocations significantly affect the detector performance. As an indicator of the quality of a detector, R_0A_j product is used widely, where R_0 is the zero voltage resistance and A_j is the effective junction area. R_0A_j decreases when EPD increases (Figure 2. a). Figure 2. b shows 1/f noise current increases linearly when dislocation density increases. Moreover quantum efficiency and short-circuit current density decreases with increasing dislocation density[5]. This study shows that dislocation density must be decreased below 10^5 cm^{-2} for LWIR FPA.

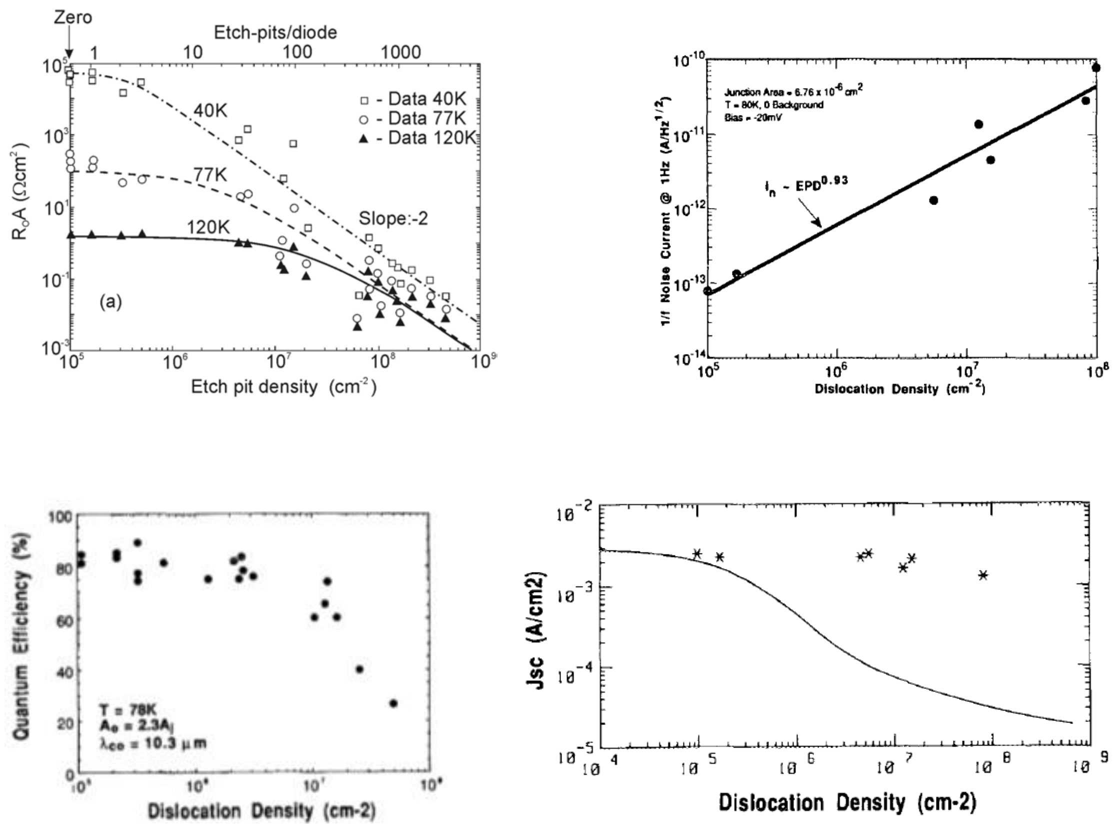

Figure 2. a) R_0A_j as a function of EPD, b) 1/f noise current at 1 Hz as a function of EPD at 78K, c) Quantum efficiency as a function of EPD at 78 K and d) Short circuit current density at 78 K as a function of EPD [5].

With the intension of improvement of detector performance, dislocation reduction has become very important all over the world. Annealing is the usual method of choice to reduce the density of dislocations. Dislocation reduction mechanism, during annealing, has not been understood yet clearly. It is known that, dislocation densities can be reduced with increasing annealing temperatures [6-9]. Besides dislocation density can decrease

when the number of annealing cycles increases. There are many studies about dislocation reduction with cyclic annealing in the literature [6, 7, 10, 11]. Recently a report has been published about annealing with 256 cycles with dislocation densities being reduced to about 10^6 cm^{-2} [8].

The dependence of dislocation density D on the number of cycles t and annealing temperature T is the given by the following equation:

$$D = D_0 e^{-\alpha T t} \quad (1.\ 1)$$

where D_0 is as-grown sample' dislocation density and α is a proportionality constant. This formulation was first used for GaAs/Si sample [9]. It is based on a model which assumes that only the annealing temperature and the annealing cycle will have an effect on the reduction of dislocations. This model lacks the annealing time and there is a confusing between annealing time and cycle number.

In addition to annealing, hydrogen treatment can also be used to improve the detector quality for MCT based materials. Hydrogen is an important element for improving electrical and optical properties of a semiconductor. It is a common impurity in a semiconductor included naturally in the starting materials or induced during the growth from the chemicals and the gases containing hydrogen. It has high diffusivity at room temperature and it can incorporate into materials easily. This makes the hydrogen both desirable and undesirable. Nevertheless, it passivates electrically active dangling bonds and reduces dislocations in amorphous and polycrystalline semiconductors. Additionally, hydrogen decreases the leakage currents in p-n junctions. It is also important for single-crystal semiconductors. Hydrogen incorporation can reduce surface dangling bonds, impurity states, and defects interfaces. It can also be used for surface deoxidation to get rid of native oxides [12-14]. In addition, it passivates point defects, extended defects, and shallow and deep levels[15]. It is an amphoteric material, thus, it can activate or deactivate both donors and acceptors dopants.

As a tool for optical characterization, Raman spectroscopy plays a major role for identification of chemical and crystal structure of materials via electronic, vibrational, and rotational excitations. It is a two step process in which a monochromatic light beam incident on a material medium, can excite the medium atoms via internal transitions. Excited entity may lose energy via an emission of a light photon. If incident and emitted photons have the same energy (same frequency), scattering is elastic, which is called Rayleigh scattering. If the scattered photon has less (more) energy than the incident, it is

called Stokes (anti-Stokes) scattered Raman light. In both Stokes and anti-Stokes scattered cases, the incident photon and the scattered photon energies will differ from each other by an amount equal to some internal energy difference. Thus by studying this difference, one can understand the possible energy level separation for the material medium. This provides valuable information about the structure of the medium. Thus, Raman spectroscopy is essential to study chemical and structural properties. In semiconductors, Raman spectroscopy is essential to study phonons, excitons, plasmons, polarons, and polaritons. Electronic transitions, such as deep or shallow impurity levels, as well as their vibrionic properties can also be studied with Raman spectroscopy. There exist many other cases where Raman scattering is useful. In elastic scattering of light was first predicted theoretically by Smecal [16] in 1923. Such a scattering was first observed by C.V. Raman [17] and also by Landsberg and Mandelstam in 1928 [18]. Abstreiter [19] in 1978 shows a range of capabilities of Raman spectroscopy. Various applications of Raman Spectroscopy such as crystal orientation, depth profile, carrier concentration, was displayed for GaAs and $Al_xGa_{1-x}As$ samples [20].

The earliest Raman analysis of CdTe was presented in 1968 by A. Mooradian and G.B. Wright, where plasmon-phonon interaction were observed. Characterization of Te precipitation in CdTe crystal by Raman Spectroscopy was studied first in 1983 [21]. In that study a CdTe crystal was grown by Bridgman method. The samples were analyzed at 300 K. Three peaks were observed at 90 cm^{-1}, 120 cm^{-1} and 139 cm^{-1}. The peaks were assigned as Te (E), Te (A_1) and Te (E) respectively based on two other studies [22, 23]. In 1984 P. M. Amirtharaj and Fred H. Pollak removed the Te excess on CdTe surface [24]. They used (100), (110) and (111) oriented CdTe films, etched by Br/ Methanol solutions and characterized the samples with Raman Spectroscopy. The study clarified that the peak at 141 cm^{-1} was the combination of Te (E) with CdTe (TO), except for the (100) oriented CdTe. In 1987, InSb-CdTe interface was examined by Raman Spectroscopy [25]. In^+ implanted CdTe was analyzed using resonant Raman Scattering in 1989 [26]. In^+ dose effects were analyzed by looking at Intensity (I) (2nd order LO)/ I (1st order LO) ratios of CdTe. It was observed that I (2nd order)/ I (1st order) ratios decreased as In^+ dose was increased. In 1989 multi-phonon Raman scattering was studied for (001) CdTe, overtones of LO phonon modes and CdTe 3LO, 4LO, 5LO, and 6LO overtones were observed for the first time [27]. In 1995 CdTe (111) sample were annealed for reduction of the Te precipitation, and analyzed with Raman Scattering[28]. Te related lines disappeared in the samples annealed for 22 hours at 500 ^{o}C. In 2014 thick CdTe

films were analyzed with Raman scattering [29] and a new peak at 271 cm^{-1} was observed. The peak was assigned as 2TO of CdTe phonon mode.

This thesis focuses on the defect reduction processes in MBE grown CdTe films on GaAs substrates via ex-situ annealing. The annealing time and number of cycles are the main investigation topics. Additionally, annealing temperature and annealing under hydrogen atmosphere are investigated. Raman spectroscopy is used to analyze strain originated from dislocations to compare with dislocation density by an etch decoration method. Temperature dependence of the relevant Raman peaks are also investigated. Surface morphologies are studied by SEM and AFM techniques.

CHAPTER 2

EXPERIMENTAL TECHNIQUES

Thin film of CdTe was grown on GaAs substrate by an MBE system. They were later annealed ex-situ by a homemade annealing setup. The samples were characterized with Raman spectroscopy, SEM, AFM and an etch decoration method. The details about these techniques will be given in the following sections.

2.1. CdTe Thin Films Growth by MBE

The MBE system was used GEN20 from VEECO in this study (Figure 3). This system consists of three main parts. These are the load lock, storage chamber and main chamber. Sample holder can be transferred with the help of 2 rods manually between the chambers. There is a manipulator in the main chamber, which rotates the sample in two direction. Sample can be heated with 2 heaters that are inner and outer heater. Thermocouples provide the control of the substrate temperature with feedback signal. Sample temperature can be read also by a kSA Bandit temperature monitor [30] and pyrometer. Pyrometer is an optical instrument which gives the substrate temperature from the measurement of a specific wavelength of infrared radiation. With these three components, the sample temperature can be monitored and controlled. The system has a Reflection High-Energy Electron Diffraction (RHEED) equipment which is used to understand the termination of deoxidation GaAs and also it gives an estimation for the sample crystal quality.

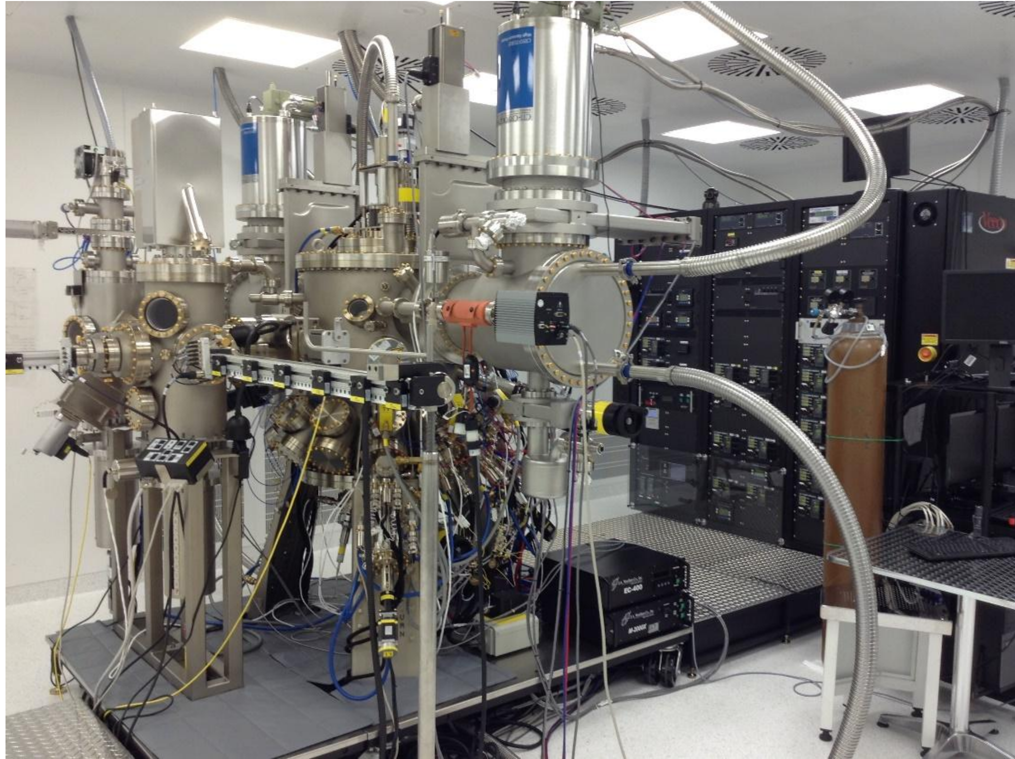

Figure 3. A schematic representation of MBE a) top view and b) side view.

CdTe films were grown on the (211) B GaAs wafers, were purchased from a commercial company, AXT [31]. GaAs is the preferred substrate due to its small lattice and thermal mismatch with CdTe, and the simplicity of the selection of polarity of CdTe film during their growth.

For the growth procedure GaAs wafers were cut in desired size and placed onto the substrate holder. Substrates were heated to 200°C for water desorption in the load lock chamber. Sample CT9 used for annealing studies, was grown on the 4'' GaAs wafer and chamber pressure was nearly 10^{-9} Torr. As, Te and CdTe sources calibrations were done and also for growth P, I and D values were taken as 135, 90 and 18 respectively. Figure 4 shows that the GaAs deoxidation temperature was at 620°C (according to pyrometer), nucleation layer temperature was at 364°C (according to pyrometer) and the growth temperature was 377°C (according to pyrometer). Deoxidation was done under As over pressure, beam equivalent pressure (BEP) was 5.16 x10^{-6} Torr. After the de oxidation all steps were carried out under Te over pressure with a BEP of 7.06 x 10^{-7} Torr. Nucleation layer took 30 seconds to growth under 6.7x10^{-7} Torr CdTe BEP. CdTe Growth took 2 hours under 6.7x10^{-7} Torr CdTe BEP. During the growth step, there was a decreasing trend in the substrate temperature decrease, so the growth temperature was kept at 364°C by slowly increasing the power.

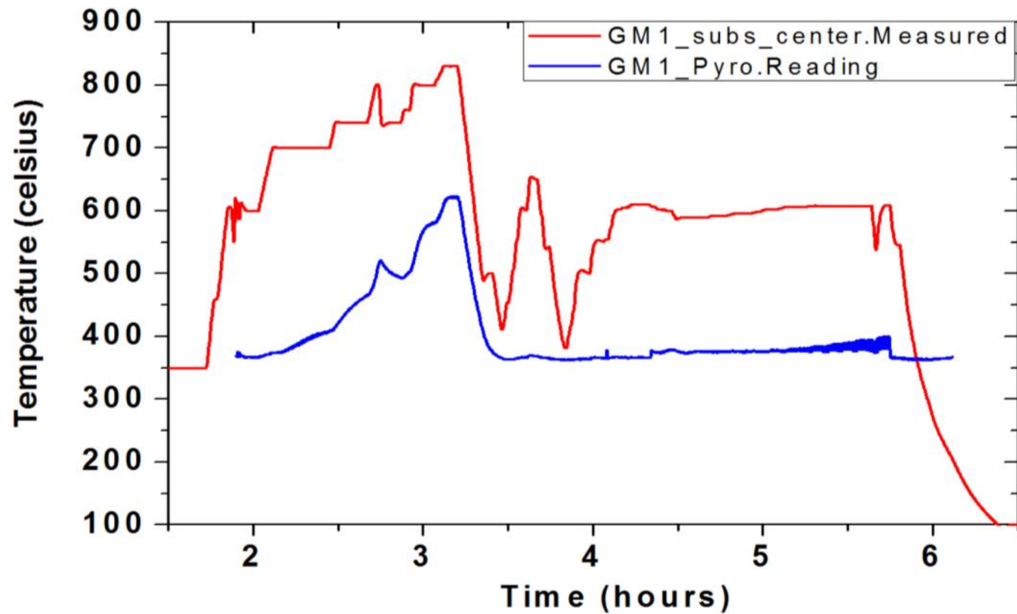

Figure 4. During the growth sample of G3AA-CT9 time versus temperature graph.

2.2. CdTe Thin Films Annealing by Home Made Quartz System

Annealing was done by a homemade quartz system. This section consists of designing and details of this system.

Figure 5 shows a picture of the experimental setup. The system consisted of a quartz tube, a sample heater apparatus, a DC power supply and gas sources. The quartz had a 60cm length and 2 in in diameter. The quartz tube was sealed by a leak proof seal which was with a quick flange kit. The flanges had two 0.6 cm diameter tubes for gas input and output. All of the gas lines were 316 ss tubes. The tubes were cut in required length, bent to required angles and were connected with Swagelok tube fittings.

In order to control gas flow, Omega FMA 1700/1800 series mass flowmeter was used. For passivation of high purity (99.98%) H_2 to was used as carrier gas with high pure Ar.

For evacuation the air from the system a roughing pump was combined with the system. A pressure gauge was used to monitor the pressure inside the annealing chamber.

Figure 5. A photograph of the designed annealing system.

Leak proof seal flanges were drilled 1 cm away from the middle. 0.15 cm in diameter cooper wires were isolated by ceramic beads and were pasted by epoxy adhesive to the flange's holes for the electrical contacts. Then the copper cables were connected with the sample heater and a power supply. The power supply was EMS 300V with 3.5A maximum current. The sample heater is shown in Figure 6. It consisted of a stainless steel blocs and a Si heater. The Si slab with a 3.5cm length and a 1cm width was cut from a (100) Si wafer (n-type doped 530 um thick). The part of Si wafer was connected with the stainless steel blocks by screws. After the system setup leak check was done using absolute methanol, the sample heater and the mass flow meters were calibrated.

Figure 6. The Si sample heater.

Calibration of the sample heater was done by melting the pure In, Se, Zn and an Al pellet. Melting points are 156.61°C, 217°C, 419.58°C, and 660.37°C for In, Se, Zn, and Al, respectively. Additionally they were melted on Si heater and their melting

currents were found. Temperature calibration graph is given in Figure 7. The values presented in this graph were used in further calculations in this thesis.

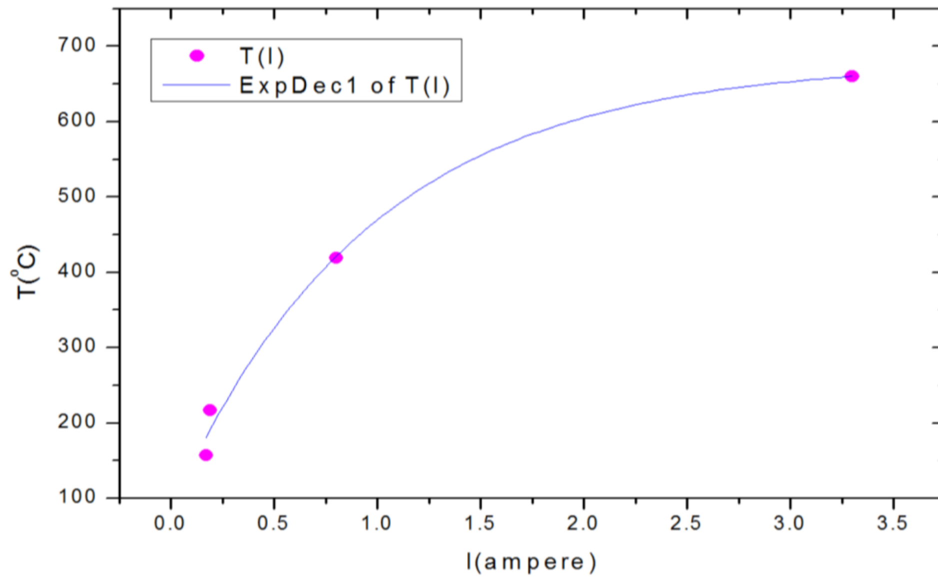

Figure 7. The temperature calibration graph. First point correspond In melting point, second point, third point, and fourth point corresponds melting points of Se, Zn, Al respectively.

H_2 gas calibration was done using a bubble meter. The bubbles were counted and time was measured with a chronometer. When bubbles takes the 100 ml lead, time was recorded. By using equation (2.1) output gas flow was calculated. Figure 8 shows the H_2 gas calibration values.

$$\text{output gas flow} = \frac{60 \times 100}{\text{elapsed time}} \tag{2.1}$$

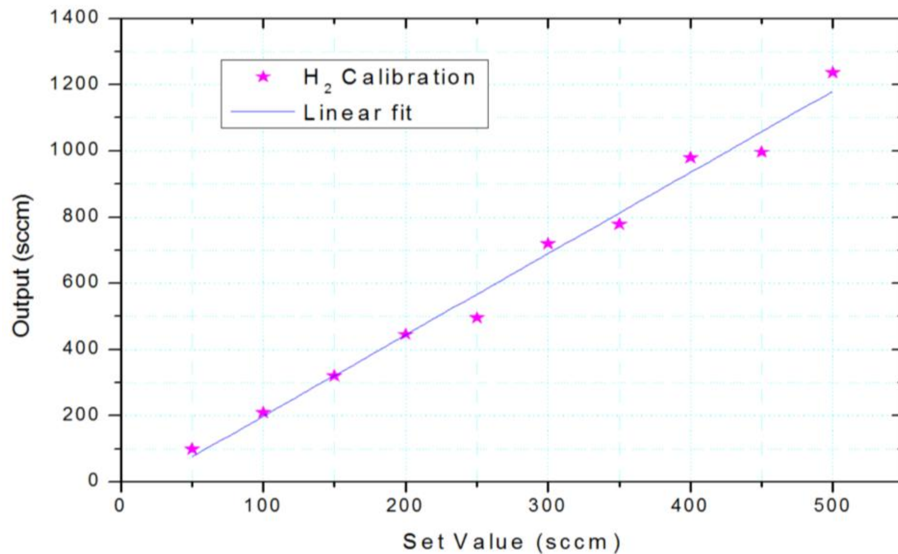

Figure 8. Mass flowmeter of H_2 gas calibration.

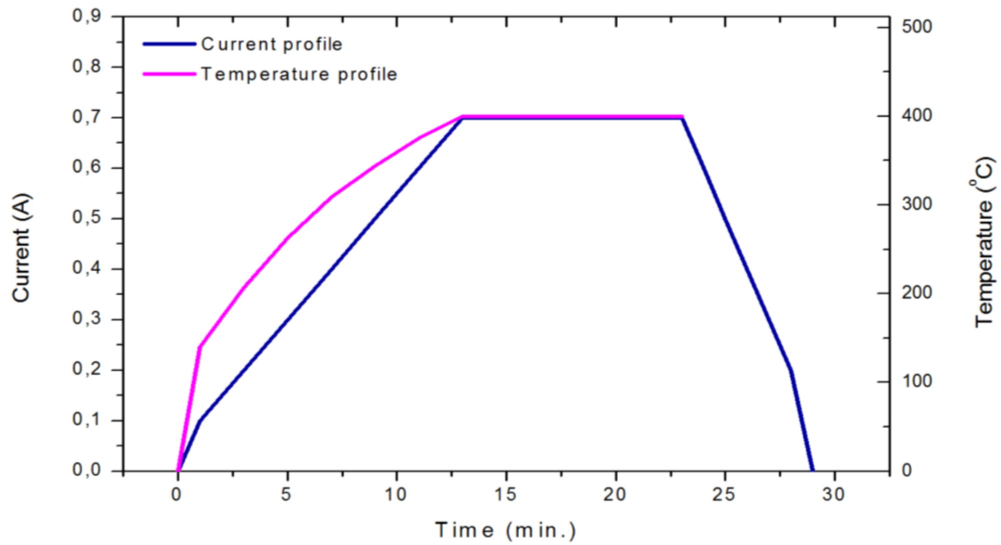

Figure 9.Temperature profile of CT9-2-AN10.

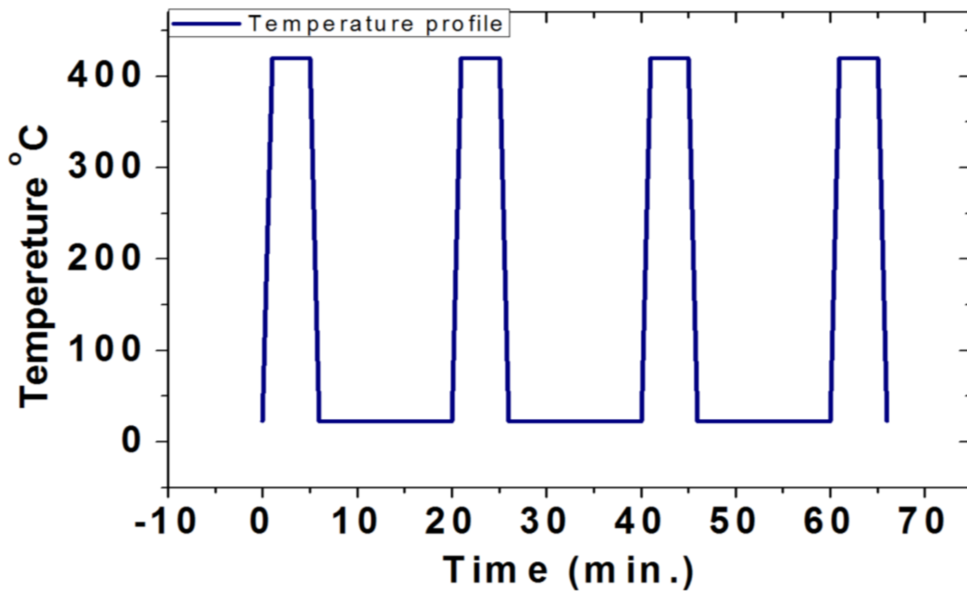

Figure 10. Temperature profile of CT9-2-AN30 sample.

Annealing was done by changing temperature while keeping the other parameters constant. Also anneal time was varied, while all parameters were fixed. Additionally cyclic anneals were done by keeping total time and temperature constant. Finally, anneal was also done by changing time under H_2 ambient. Annealing temperature was estimated by calibration results given in Figure 7. Some annealing was done by graph which is given in Figure 9 and some annealing was done by directly setting the temperature (current) as in Figure 10. Setting the current directly originated from a study [32] which has a system

for Carbon Nanotube (CNT) growth. That system has also silicon heater. Hydrogen flow was controlled with using calibration curve given in Figure 8. All anneal and etch conditions is presented in Table 1.

Table 1. Table of annealing and etch parameters.

SAMPLE NAME	I (A)	T(C)	CYCLIC/TIME	ANNEAL TIME	HIGH UP RAMP	COOL DOWN RAMP	H2 (sccm)	ETCH TIME (s)
ct9-2-an1	1,8	558		25 min.	0,1 A/1 min.	0,1A/min.	545	
ct9-2-an2	0,18	190		5 min.	0,1 A/2 min.	0,1A/min.		15
ct9-2-an3	1,16	485		5 min.	0,1 A/2 min.	0,1A/min.		25
ct9-2-an4	0,92	445		5 min.	0,1 A/2 min.	0,1A/min.		99
ct9-2-an5	0,7	400		5 min.	0,1 A/2 min.	0,1A/min.		50
ct9-2-an6	0,7	400		5 min.	0,1 A/2 min.	0,1A/min.		31
ct9-2-an7	0,75	410		5 min.	0,1 A/2 min.	0,1A/min.		30
ct9-2-an8	0,8	420		5 min.	0,1 A/2 min.	0,1A/min.		45
ct9-2-an9	0,66	390		5 min.	0,1 A/2 min.	0,1A/min.		50
ct9-2-an10	0,7	400		10 min.	0,1 A/2 min.	0,1A/min.		34
ct9-2-an11	0,7	400		20 min.	0,1 A/2 min.	0,1A/min.		33
ct9-2-an12	0,66	390		6 hours	0,1 A/2 min.	0,1A/min.	700 (300)	
ct9-2-an13	0,37	300		12 hours+15 min.	0,1 A/2 min.	0,1A/min.	700 (300)	12
ct9-2-an14	0,37	300		6 hours	0,1 A/2 min.	0,1A/min.	700 (300)	12
ct9-2-an15	0,37	300		48 hours	0,1 A/2 min.	0,1A/min.	700 (300)	12
ct10-an16	0,37	300		48 hours	0,1 A/2 min.	0,1A/min.		
ct9-2-an17	0,28	250		5 min.	0,1 A/2 min.	0,1A/min.		18
ct9-2-an18	0,37	300		5 min.	0,1 A/2 min.	0,1A/min.		15
ct9-2-an19	0,51	350		5 min.	direct	direct		27
ct9-2-an20	0,6	375		5 min.	direct	direct		15
ct9-2-an21	0,78	420		5 min.	direct	direct		49
ct9-2-an22	1,75	550		5 min.	direct	direct		15
ct9-2-an23	1,3	500		5 min.	direct	direct		15
ct9-2-an24	1,53	530		5 min.	direct	direct		15
ct9-2-an25	0,8	420		5 min.	direct	direct		18
ct9-2-an26	1	460		5 min.	direct	direct		26
ct9-2-an27	0,7	400		30 min.	direct	direct		18
ct9-2-an28	0,8	420	1X20	19 min.	direct	direct		15
ct9-2-an29	0,8	420	2X10	20 min.	direct	direct		15

(Cont. on next page)

Table1. (Cont.)

ct9-2-an30	0,8	420	4X5	20 min.	direct	direct		15
ct9-2-an31	0,8	420	8X2,5	20 min.	direct	direct		15
ct9-2-an32	0,8	420	1X10	10 min.	direct	direct		15
ct9-2-an33	0,8	420	2X5	10 min.	direct	direct		15
ct9-2-an34	0,8	420	4X2,5	10 min.	direct	direct		15
ct9-2-an35	0,18	190		20 min.	direct	direct		15
ct9-2-an36	0,37	300		20 min.	direct	direct		15
ct9-2-an37	0,51	350		20 min.	direct	direct		15

2.3. Raman Characterization

Raman spectroscopy was used to characterize samples. Optic phonons are investigated with Raman scattering to characterize the samples. Raman spectra of all samples before and after annealing are obtained and compared. Figure 11 displays the experimental setup of our Raman spectrometer, S&I Mono Vista, Germany, used in this study. This system was used for both Raman and Photoluminescence measurement. The system has two laser sources: an Argon ion gas laser for 514 nm and 488nm wavelengths and a Helium-Neon gas laser emitting light at a wavelength of 633 nm.

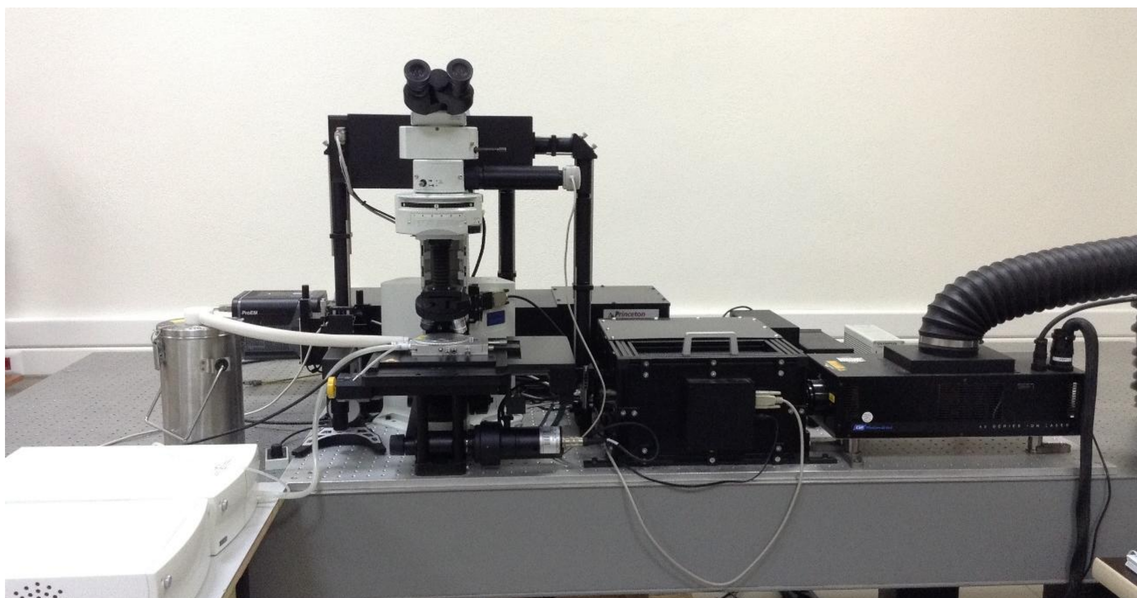

Figure 11. Schematic diagram of Raman Spectroscopy system.

Temperature dependent measurements were done by a Linkam vacuum chamber with an adjutable temperature range from 80 K to 300 K.

After a beam of monochromatic light is incident on a sample, back scattered light is collected via focusing objectives and sent to a monochrometer after filtering the Rayleigh component via a notch filter on the optical path before the monochrometer. The inelastically scattered light photon energy will be either less (Stokes) or more (anti-Stokes) by an amount equal to some internal energy difference inside the medium. Thus, Stokes scattering is more dominant at lower temperatures where most of the scatters are in their ground state. As the temperature increases, excited states will be populated more and more causing an increases in the Anti-stokes light due to transitions to ground state. Intensity ratios of Stokes-anti-Stokes lines is given as:

$$\frac{I_{anti-Stokes}}{I_{Stokes}} = \frac{I(w+\Omega)}{I(w-\Omega)} = \frac{n_K}{n_K+1} = e^{-\frac{\hbar\Omega}{k_B T}} \tag{2.2}$$

where, w is the excitation frequency, Ω is due to an internal transition, n_K is the Fermi distribution function, K is the wave vector, k_B is the Boltzmann constant and T is the temperature.

In this study, 488 nm line of the Ar-ion laser source was used. 488 nm match up better with $E_0+\Delta_0$ [27] which is Γ_6- Γ_7 CdTe spin-orbit split- off. This cause resonant scattering. In this case 2LO and LO phonon modes will have the same intensity at 80 K.

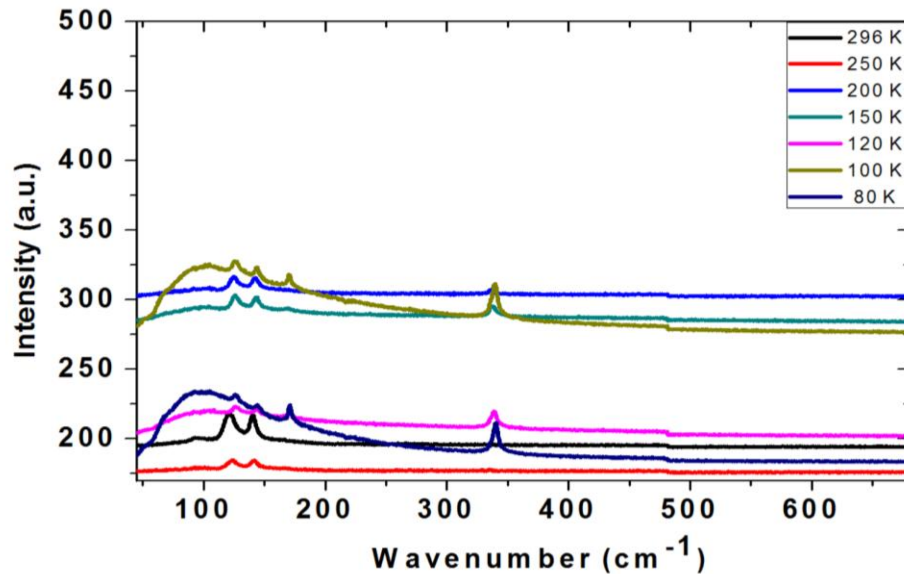

Figure 12. As grown CT9-2 sample’s Raman spectra at different temperature.

There were background radiation in spectra. As an example as-grown CT9-2 sample's Raman spectrum is given in Figure 12. Background was removed and baseline was formed in the same line (Figure 13). In order to be sure for the correct calculation of modes' height and center, peaks were fitted to some Lorentz functions. Figure 14 illustrates fitting of the CT9-2-an13 at 80 K. The green lines represent the individual modes and red lines represent overal fit. Two different samples were analyzed in the Appendix A for all measured temperatures.

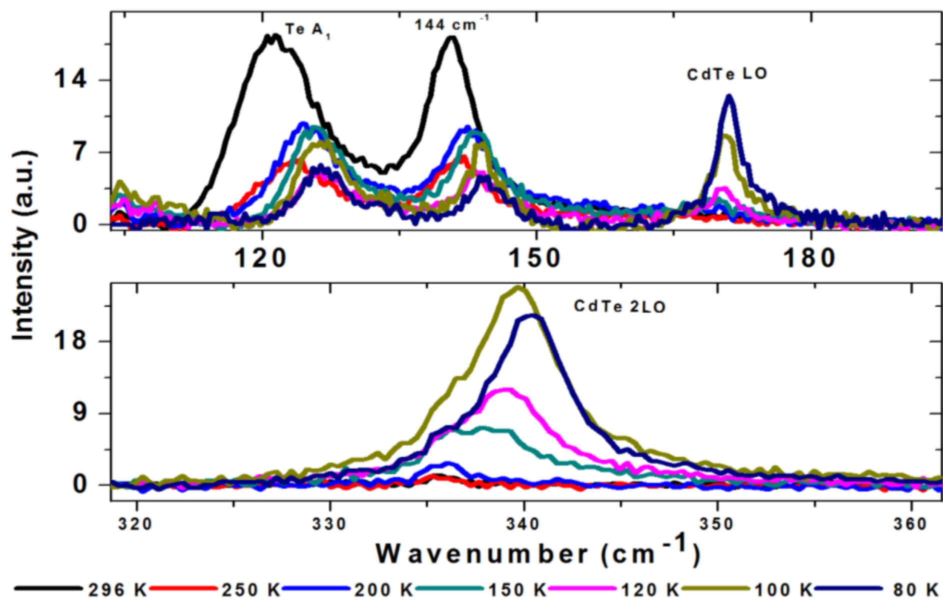

Figure 13. After the background correction as-grown CT9-2 sample's Raman spectra at different temperature.

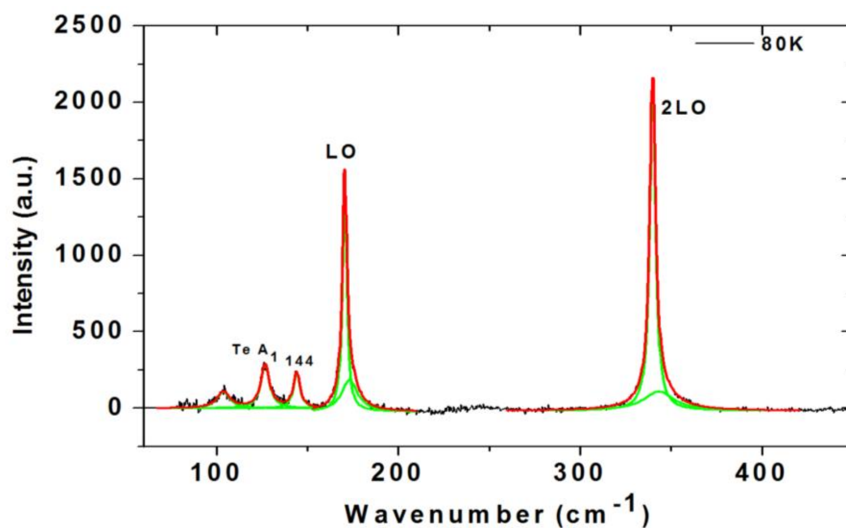

Figure 14. Fitted Raman spectra of CT9-2-an13 sample at 80 K.

In this thesis, peaks at 76, 84, 93, 99, 105, 125, 141, 166, 174, 334, 340, 506 and 660 wavenumbers (cm^{-1}) were observed. The assignments of these pics were carried out according to the literature: 125 cm^{-1} represents Te A_1 phonon mode, while, 166 cm^{-1} was due to CdTe LO, 334 cm^{-1} is labeled as CdTe 2LO modes and 506 is assigned to CdTe 3LO [20, 23-29, 33-35]. The 144 cm^{-1} peak was complex and it was hard to identify, since Te E phonon mode was expected in that wavenumber [23, 24, 34, 35] and also there is no report about CdTe (211) by Raman scattering, CdTe TO phonon modes were expected in that wavenumber also. CdTe TO/LO ratio is not known for (211) direction, it is going to be studied here.

2.4. SEM Characterization

SEM was carried out to compare sample surfaces before, after annealing as well as after EPD processes. The system is FEI QUANTA FEG 250 and it has Everhart-Thornley Detector (ETD) for high vacuum, Large Field Detector (LFD) for low vacuum, Backscattered Electron Detector (BSED), BSE for Energy-dispersive X-ray spectroscopy (EDX) analysis and Scanning Tunneling Electron Microscope (STEM) mode (Figure 15). For this study, ETD detector was used in high vacuum in different magnifications.

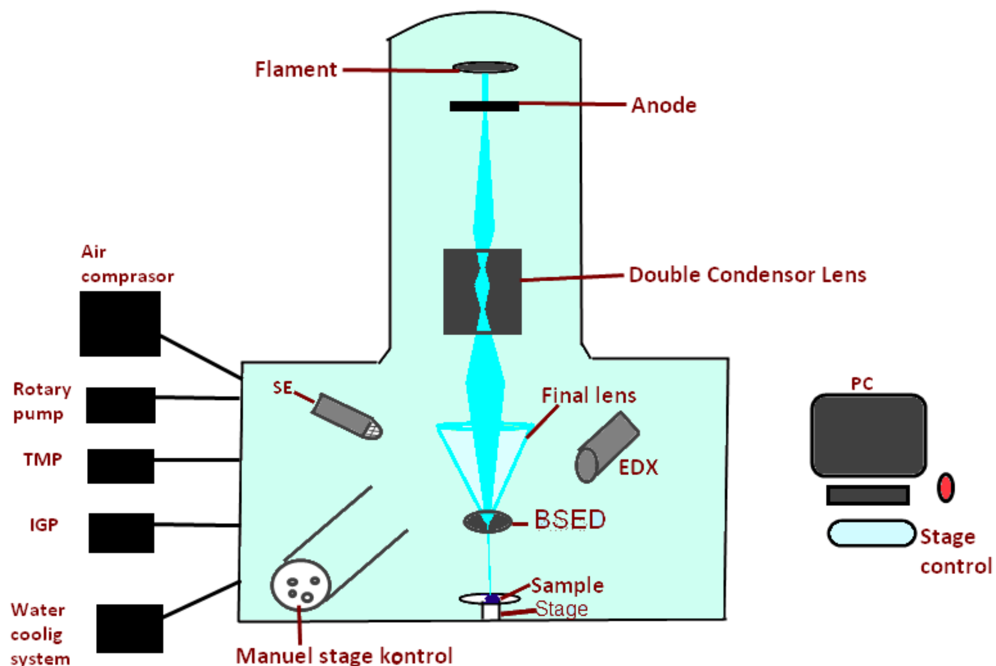

Figure 15. Schematic diagram of SEM system.

2.5. AFM Characterization

Surface morphology and surface roughness were studied by Atomic Force Microscopy (AFM) using a commercial NT-MDT system. Its schematic diagram is illustrated in Figure 16. For measurements golden silicon probes were used (NT-MDT). Cantilever is 135 um in length, 30 micron in width with a thickness of 1.5 micron. Resonant frequency range of a Cantilever is 47-150 kHz and force constant range of cantilever 0.35-6.1 N/m. All samples were analyzed over a 10x10 um^2 area and a 1x1 um^2 area by the semi contact mode.

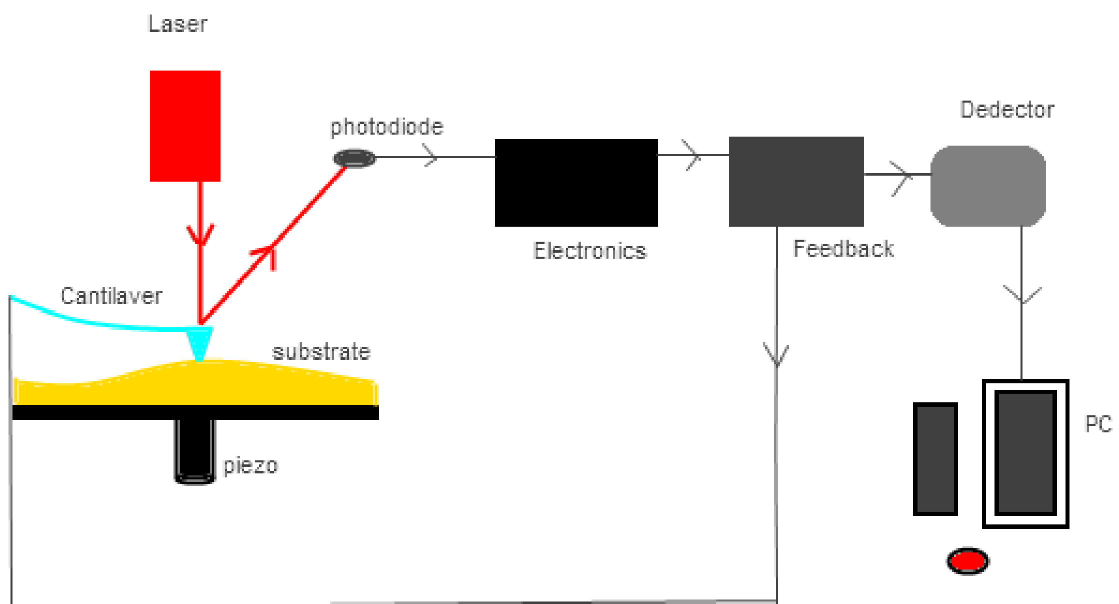

Figure 16. Schematic diagram of AFM system.

2.6. Defect Decoration Method

Dislocations were analyzed by a wet chemical etching method. The etch method was Everson, which is the most widely used method for CdTe (211) B face. The etch details of parameters was given in another study [36].

The used chemicals and volumes are presented in Figure 17. Firstly Lactic acid ($C_2H_4OHCOOH$) was placed in a solution beaker (polypropylene beaker). Next, nitric acid (HNO_3) was dropped into the solution beaker by a pipet. Then hydrofluoric acid (HF) was added. Samples were, then, placed in this Everson solution. All samples were etched in different times. The etch times are given in Table 1. The samples were rinsed in deionized water after each etch. Lastly, the samples were dried by high purity N_2 gas.

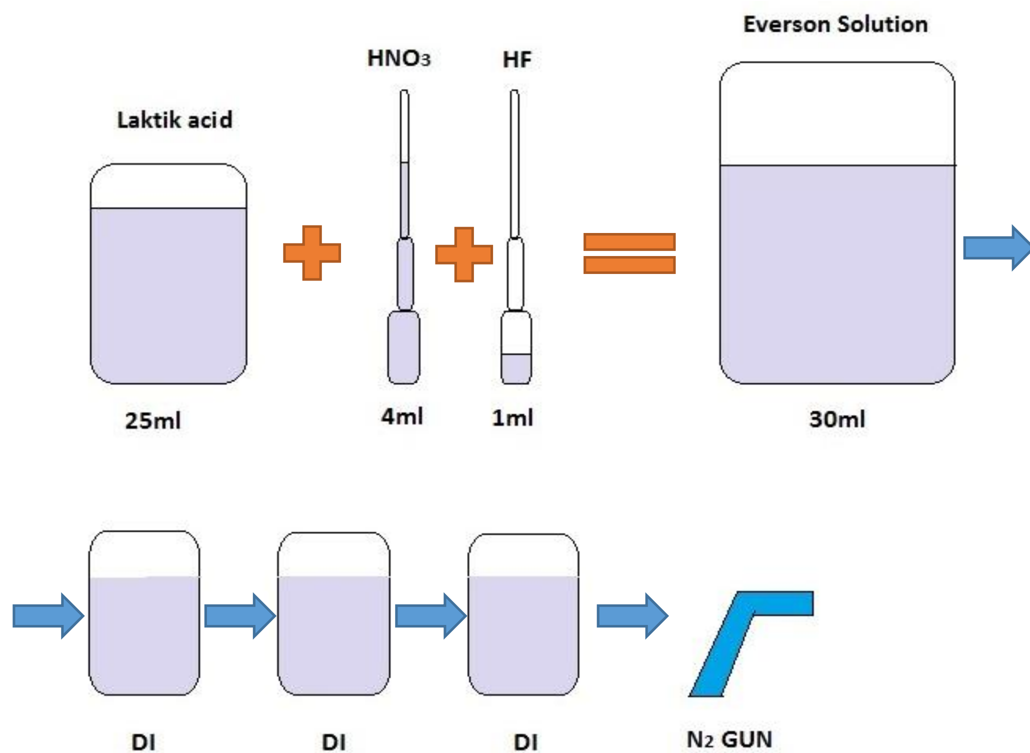

Figure 17. Everson etch steps.

CHAPTER 3

RESULTS AND DISCUSSION

This chapter has two main parts which are about annealing in vacuum and annealing with hydrogen gas.

3.1. Annealing Under Vacuum

Annealing was done under vacuum with a pressure of nearly 20-10 mTorr (medium vacuum) in the vacuum tube. Temperature, time and number of cycles were experimental parameters. Results obtained with these parameters are given in the following sections.

3.1.1. Effects of Annealing Temperature

In this part, time was fixed and temperature was varied. Temperature affects were investigated. Some annealings were done by increasing temperature at a fixed rate (Figure 18), some annealings were done by setting a desired temperature. There was just two different times for temperature studies; they were 5min. and 20min.

In the beginning, time was fixed at 5 min. and temperature was changed from 190°C to 485°C by varying the sample heater current by ramping. After the annealing surface morphology was analyzed by SEM. Figure 18 displays the SEM pictures for CT9-2 sample. When annealing temperature reach to 400°C, small holes appeared on the surface. Size of the holes grew up with increasing temperature. Next, annealed samples were etched by Everson method. After the etch surface morphology was again analyzed by SEM, typical SEM pictures are illustrated in Figure 19. Dislocation densities were calculated using SEM pictures and they are displayed a function of annealing temperature in Figure 20. Dislocation density first increased then decreased with increasing the annealing temperature.

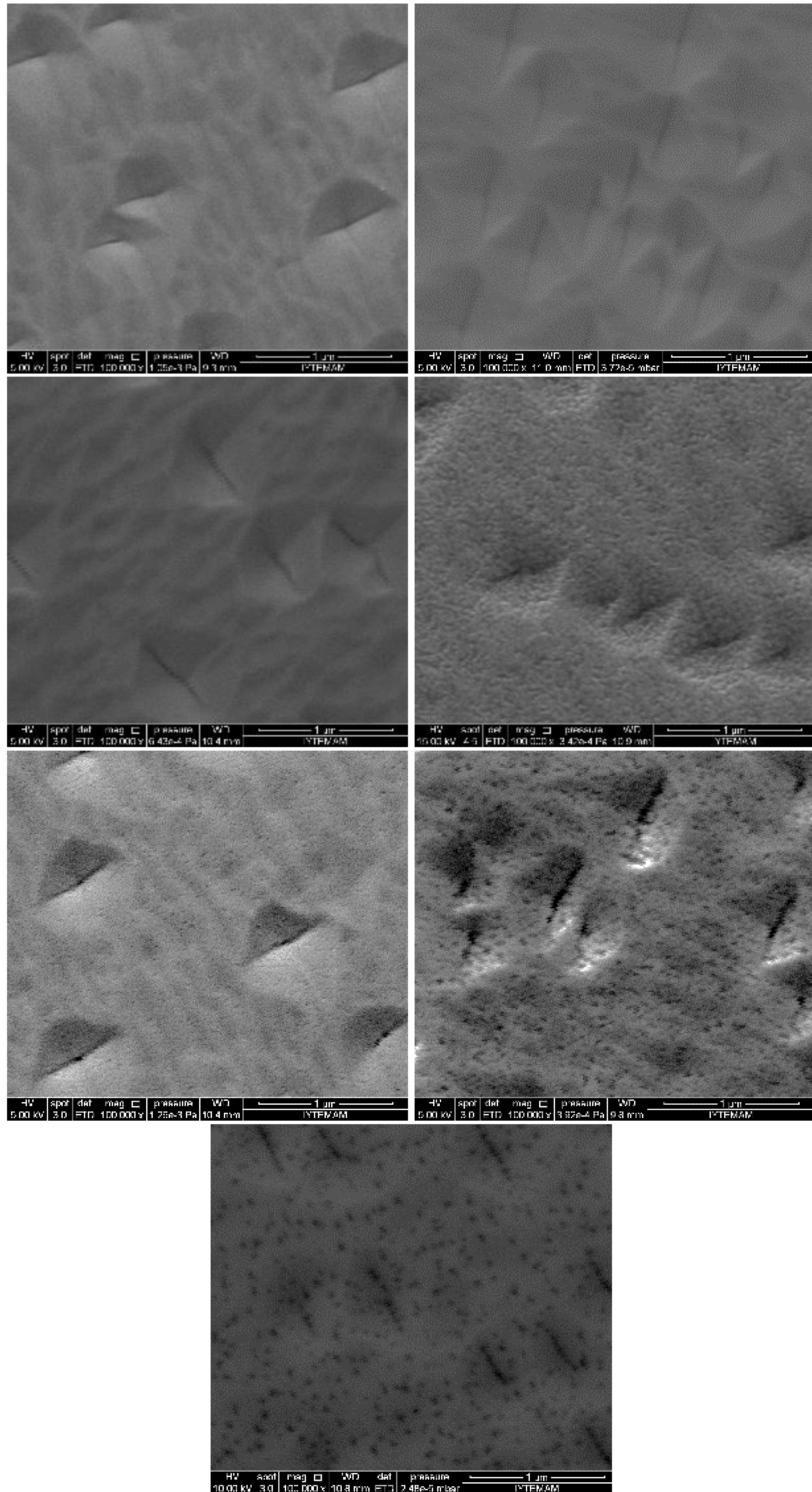

Figure 18. SEM micrograph of annealed for 5 min. a) as-grown CT9-2, b) CT9-2-AN2 annealed at 190ºC c) CT9-2-AN9 annealed at 390ºC, d) CT9-2-AN6 annealed at 400ºC, e) CT9-2-an7 annealed at 410ºC, f) CT9-2-AN8 annealed at 420ºC, and g) CT9-2-AN3 annealed at 485ºC samples.

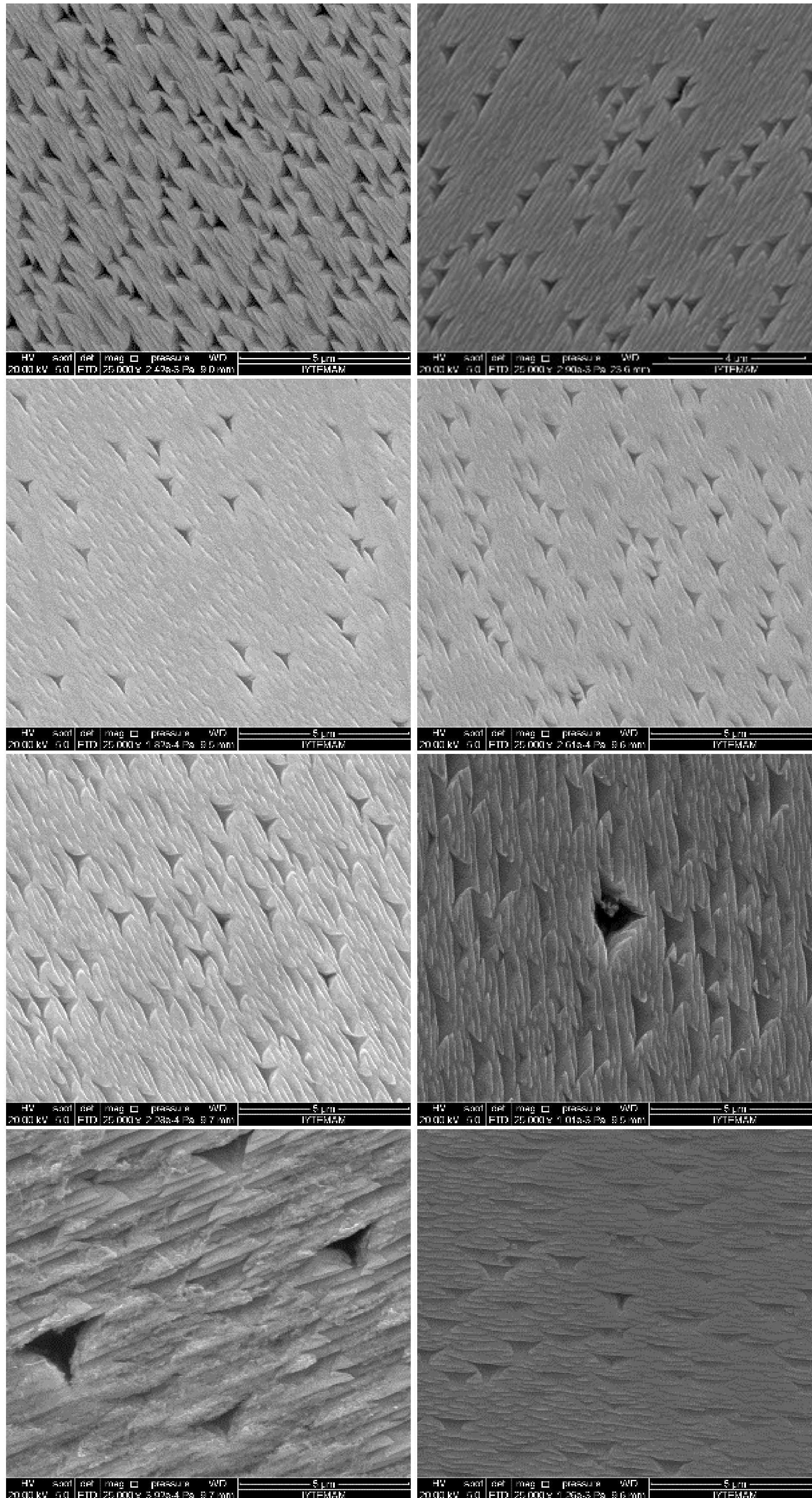

Figure 19. Etched by Everson method a) CT9-2-AN2-E, b) CT9-2-AN17-E, c) CT9-2-AN9-E, d) CT9-2-AN6-E, e) CT9-2-AN7-E, f) CT9-2-AN8-E, g) CT9-2-AN4-E and h) CT9-2-AN3-E samples.

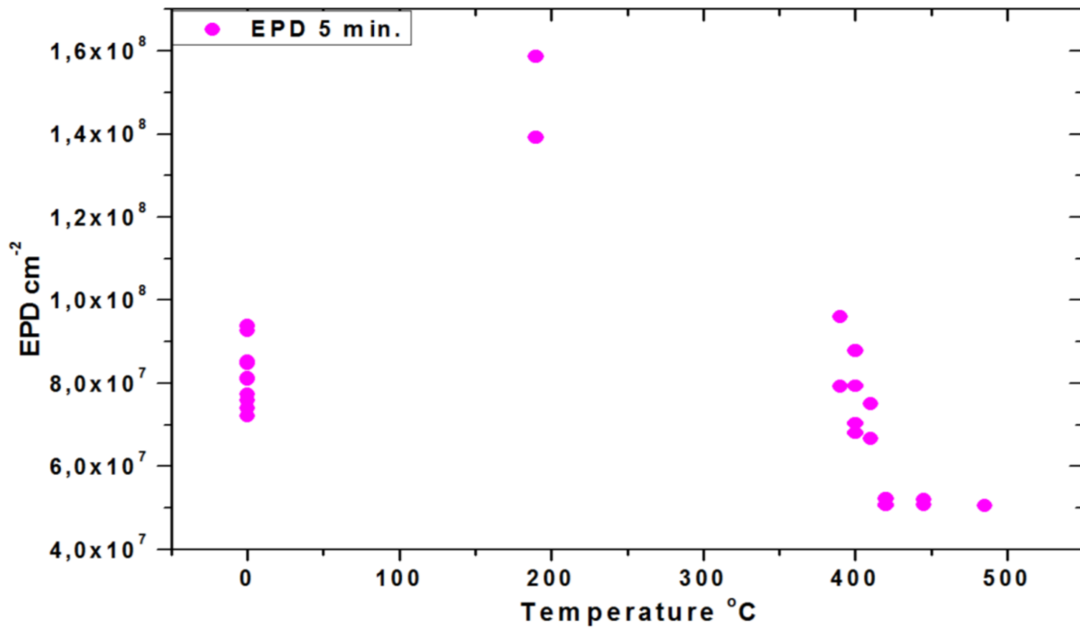

Figure 20. Dislocation densities as a function of annealing temperature. Annealing was for 5 min.

Raman shifts at 80 K is represented in Figure 21 for 5 min. anneals at different annealing temperatures. LO peak positions shifted from about 163 cm^{-1} to 171 cm^{-1}. Peak positions are displayed in Figure 22. Annealing temperatures did not affect 5 min. annealed samples. Measurement at higher temperatures display wider scattering. Lover measurement temperatures showed narrower dispersion.

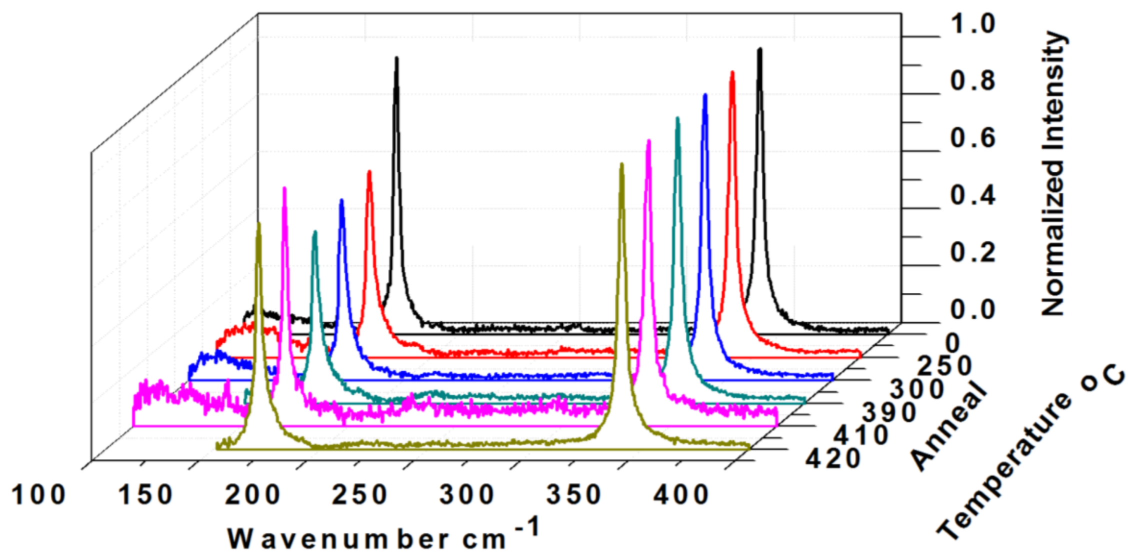

Figure 21. Raman shifts as a function of annealing temperature. Raman measurement were done at 80 K.

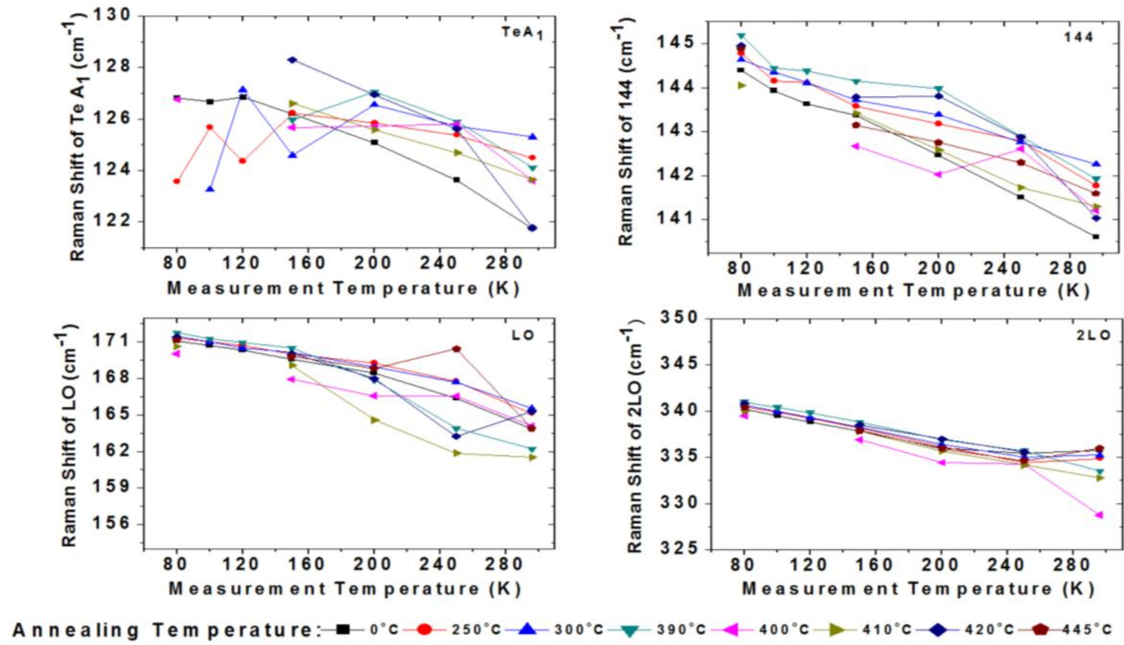

Figure 22. Raman shifts of phonon modes as a function of measurement temperature for 5 min annealed samples at 7 different temperature.

Full with at half maximum (FWHM) values of Raman modes are displayed in Figure 23 for 5 min. annealed samples. FWHM values decreased with decreasing sample temperature during Raman measurements for LO and 2LO modes. This decrease was not the same for Te A_1 and 144 modes. FWHM of LO value showed an increase for the 300°C annealing temperature while a decrease for 400 °C for annealed samples for higher measurement temperature (296 K, 250 K, and 200 K). However, FWHM of LO value was constant at different annealing temperatures for lower measurement temperature (150 K, 120 K, 100 K and 80 K). FWHM of 2LO mode increases for 415 °C annealing temperature. FWHM of 2LO peak is constant as a function of annealing temperature if temperature of Raman measurement is 296 K, 250 K. FWHM of 144 cm^{-1} mode had scattered. FWHM of Te A_1 mode did not change depending on annealing temperature. At colder measurement temperatures Te A_1 mode was not observable (see Figure 102 in appendix a), for this reason some points did not exist in the graph in Figure 23.

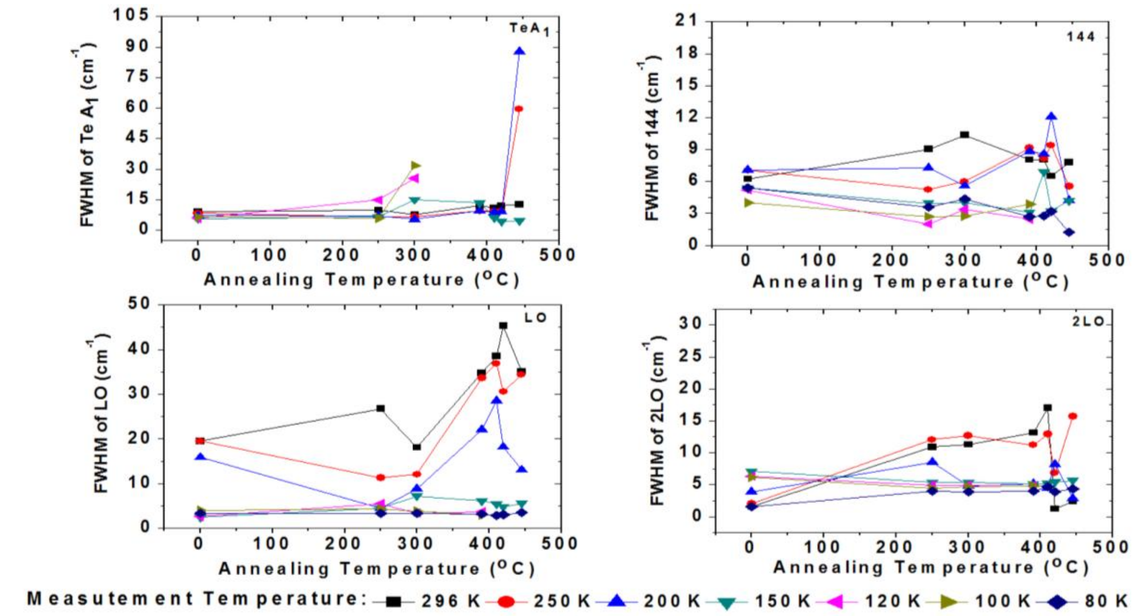

Figure 23. Variation of FWHM value of Te A_1, 144, LO and 2LO phonon modes of for 5 min. annealed samples.

$I_{Te\ A1}/I_{LO}$ ratios are presented in Figure 24. TeA$_1$/CdTe LO changed from about 23.5 to 0.4 .For as-grown sample and after annealing TeA$_1$/CdTe LO changed nearly from 3 to zero for annealed samples during 5 min. at seven different annealing temperature. Additionally, TeA$_1$/CdTe LO ratios decreased with decreasing measurement temperature.

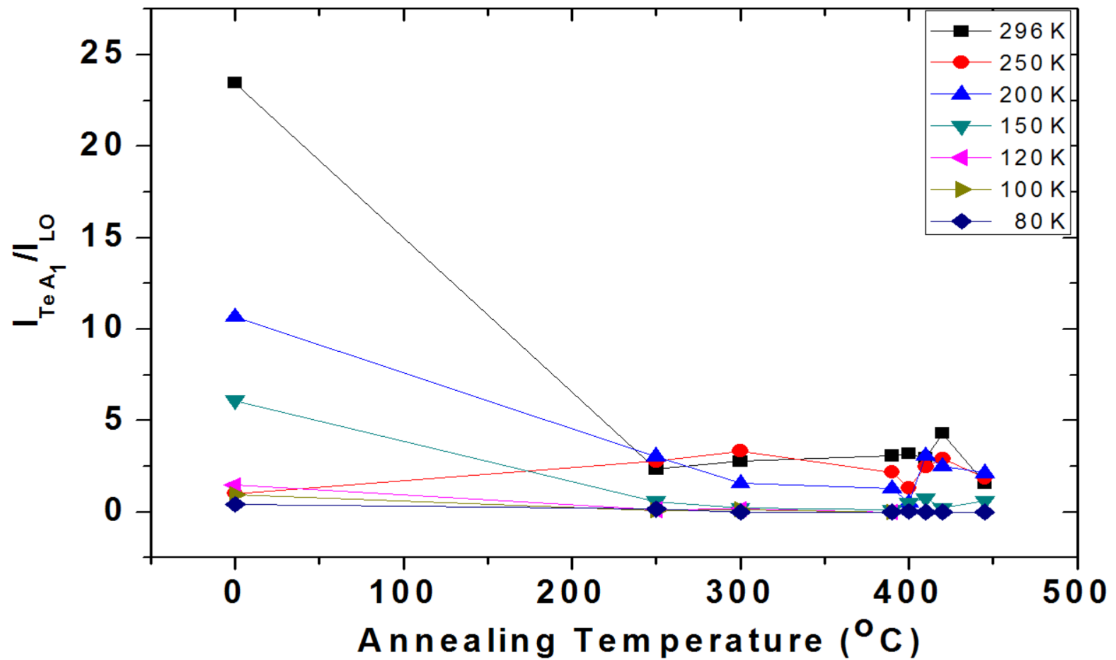

Figure 24. Plot of CdTe phonon modes $I_{Te\ A1}/I_{LO}$ ratios as a function of annealing temperature of annealed for 5min.

I_{144}/I_{LO} ratios are given in Figure 25. As-grown sample showed broad distribution (21.4 to 0.38) for different measurement temperatures. I_{144}/I_{LO} ratios distributed from 3 to 0.1 for 5 min. annealed samples and annealing temperatures were varied from 250°C to 445°C.

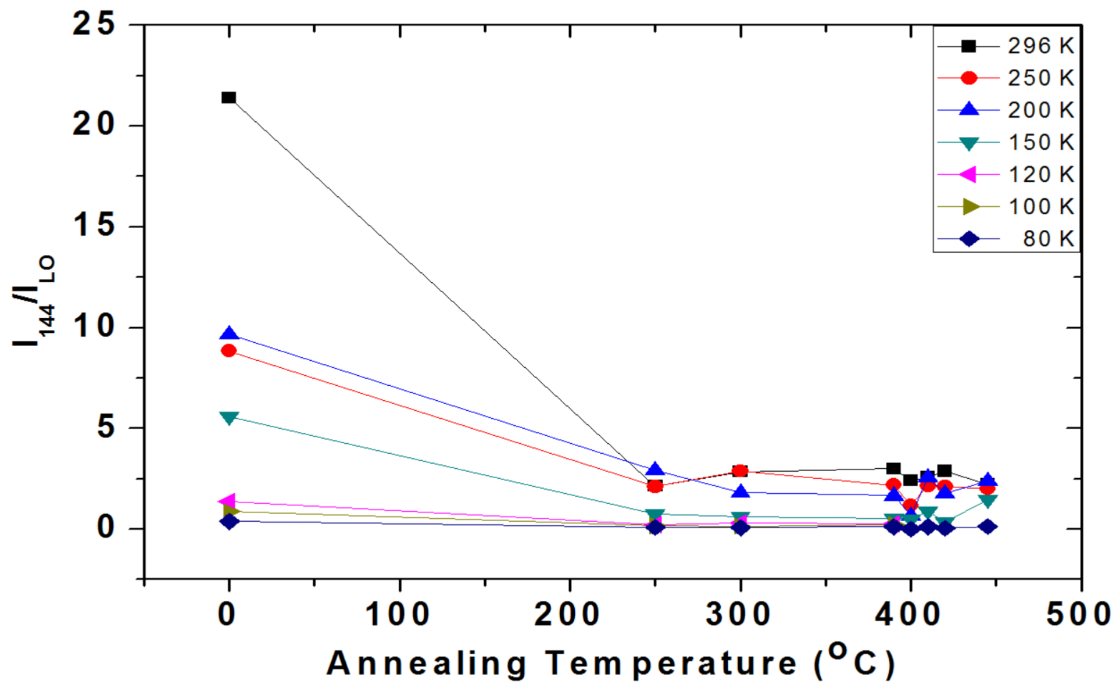

Figure 25. Graph of I_{144}/I_{LO} ratio as a function of annealing temperature. Raman measurement was done with cooling from 296 K to 80 K.

Figure 26 illustrates 2LO/LO ratios at seven different Raman measurement temperature for different annealing temperatures. 2LO/LO ratios decreased from 1.95 (as-grown sample) to 1.02 (at 445°C annealed sample) at 80 K measurement temperature. For 100 K Raman measurement temperature, 2LO/LO ratios decreased from 2.78 to 1.62. When Raman measurement temperature was 120 K, 2LO/LO ratios decreased 4.57 to 2.85. For higher measurement temperature, there was no correlation between 2LO/LO ratio and annealing temperature.

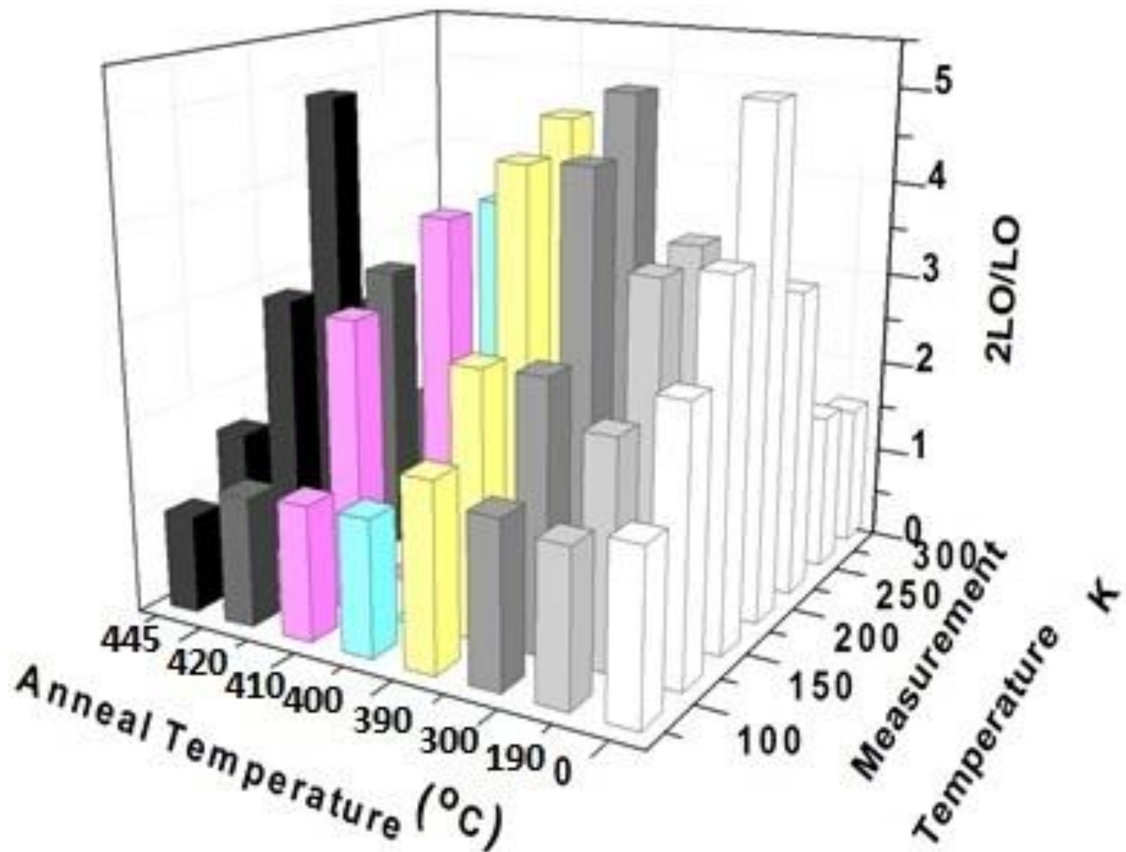

Figure 26. 3D graph of CdTe Raman spectroscopy result's 2LO/LO ratios changing with annealing temperature and Raman measurement temperature.

After that, annealing was done by setting the annealing current directly. These samples' surface were analyzed by AFM.

Figure 27 displays such AFM pictures. AFM roughness was calculated for 10x10 um^2 and 1x1um^2 area (Figure 28). Up to 0.8A, there was no identifiable change for surface roughness when temperature was increased. After 0.8A there was a rise with the increasing temperature. The annealed samples were etched by Everson method to compare dislocation density variation with sample heating type. The etched samples surface morphologies are displayed in Figure 29 and calculated EPD values are illustrated in Figure 30. Dislocation density decreased with temperature increasing and 0.8A was threshold current for dislocation decline.

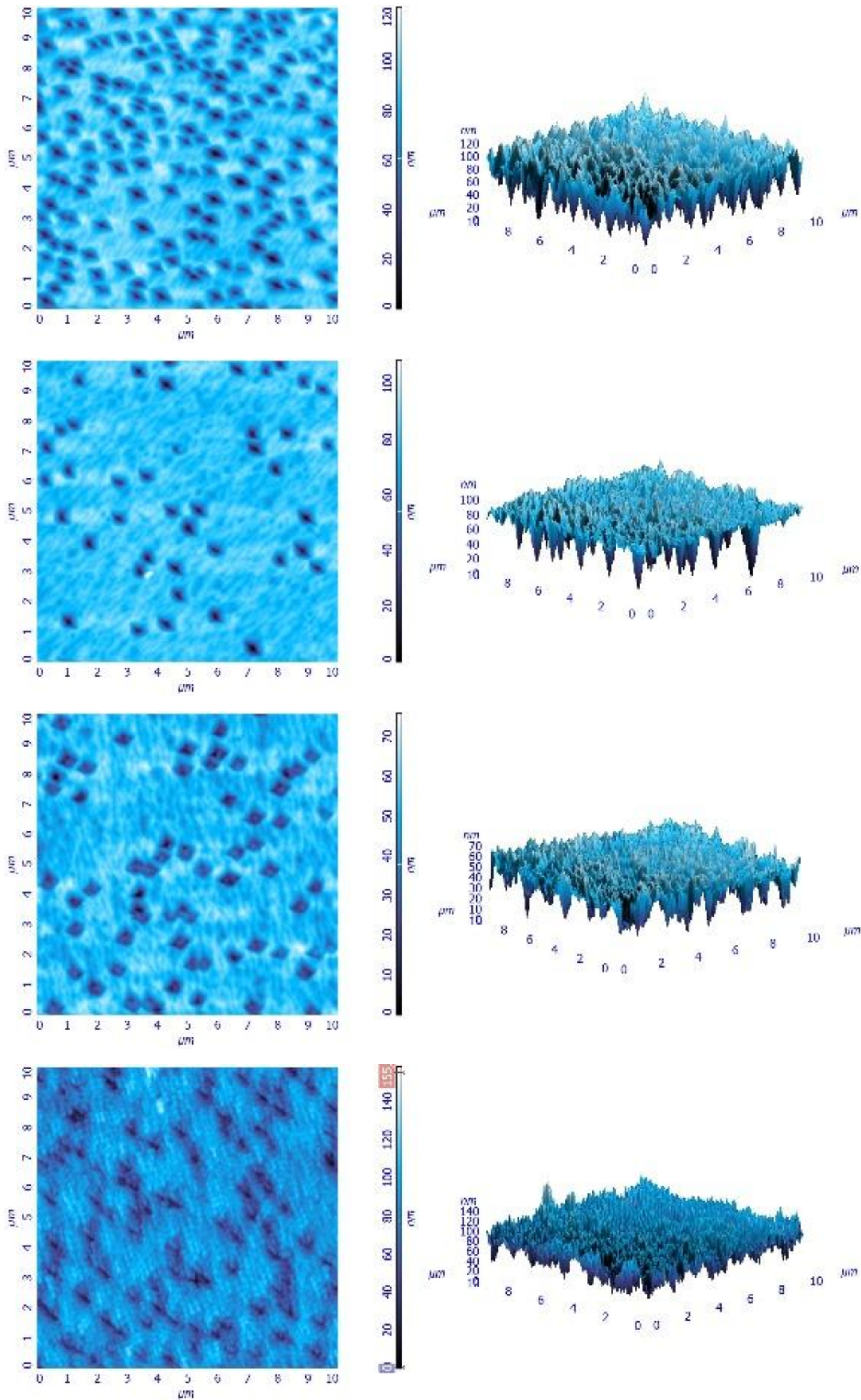

Figure 27. CT9-2-AN19 annealed at 350°C; a) 2D AFM image, b) 3D AFM image. CT9-2-AN21 annealed at 415°C c) 2D AFM image, d) 3D AFM image. CT9-2-AN23 annealed at 500°C e) 2D AFM image, f) 3D AFM image. CT9-2-AN22 annealed at 550°C g) 2D AFM image, h) AFM 3D image.

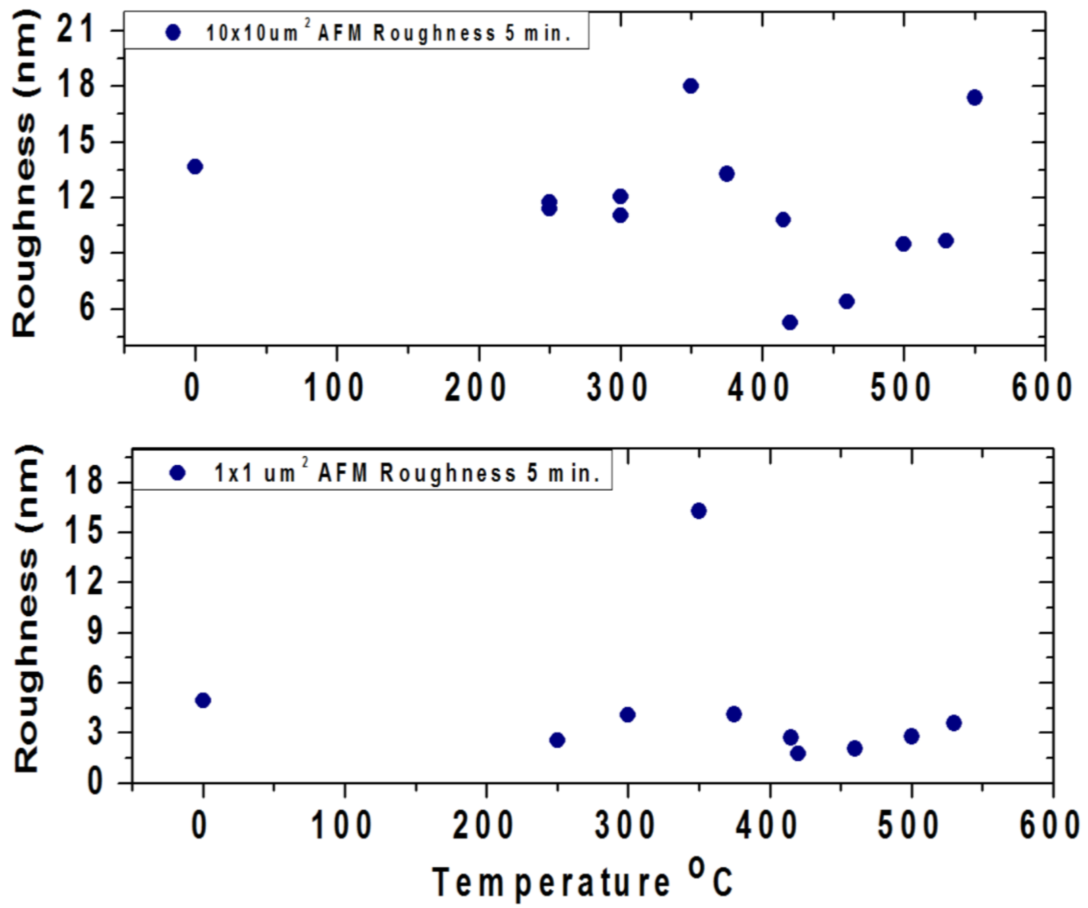

Figure 28. Surface roughness for 5 min. annealed samples as a function of annealing temperature obtained from 10x10 um^2 and 1x1 um^2 area.

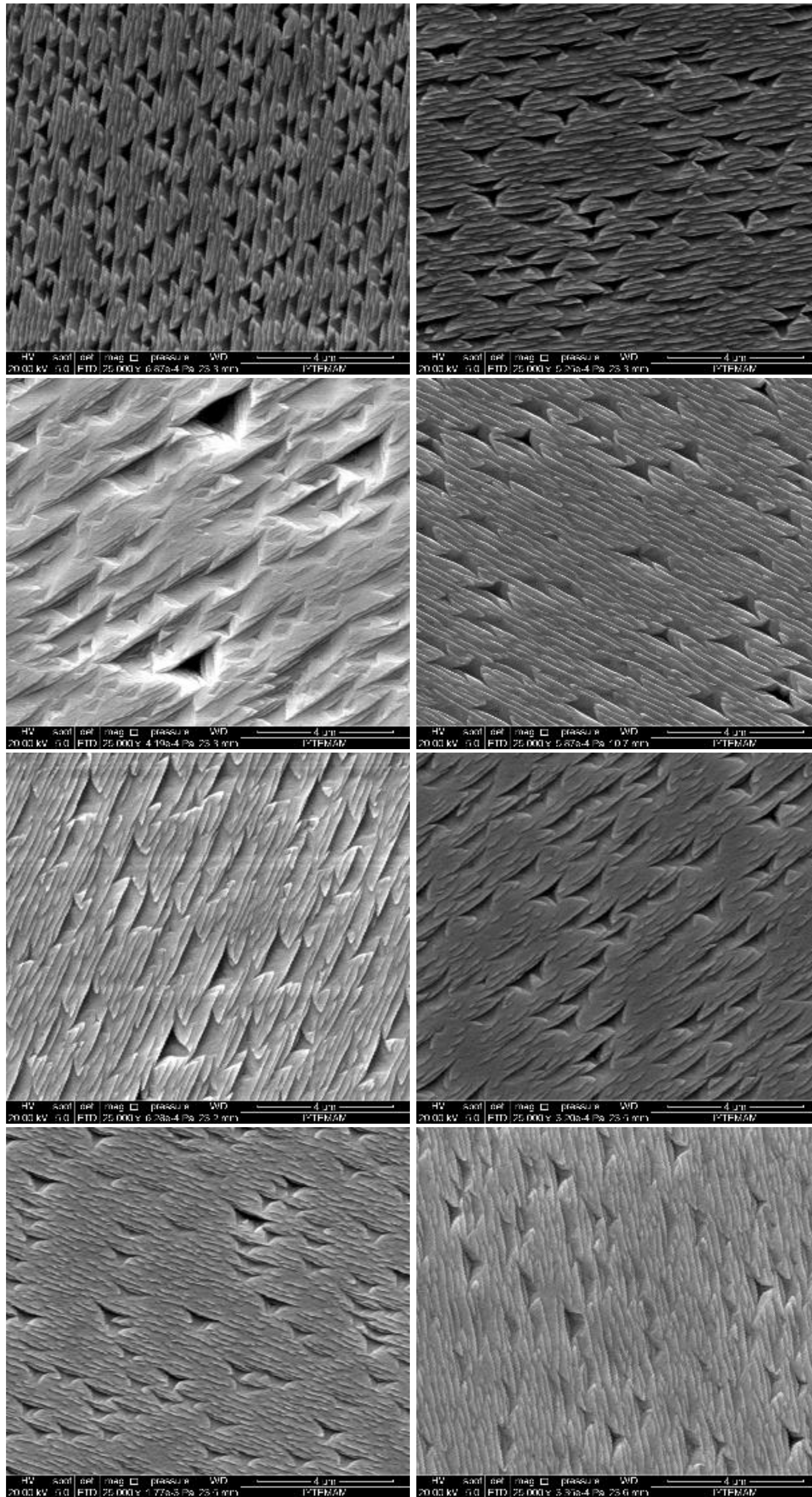

Figure 29. Etched by Everson method a) CT9-2-AN19-E, b) CT9-2-AN20-E, c) CT9-2-AN21-E, d) CT9-2-AN25-E, e) CT9-2-AN26-E, f) CT9-2-AN23-E, g) CT9-2-AN24-E and h) CT9-2-AN22-E.

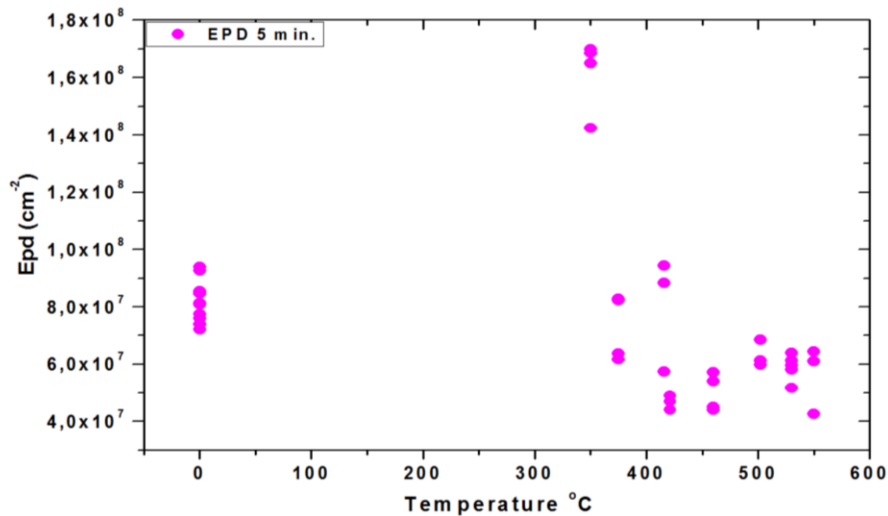

Figure 30. Dislocation densities as a function of annealing temperature. Annealing was for 5 min.

Raman spectra of rapidly heated samples are displayed in Figure 31. The four main modes of CdTe Raman peak positions are illustrated in Figure 32. Te A_1 modes shifted from nearly 124 cm^{-1} to 128 cm^{-1}, with decreasing of measurement temperature. 144 cm^{-1} phonon mode shifted from nearly 142 cm^{-1} to 144 cm^{-1}, when Raman measurement temperature changed from room temperature to 80 K. LO phonon modes shifted about from 165 cm^{-1} to 170 cm^{-1}, as decreasing of measurement temperature. Additionally 2LO phonon modes shifted linearly from nearly 333 cm^{-1} to 341 cm^{-1}, with a decrease of measurement temperature. There was not any change for phonon modes with the annealing temperature annealed for 5 min.

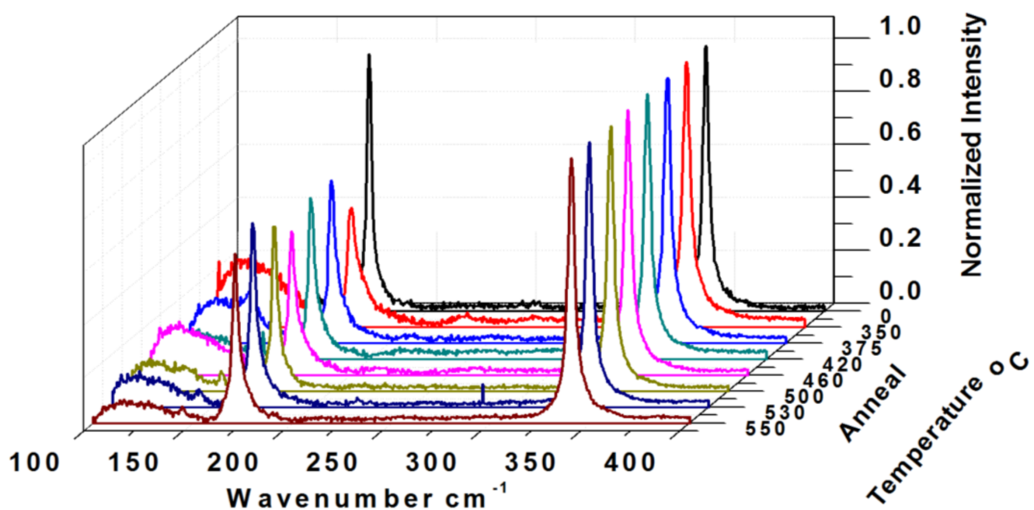

Figure 31. Raman shifts as a function of annealing temperatures. Raman measurement were done at 80 K and annealing time was 5 min.

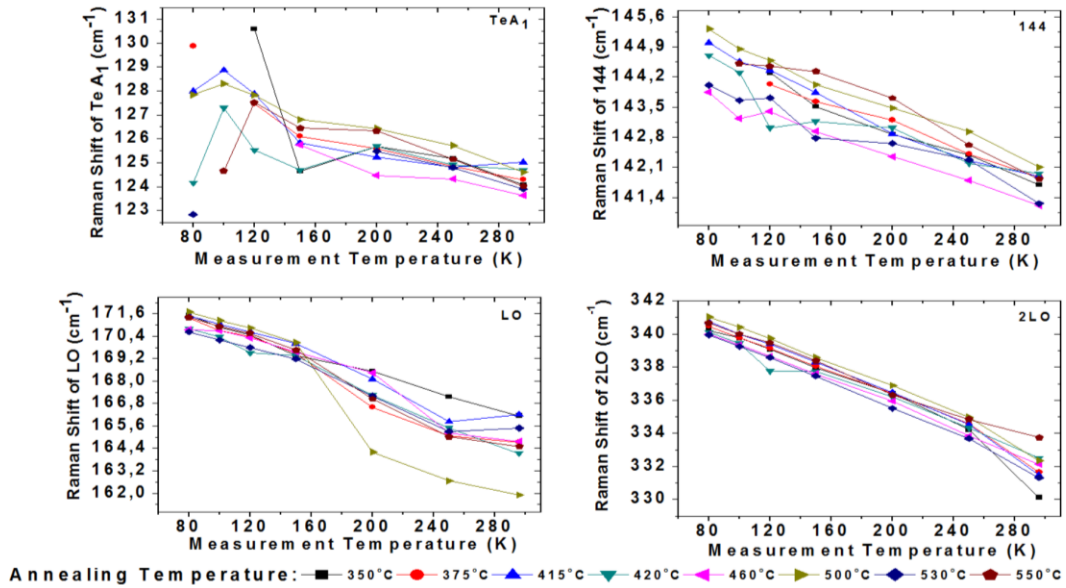

Figure 32. Raman shifts of Te A_1, 144 cm^{-1}, LO and 2LO phonon modes as a function of measurement temperature for 5 min. annealed samples at 7 different temperature.

FWHM values of Te A_1 modes of 5 min. annealed samples did not have a significant change, and 144 cm^{-1} phonon mode was the same as Te A_1 modes. The changing 144 cm^{-1} and Te A_1 modes were between 1 and 8 cm^{-1}. For LO phonon modes, the FWHM value decreased, with decreasing measurement temperature. FWHM of 2LO peak also decreased as measurement temperature decreased. Measurement temperature was under 200 K, the FWHM values of 2LO peak was constant for different annealing temperature. FWHM values of all peaks during 5 min. annealing are presented in Figure 33.

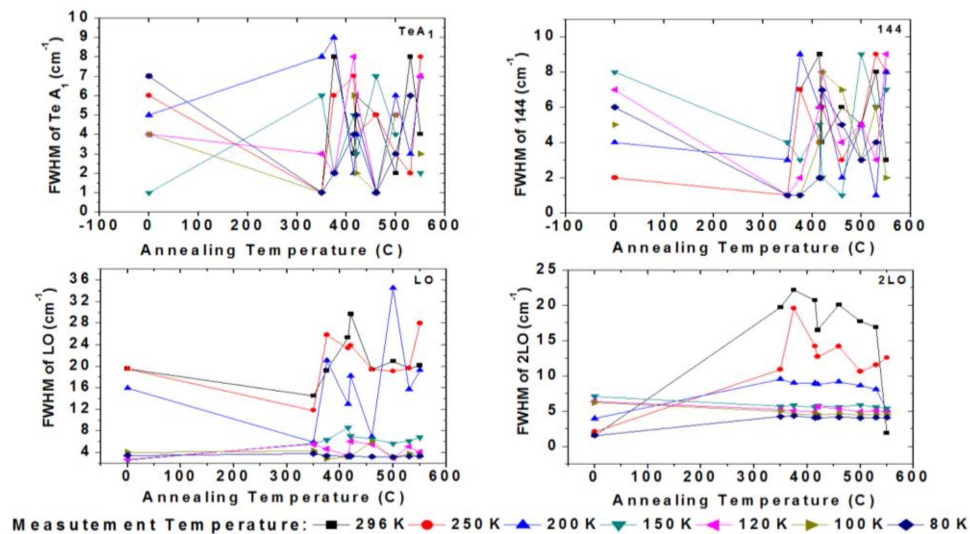

Figure 33. Variation of FWHM value of Te A_1, 144 cm^{-1}, LO and 2LO phonon modes for 5 min. annealed samples.

Te A_1/CdTe LO ratios of 5 min. annealing is displayed in Figure 34. It was observed that Te A_1/CdTe LO ratios decreased with decreasing temperature. For lower measurement temperatures (150 K to 80 K) Te A_1/CdTe LO was nearly zero and it did not change with the annealing temperature for 5 min. For higher measurement, temperature Te A_1/CdTe LO was nearly constant for different annealing temperatures and only at 500°C (annealing temperature) there was an increment.

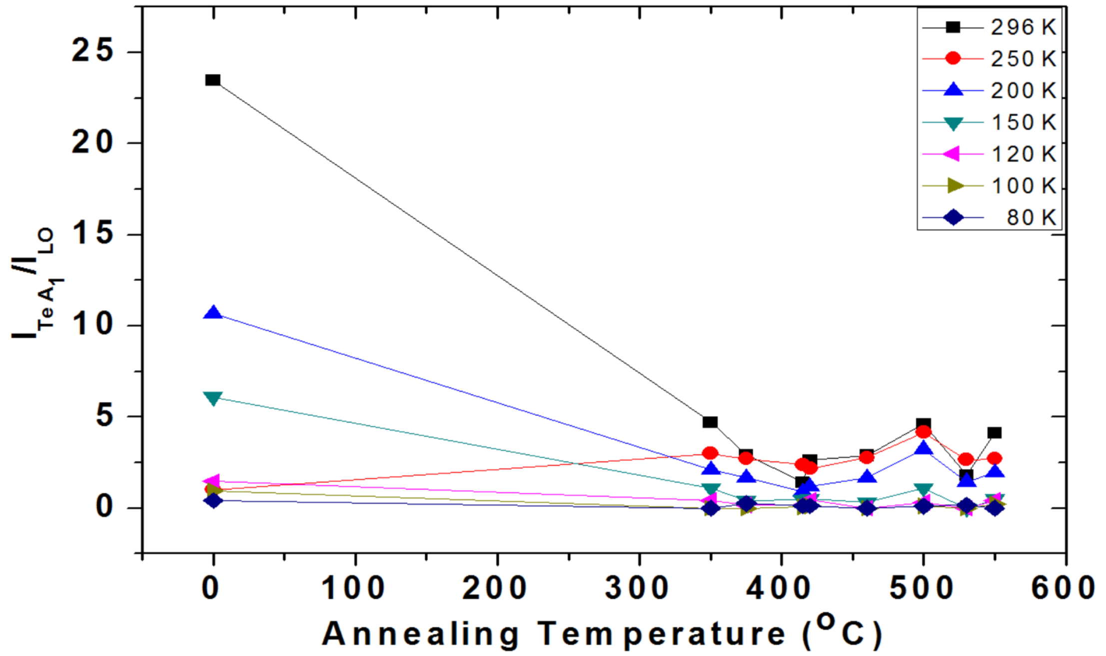

Figure 34. Plot of optic phonon modes $I_{Te\ A1}/I_{LO}$ ratios as a function of annealing temperature of annealed for 5min.

Before annealing TO/LO ratios distributed from 22 to zero and after the 5 min. annealing TO/LO ratios varied nearly from 5 to zero (Figure 35). Under 150 K of measurement temperature, TO/LO ratios did not change according to the annealing temperature. Between room temperature and 200 K of measurement temperature TO/LO ratios showed a rise when the annealing temperature increased from 400°C to 500°C and after the 500°C TO/LO ratio decreased again.

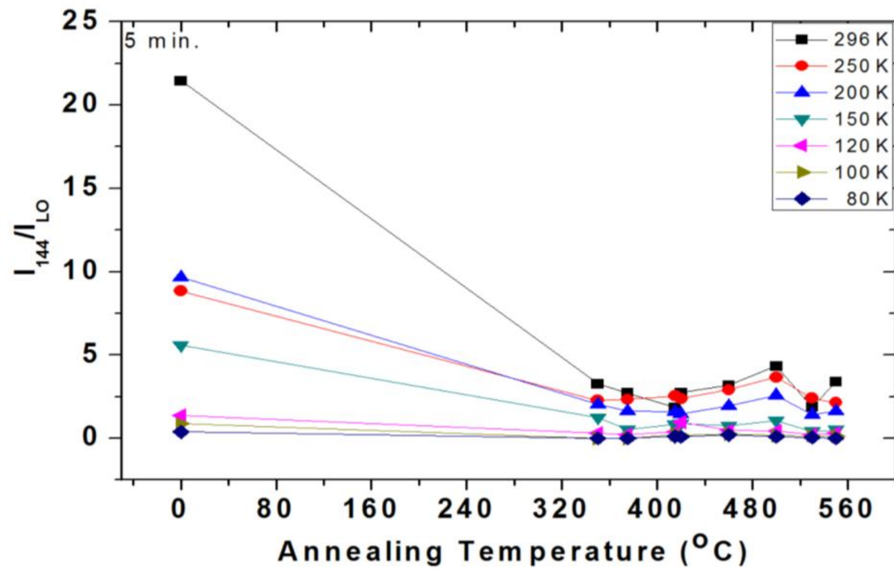

Figure 35. Graph of I_{144}/I_{LO} ratio as a function of annealing temperature. Raman measurement was done with cooling from 296 K to 80 K.

2LO/LO ratios of 5 min. annealing at eight different annealing temperature which were from 350ºC to 550ºC are presented in Figure 36. 2LO/LO ratios decreased from 1.77 to 1.69 at 80 K measurement temperature. 2LO/LO ratios changed from 2.81 to 2.85 at 100 K measurement temperature. 2LO/LO ratios decreased 3.78 to 3.3 at 120 K. 2LO/LO ratios decreased from 5.22 to 4.1 at 150 K. Additionally 2LO/LO ratios decreased 2.25 to 1.05 at 200ºC.

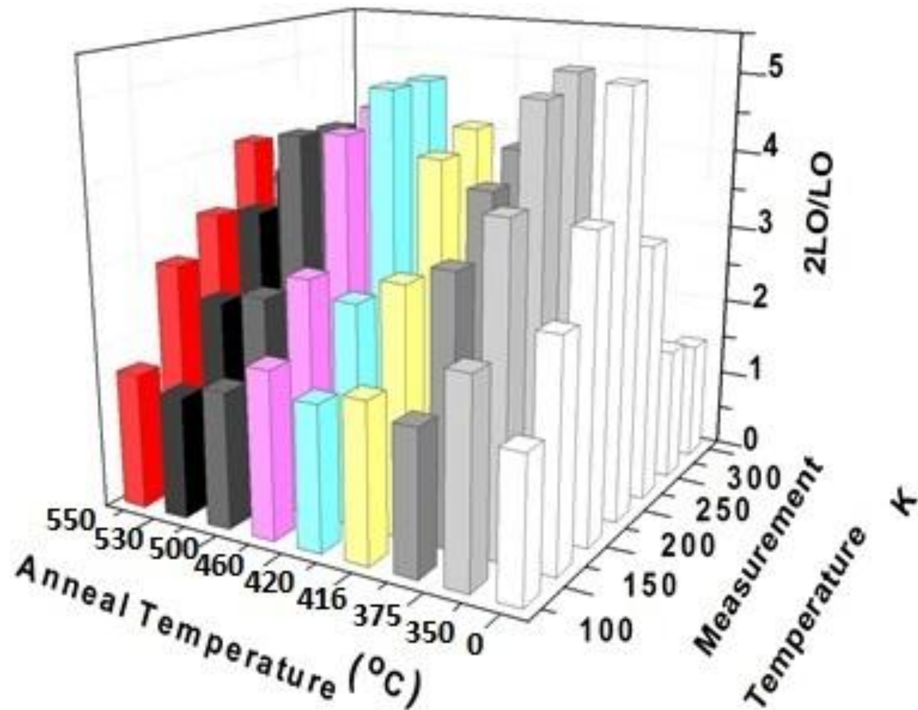

Figure 36. 3D graph of CdTe Raman spectroscopy result's 2LO/LO ratios changing with annealing temperature and Raman measurement temperature.

Lastly, the effects of annealing temperature was investigated for longer time during 20 min. surface morphology are presented in Figure 37 for SEM and Figure 38 for AFM. SEM image showed that CT9-2-AN28 sample evaporated at 420ºC for 20min. under the 20 mTorr vacuum conditions. Roughness of surface increased with increasing temperature (Figure 39). Dislocation density is presented in Figure 41, dislocation density decreased from $8.4x10^{7}$ cm^{-2} to $6.23x10^{7} cm^{-2}$ at 190ºC annealing. Dislocation density was calculated to have a mean value of $7.47x10^{7}$ for annealing at 300 ºC, about $5.15x10^{7}$ for 350 ºC and $8.23x10^{7}$ for 420 ºC (Figure 41).

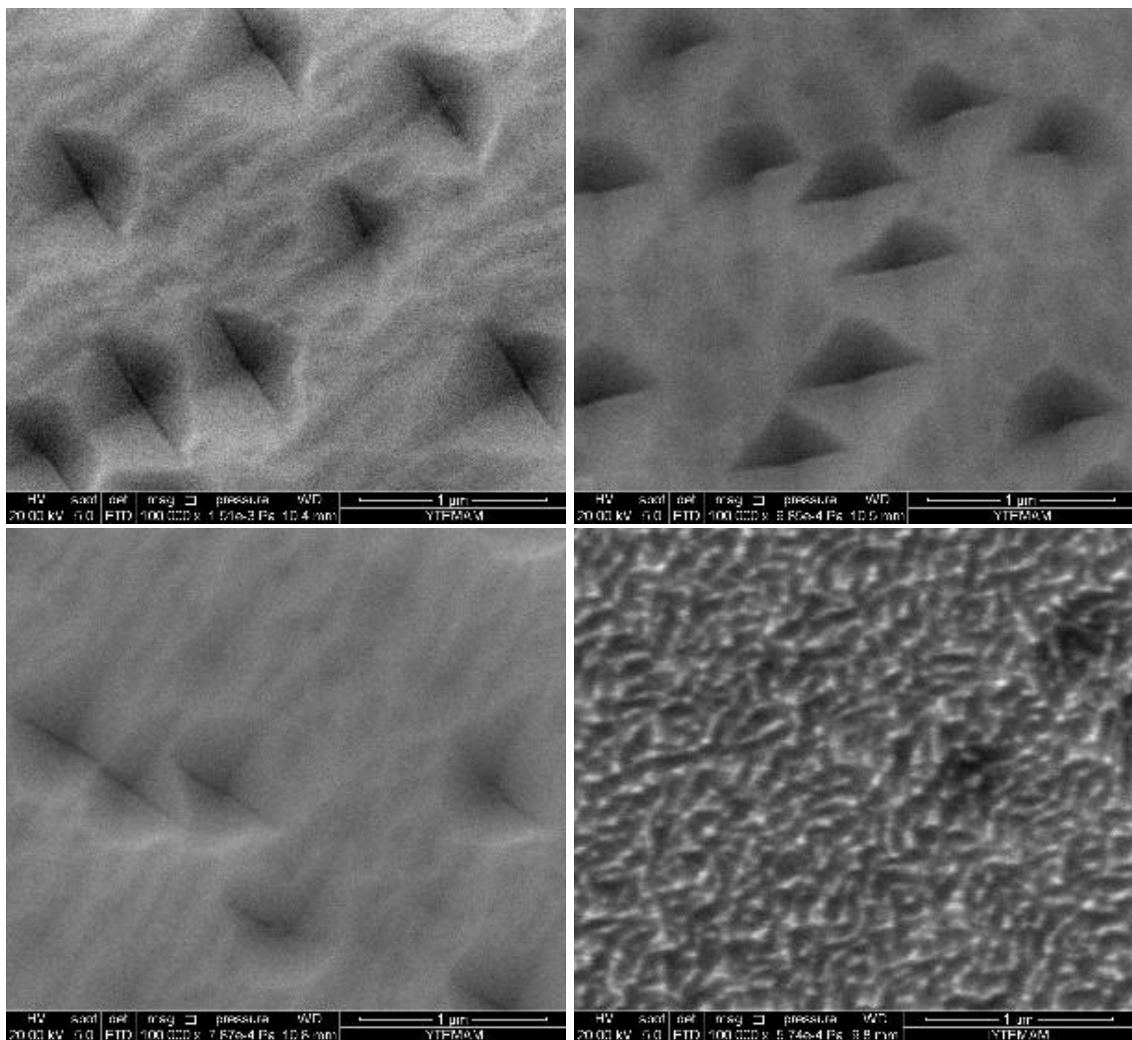

Figure 37. SEM micrograph of annealed for 20 min. a) CT9-2-AN35 at 180ºC, b) CT9-2-AN36 at 300ºC, c) CT9-2-AN37 at 350ºC and d) CT9-2-AN28 at 420ºC samples.

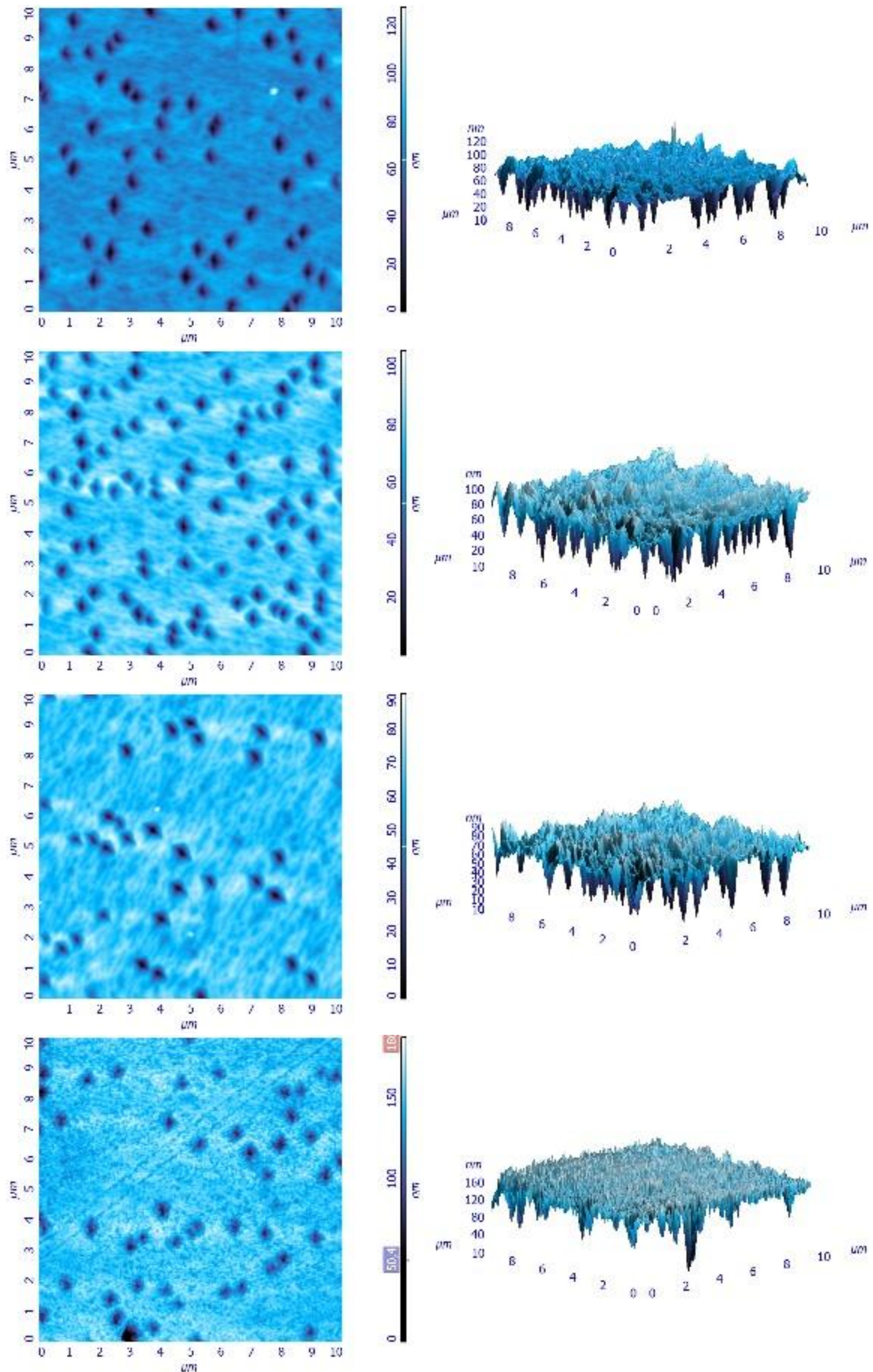

Figure 38. Annealed at 190ºC for 20 min. CT-2-AN35 sample's a) 2D AFM image, b) 3D AFM image. Annealed at 300ºC for 20 min. CT9-2-AN36 sample's c) 2D AFM image, d) 3D AFM image. Annealed at 350ºC for 20 min. CT9-2-AN37 sample's e) 2D AFM image, f) 3D AFM image. Annealed at 420ºC for 20 min. CT9-2-AN28 sample's g) 2D AFM image and h) 3D AFM image.

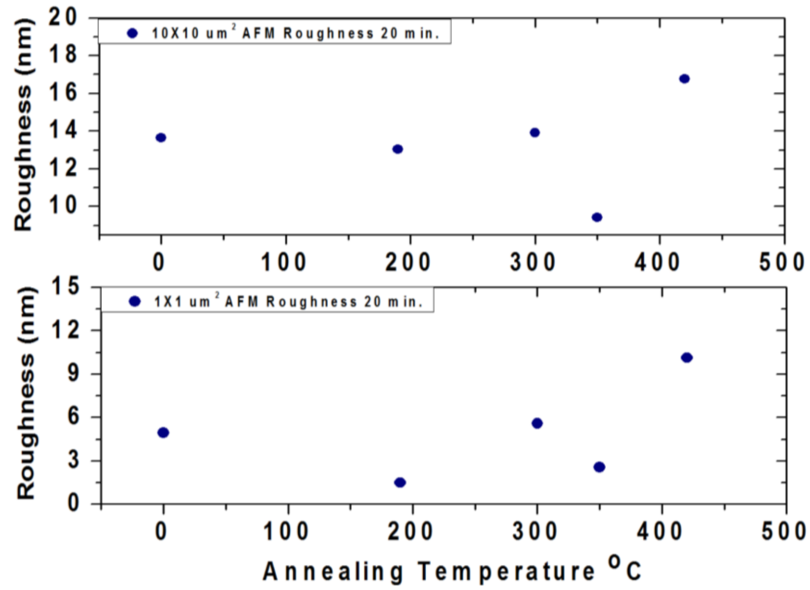

Figure 39. Surface roughness of for 20 min. annealing as a function of annealing temperature from 10x10 um^2 and 1x1 um^2 area.

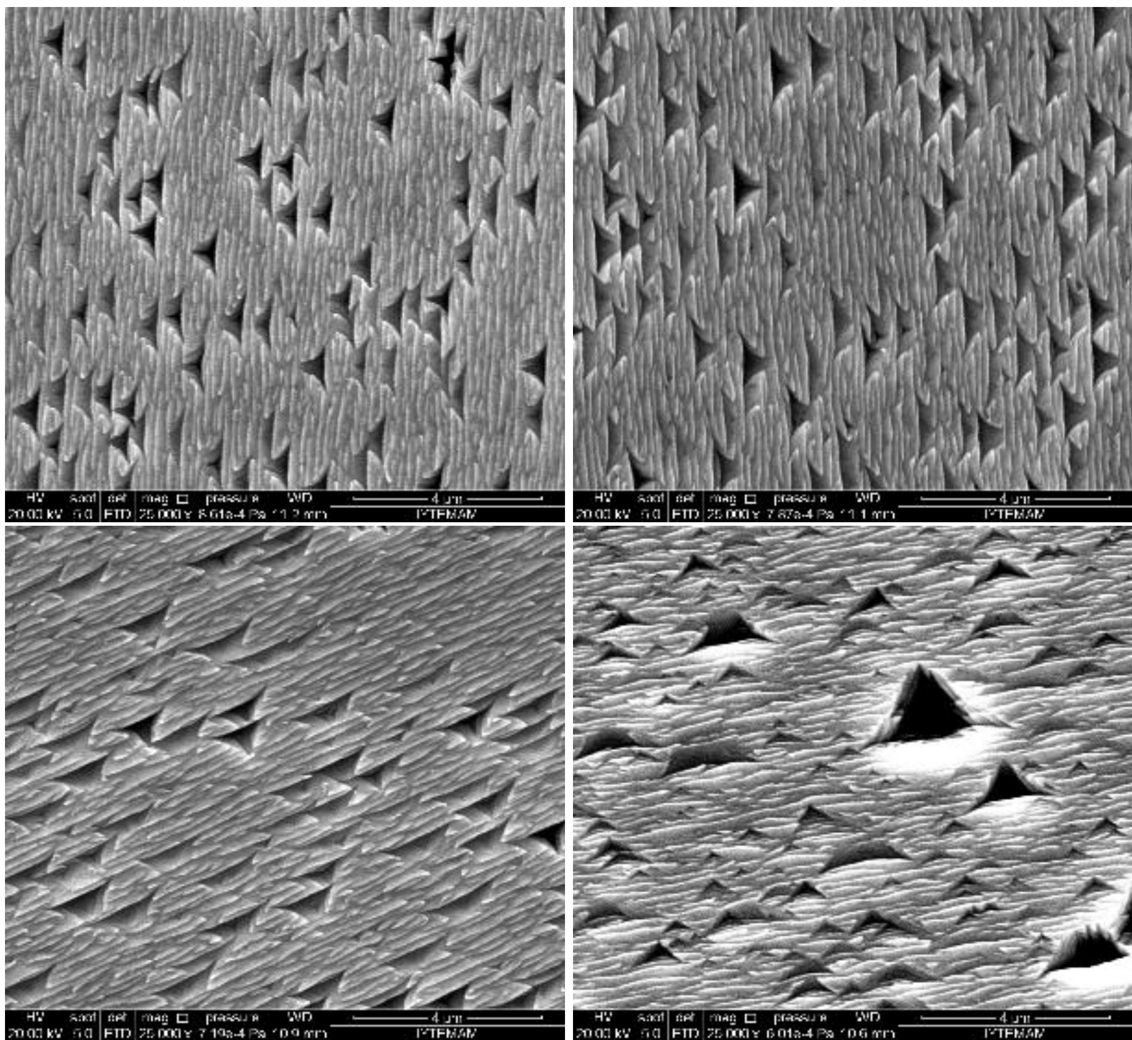

Figure 40. Etched by Everson method a) CT9-2-AN35-E, b) CT9-2-AN36-E, c) CT9-2-AN37-E and d) CT9-2-AN28-E.

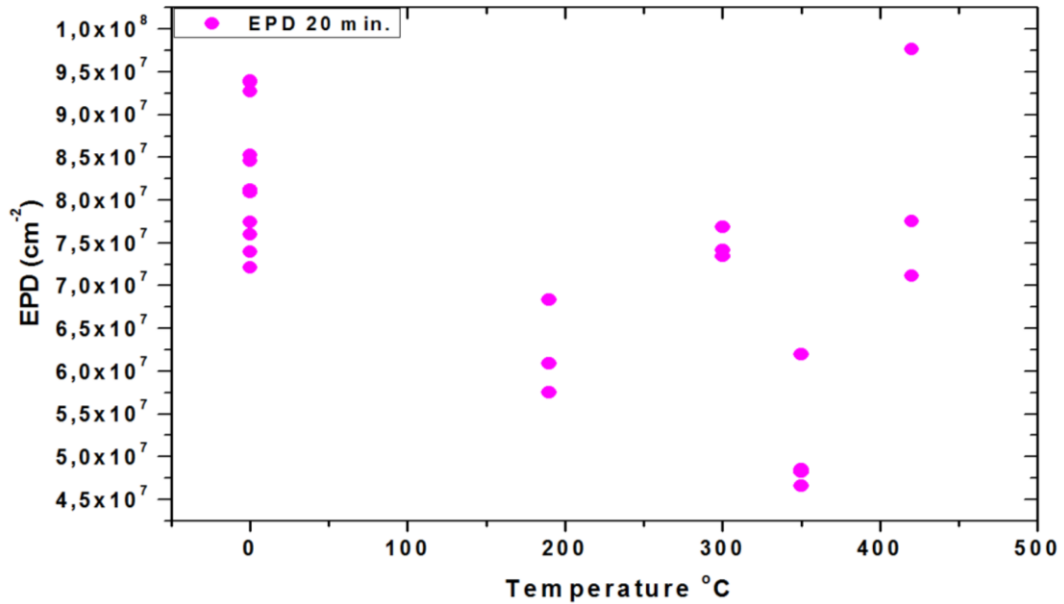

Figure 41. Dislocation densities as a function of annealing temperature. Annealing was for 20 min.

The Raman spectra of annealed samples for 20 min. is displayed in Figure 42. In addition to four well-known peaks, which were Te A_1, 144 cm^{-1}, CdTe LO, CdTe 2LO in this theses, 73 cm^{-1} and 91 cm^{-1} peaks showed significant increment (Figure 42) at 300°C, 350°C and 420°C annealing temperature. Te A_1, 144 cm^{-1}, CdTe LO, CdTe 2LO peak position is presented in Figure 43. Te A_1 line shifted 5 cm^{-1} higher wavenumber while Raman Measurement temperature decreased. While temperature of Raman Measurement decreased, 144 cm^{-1} mode shifted 3 cm^{-1}, CdTe LO shifted 7 cm^{-1} higher wavenumber. CdTe 2LO peak position did not change with regard to Raman Measurement temperature for annealed samples 190 °C, 300 °C and 350 °C. When annealing temperature increase to 300 °C, Te A_1 shifted higher wavenumber and after the 300 °C when annealing temperature increased, Te A_1 shifted again lower wavenumber. Like Te A_1 mode 144 cm^{-1} and CdTe LO phonon modes showed same characteristic with annealing temperature; when annealing temperature increased to 300 °C, 144 cm^{-1} and CdTe LO shifted higher wavenumber and after the 300 °C when annealing temperature increased, 144 cm^{-1} and CdTe LO shifted again lower wavenumber.

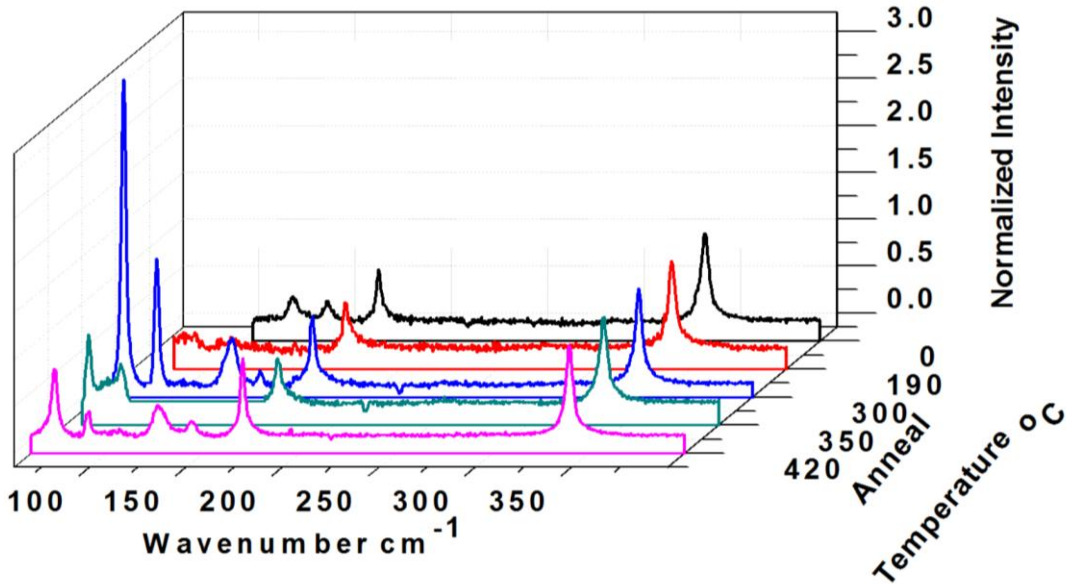

Figure 42. Raman shifts as a function of annealing temperature. Raman measurement were done at 80 K and annealing time was 20 min.

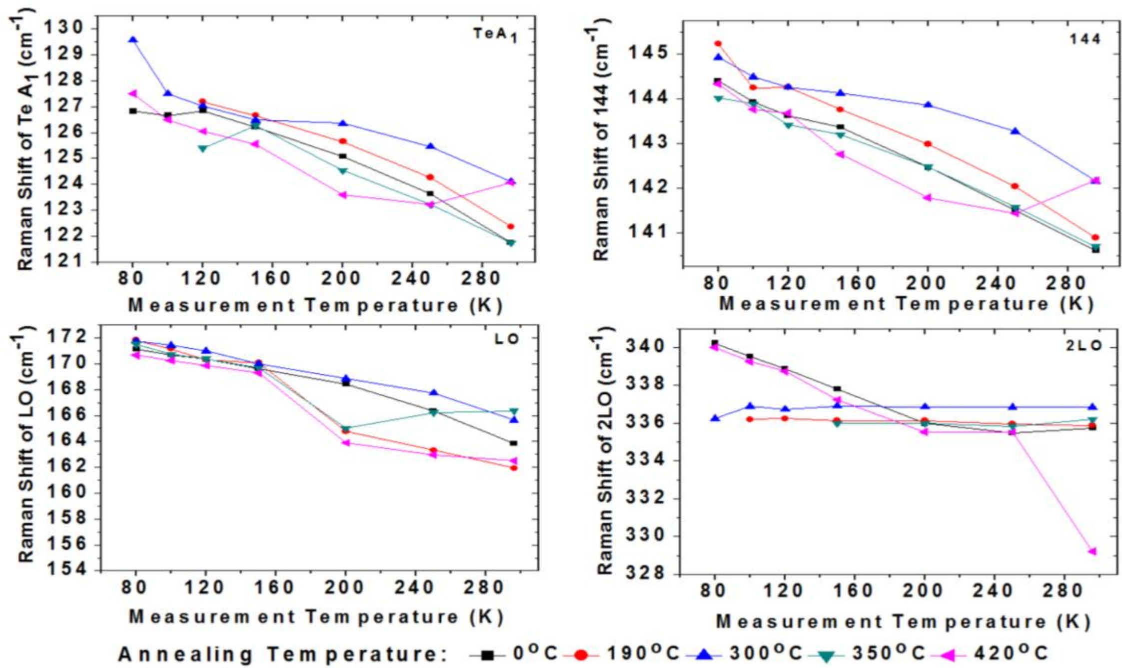

Figure 43. Raman shifts of Te A_1, 144 cm^{-1}, LO and 2LO phonon modes as a function of measurement temperature for 20 min annealed samples at 7 different temperature.

FWHM values of Te A_1 mode decreased from 9 cm^{-1} to 5.5 cm^{-1} when Raman measurement temperature decreased. FWHM value of 144 cm^{-1} mode distributed 8 cm^{-1} to 2 cm^{-1}. FWHM of LO peak decreased, when Raman measurement temperature decreased. FWHM of 2LO peak showed big values for annealed samples at 300ºC and measured at 100 K, 120 K and 150 K (Figure 44).

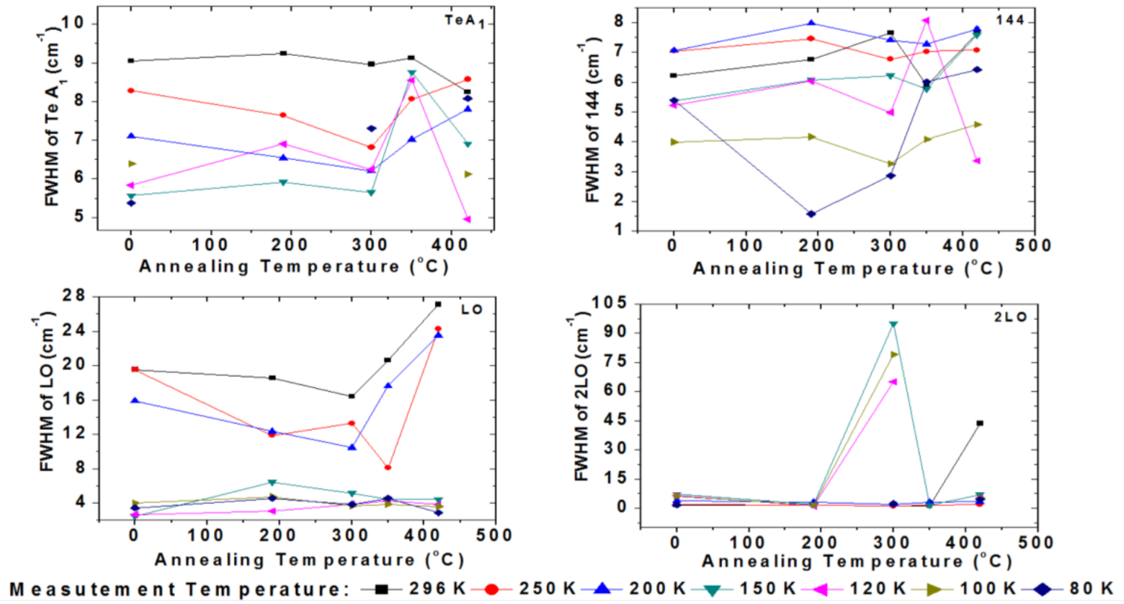

Figure 44. Variation of FWHM value of Te A_1, 144 cm^{-1}, LO and 2LO phonon modes for 20 min. annealed samples.

$I_{Te\ A1}/I_{LO}$ ratios decreased, if Raman measurement temperature decreased and when annealing temperature increased up to 300ºC, $I_{Te\ A1}/I_{LO}$ decreased thought if annealing temperature higher than 300ºC, $I_{Te\ A1}/I_{LO}$ increased again (Figure 45).

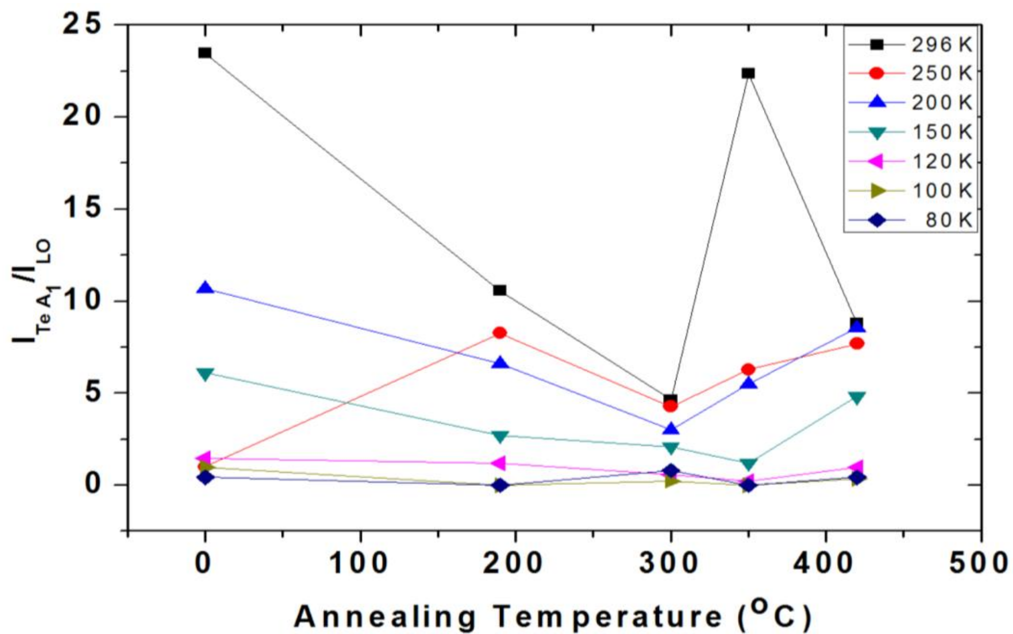

Figure 45. Plot of optic phonon modes $I_{Te\ A1}/I_{LO}$ ratios as a function of annealing temperature of annealed for 20 min.

I_{144}/I_{LO} showed the same characteristic with $I_{Te\ A1}/I_{LO}$, accordingly the peak at 144 cm^{-1} can was Te E mode. The I_{144}/I_{LO} ratios is displayed in Figure 46.

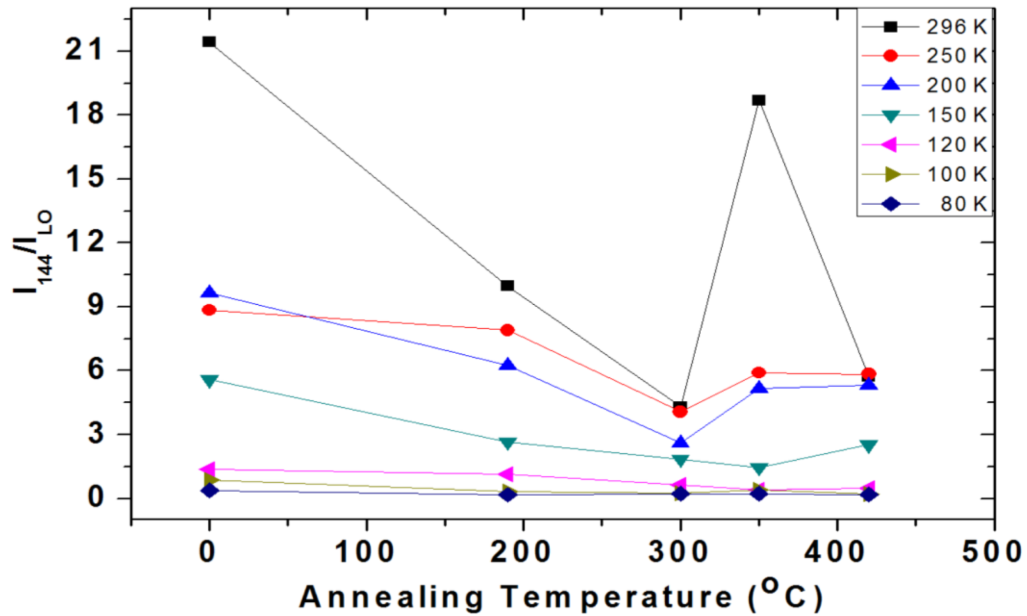

Figure 46. Graph of I_{144}/I_{LO} ratio as a function of annealing temperature. Raman measurement was done with cooling from 296 K to 80 K.

2LO/LO ratios of samples of annealed at 190 °C, 300 °C and 350°C showed different characteristic in contrast to others. At higher Raman measurement temperature, 2LO/LO displayed higher value (Figure 47). Additionally 2LO/LO ratios decreased, when Raman measurement temperature decreased. Sample of annealed at 420°C displayed the same characteristic with as-grown sample and 2LO/LO ratio was 1.16.

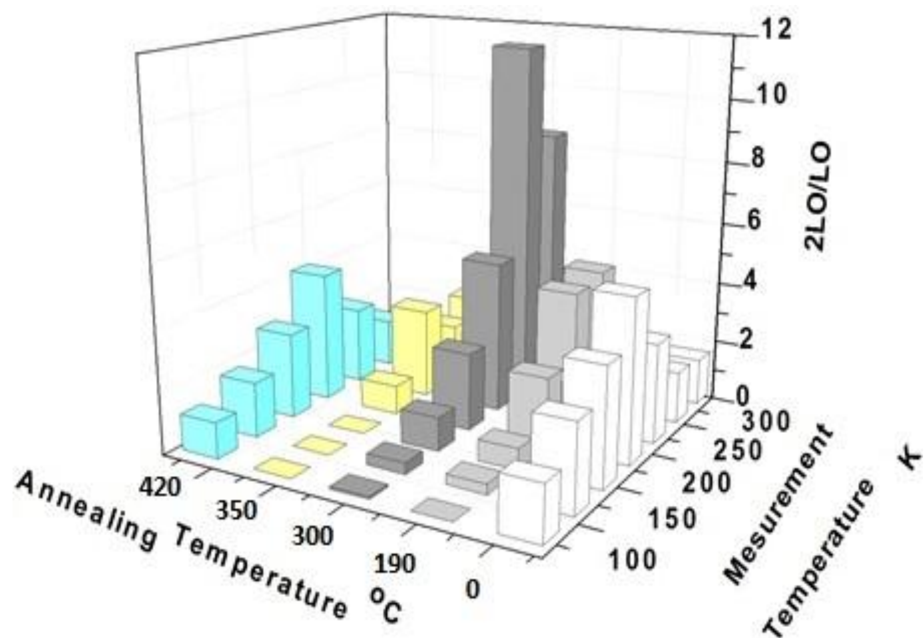

Figure 47. 3D graph of CdTe Raman spectroscopy result's 2LO/LO ratios changing with annealing temperature and Raman measurement temperature.

3.1.2 Effects of Annealing Time

Next, we kept the annealing temperature constant but the effect of varying annealing time was studied. The effect of Annealing time on CdTe/ GaAs thin films was investigated for two different annealing temperatures.

Firstly, annealing heater current was fixed at 0.7 A which corresponds to 400ºC according to the graph given Figure 7. Surface morphology of films after annealing is seen from SEM micrographs as given in in Figure 48. Figure 49 shows the SEM image of samples after etching. For 20 min. at 400ºC annealed sample had a little evaporation as shown in Figure 48 c). Dislocations decreased when time was longer as shown Figure 50.

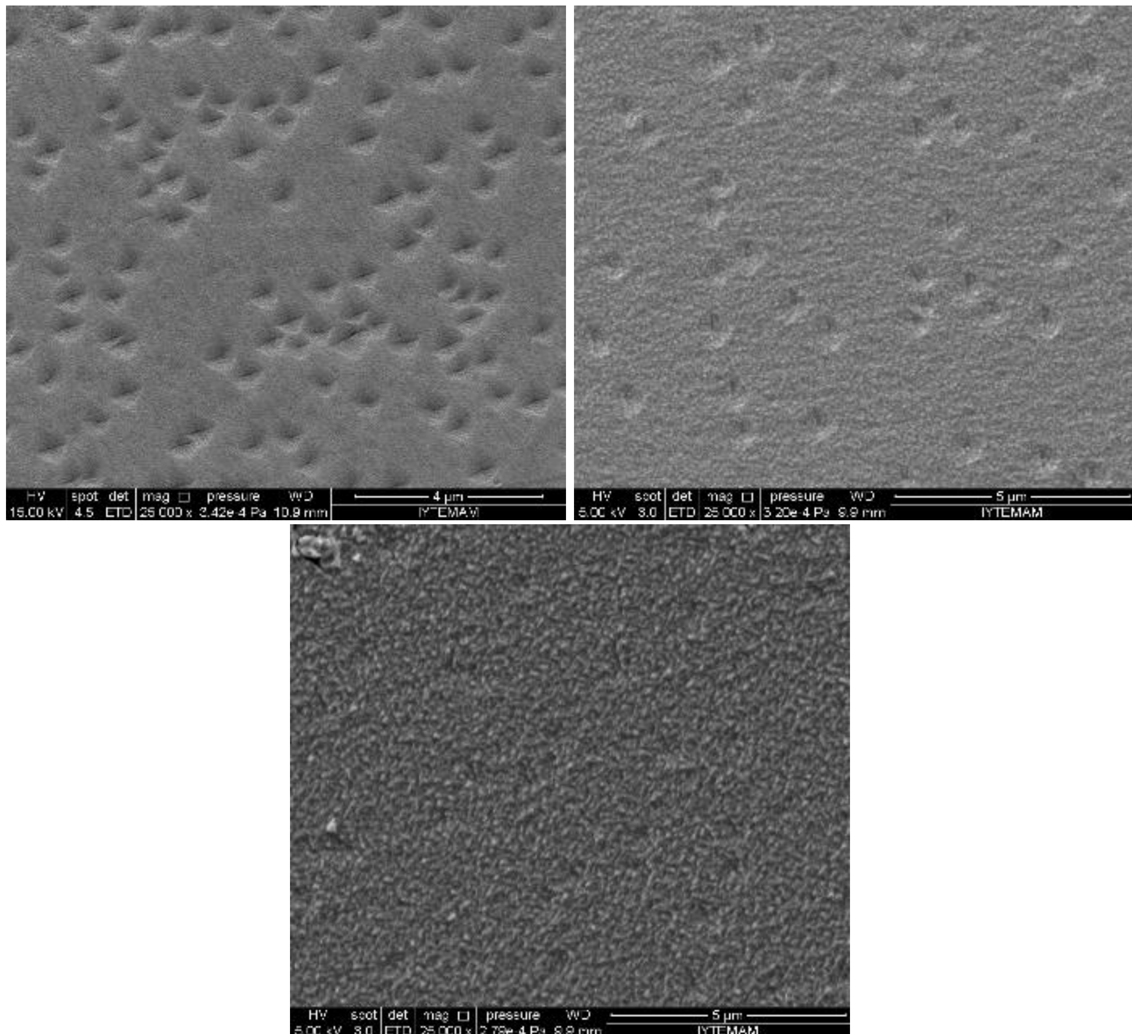

Figure 48. SEM micrograph of annealed at 400ºC a) CT9-2-AN6 for 5 min., b) CT9-2-AN10 for 10 min. and c) CT9-2-AN11 for 20 min.

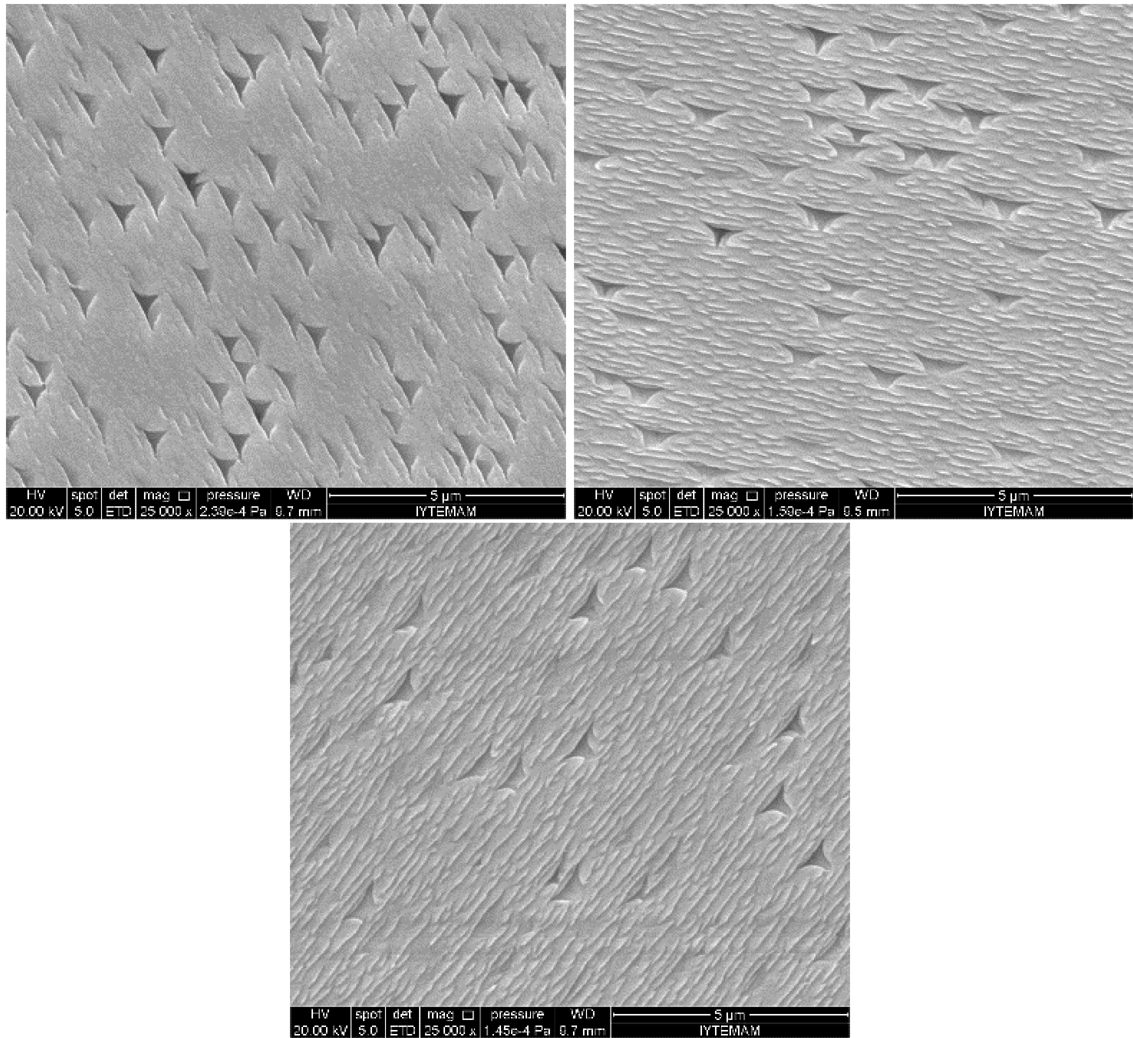

Figure 49. Etched by Everson method a) CT9-2-AN6-E, b) CT9-2-AN10-E, c) CT9-2-AN11-E samples.

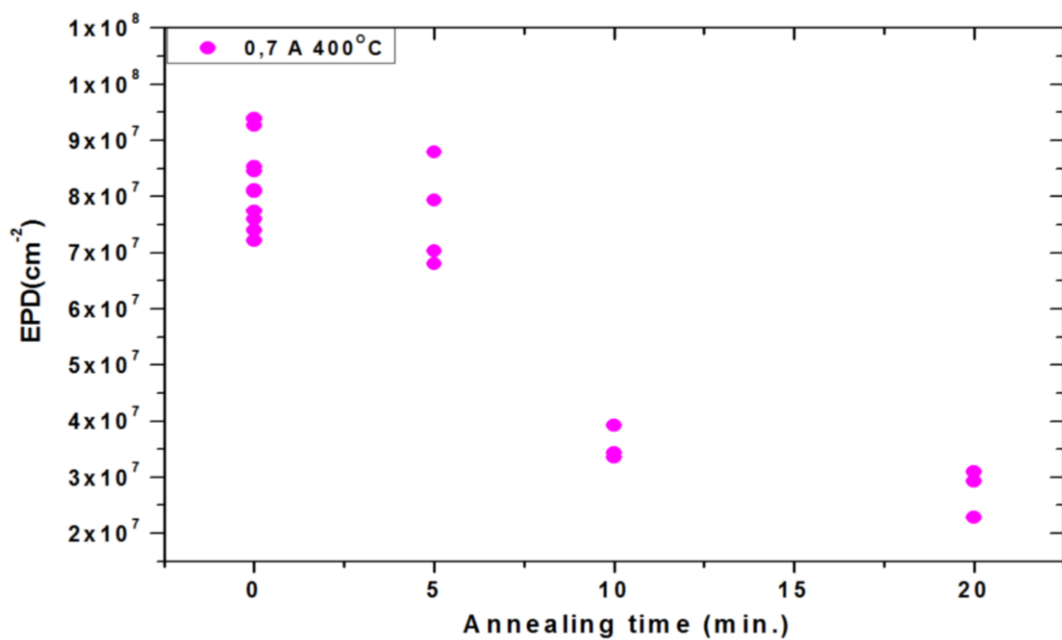

Figure 50. Dislocation densities as a function of annealing time. Annealing was at 400ºC.

Figure 51 compares the Raman spectra of samples annealed at 400 ºC with changing annealing durations. Peaks positions are shown in Figure 52. Te A_1, 144 cm^{-1}, CdTe LO and CdTe 2LO peaks shifted respectively 3 cm^{-1}, 2 cm^{-1}, 7 cm^{-1} and 6 cm^{-1} to higher wavenumber. It seems that there is no clear cut dependence of the peak positions on the annealing durations.

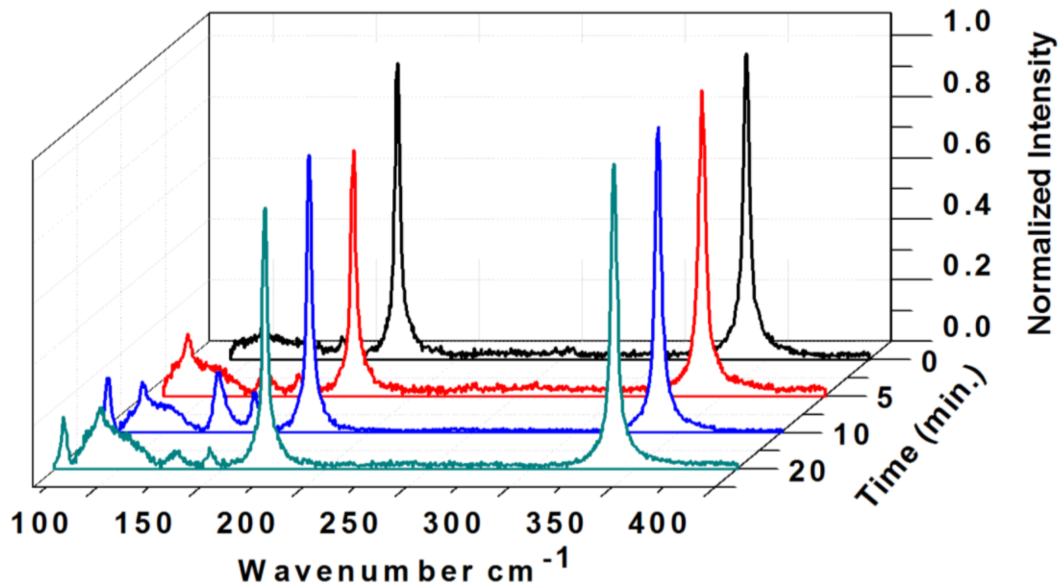

Figure 51. Raman shifts as a function of annealing time of annealed samples at 400ºC. Raman measurements were done at 80 K.

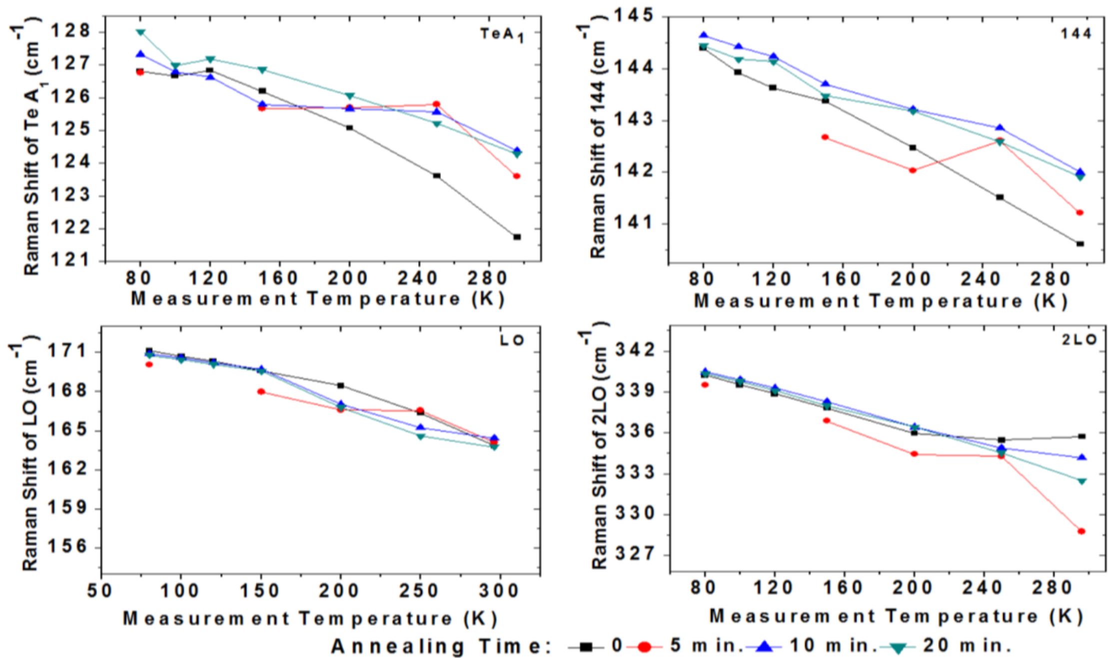

Figure 52. Raman shifts of Te A_1, 144 cm^{-1}, LO and 2LO phonon modes as a function of measurement temperature of annealed samples at 400 ºC.

FWHM of peaks decreased, when the temperature of the samples during the Raman measurement decrease, except for 144 cm^{-1} peak (Figure 53). Annealing time did not effect of FWHM of TeA_1 peak. FWHM of 144 cm^{-1} peak for the as-grown sample increased with annealed after 5 min annealing. But it decreased for the samples with 10 and 20 min. annealing times. FWHM of LO peak was not effect from 5 min. annealing, while it increased for 10 min. annealing and it did not change from 10 min. to 20 min annealing durations. FWHM of 2LO peak after 5 min. annealing increased, decreased again after 10 min. annealing and if annealing time was increased from 10 min. to 20 min. FWHM value did not change.

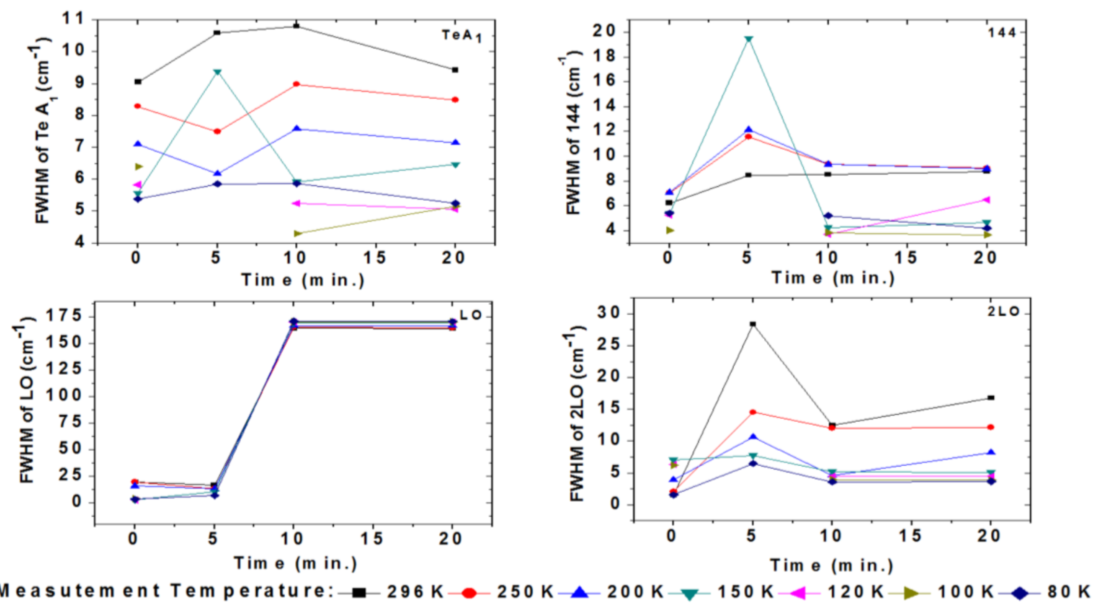

Figure 53. Variation of FWHM value of Te A_1, 144 cm^{-1}, LO and 2LO phonon modes of annealed samples at 400°C.

I_{TeA1}/I_{LO} ratios of as-grown sample distributed from 0 to 23. After annealing, this ratio varied from 0 to 3. I_{TeA1}/I_{LO} ratio decreased when Raman measurement temperature decreased. I_{TeA1}/I_{LO} ratios as a function of annealing time is presented in Figure 54.

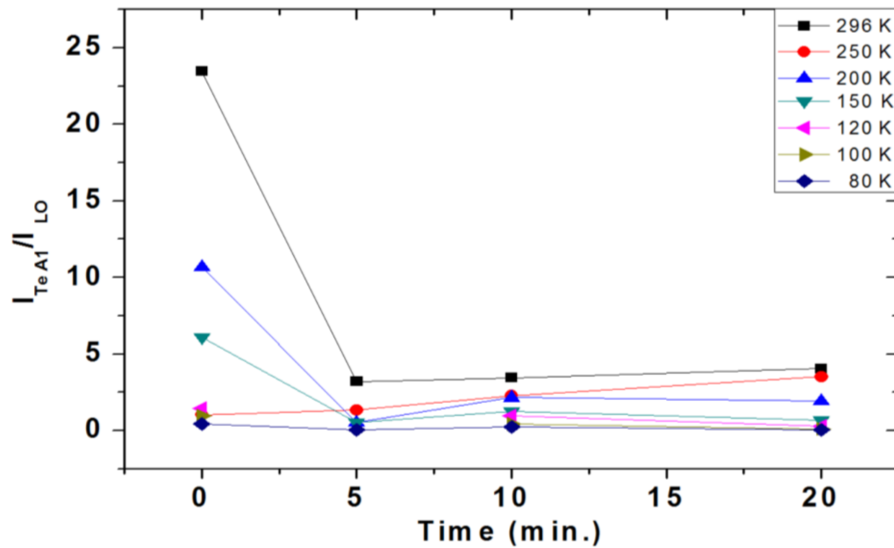

Figure 54. Plot of optic phonon mode's $I_{Te\ A1}/I_{LO}$ ratios as a function of annealing time of annealed at 400°C.

I_{144}/I_{LO} ratios decreased after annealing compared to those of as-grown samples (Figure 55). I_{144}/I_{LO} did not display any dependence on the annealing time. I_{144}/I_{LO} had a very similar feature so that 144 peak can be Te E mode.

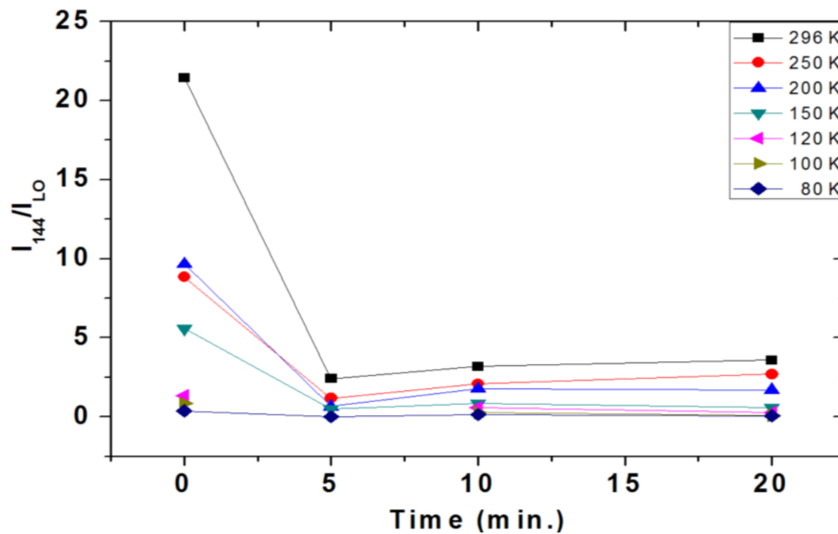

Figure 55. Graph of I_{144}/I_{LO} ratio as a function of annealing time. Raman measurements were done with cooling from 296 K to 80 K.

2LO/LO ratio as function of annealing time and Raman measurement Temperature is displayed in Figure 56. 2LO/LO ratio increased when Raman measurement temperature decreased from 300 K to 150 K. Additionally 2LO/LO ratios decreased again, when temperature decreased from 150 K to 80 K. 2LO/LO ratios as a function of annealing time, 2LO/LO ratios decreased when annealing time increased.

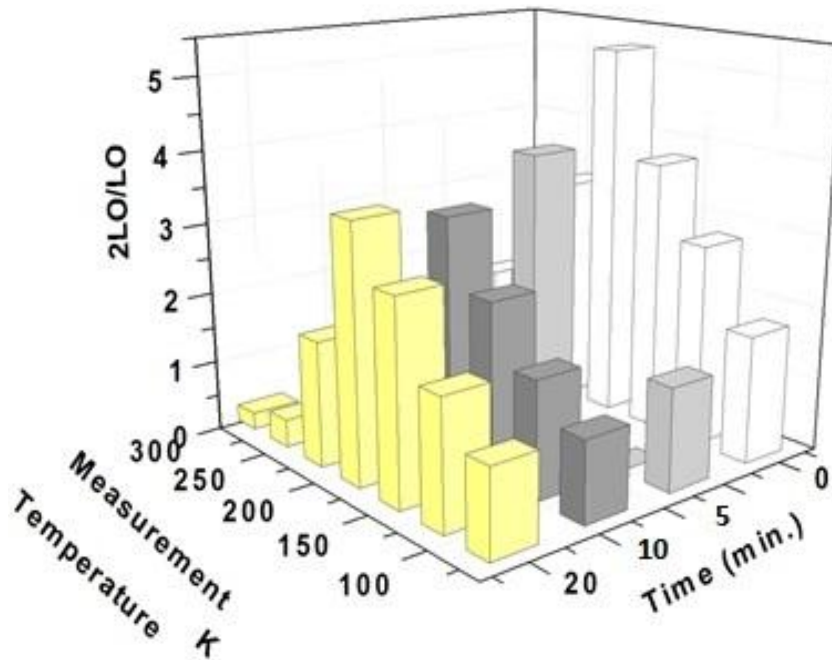

Figure 56. 3D graph of CdTe Raman spectroscopy result’s 2LO/LO ratios changing with annealing time and Raman measurement temperature.

Then, for 0.8 A namely 420ºC 10min. and 20min. was tried. SEM and AFM micrograph is presented in Figure 58, surface roughness are illustrated in Figure 59. Surface roughness decreased, when sample was annealed during 10 min. The surface roughness is increased for the sample annealed for 20min.,Figure 60 shows the annealing time effects of dislocation densities for 0.8A current. For 10 min annealing dislocation density decreased but for 20min. annealing dislocation density increased.

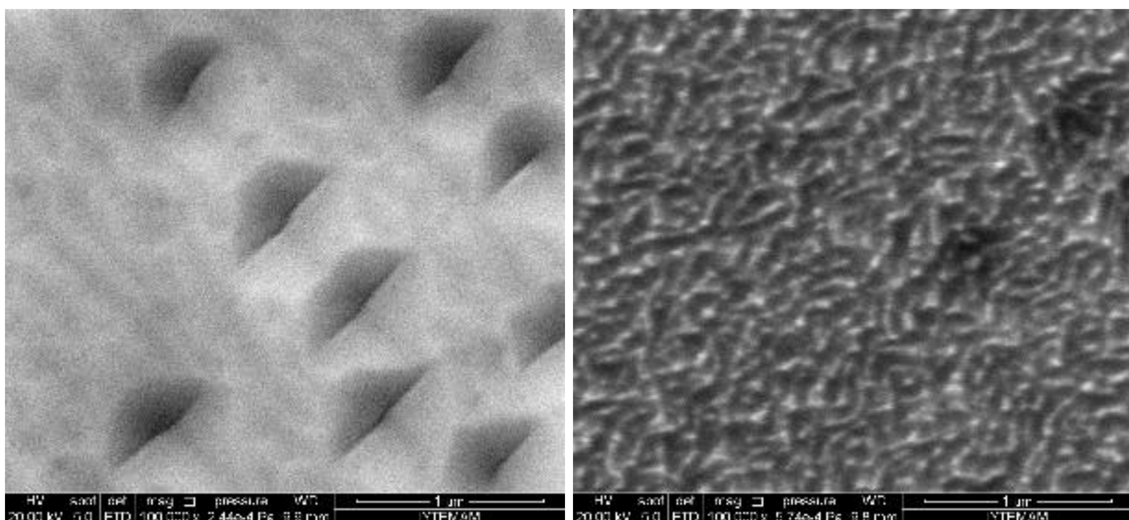

Figure 57. SEM micrograph of annealed samples at 420ºC a) CT9-2-AN32 for 10 min. and b) CT9-2-AN28 for 20 min.

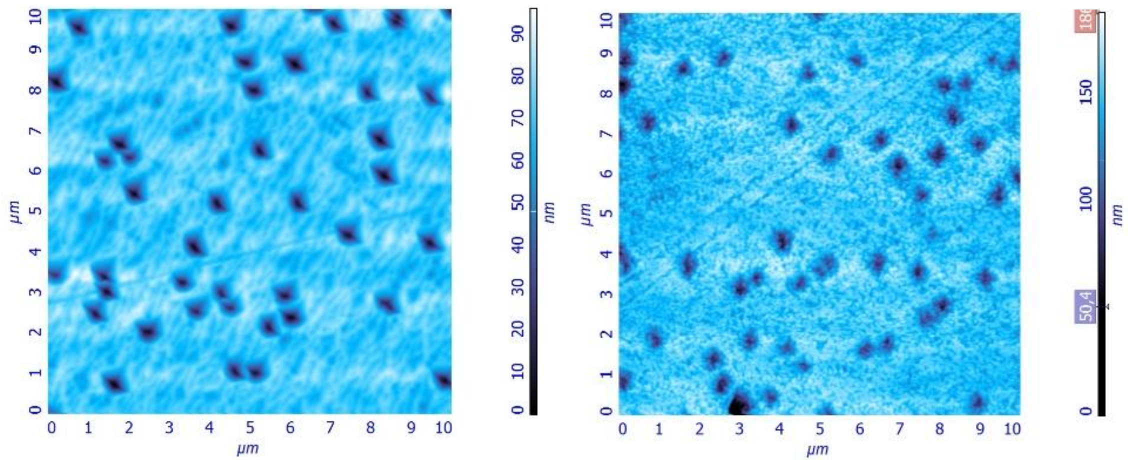

Figure 58. a) AFM 2D images from 10x10um^2 area of CT9-2-AN32 and b) AFM 2D from 10x10 um^2 area image of CT9-2-AN28 samples.

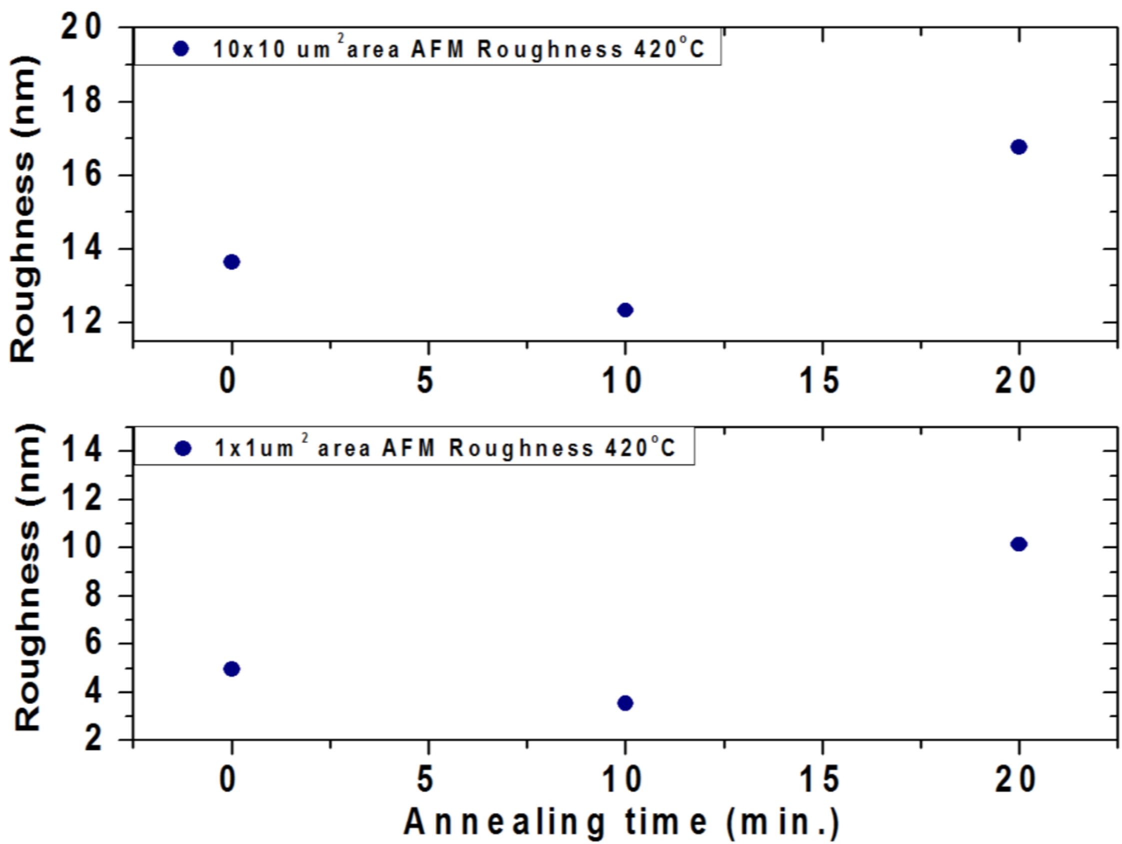

Figure 59. Surface roughness of annealed samples at 420ºC as a function of annealing time from 10x10 um^2 and 1x1 um^2 area.

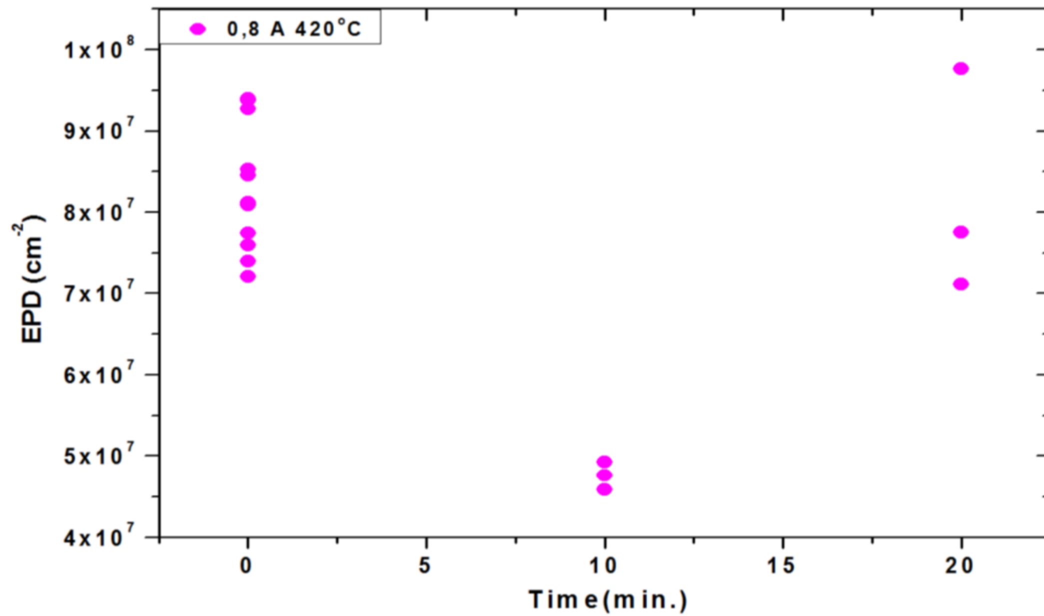

Figure 60. Dislocation densities as a function of annealing time. Annealing was at 420ºC.

Raman spectra of annealed samples shown for various annealed times in Figure 61, the Raman measurement was done at 80 K. Peak positions variation is displayed in Figure 62 and Te A_1 and 144 cm^{-1}phonon line shifted 5cm^{-1} higher wavenumber when Raman measurement temperature decreased. LO line shifted from 168 cm^{-1} to 172 cm^{-1} for 10 min. annealing and LO line shifted from 162 cm^{-1} to 171 cm^{-1} when Raman measurement temperature decreased. 2LO line did not change with Raman measurement temperature.

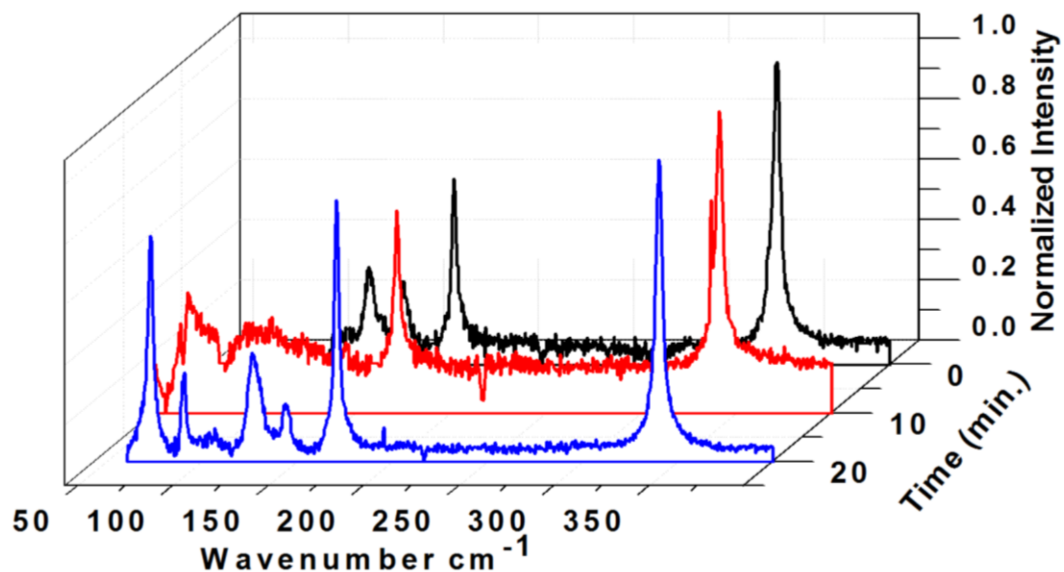

Figure 61. Raman shifts as a function of annealing time of annealed samples at 420ºC. Raman measurement were done at 80 K.

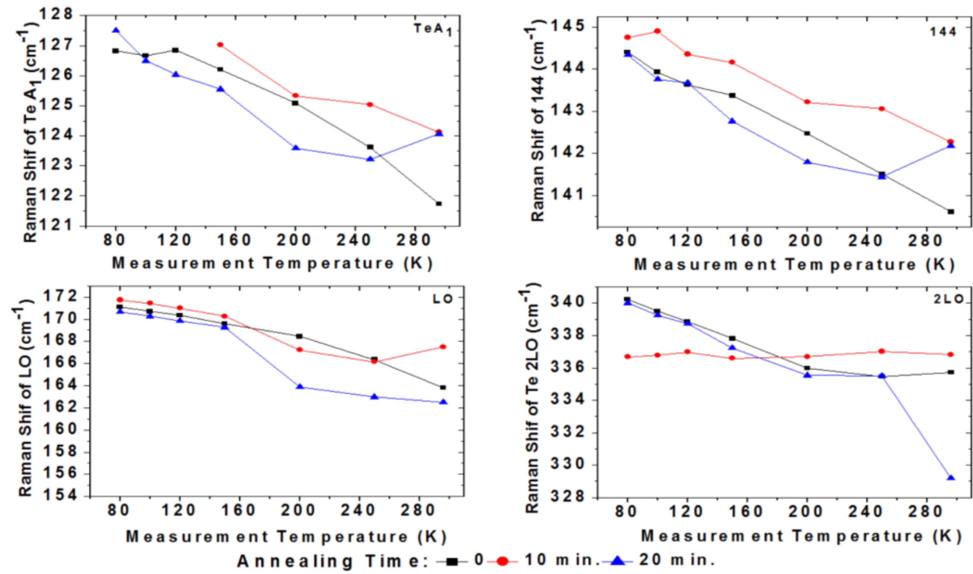

Figure 62. Raman shifts of Te A_1, 144 cm^{-1}, LO and 2LO phonon modes as a function of measurement temperature of annealed samples at 420 ^{o}C.

FWHM value of Te A_1 peak did not change with annealing time at 296 K, 250 K, 200 K, 150 K and 120 K Raman measurement temperature. FWHM values of 144 cm^{-1}, LO did not show any relation with annealing temperature. FWHM of 2LO peak decreased for 10 min. annealing and increased again 20 min. annealing (Figure 63).

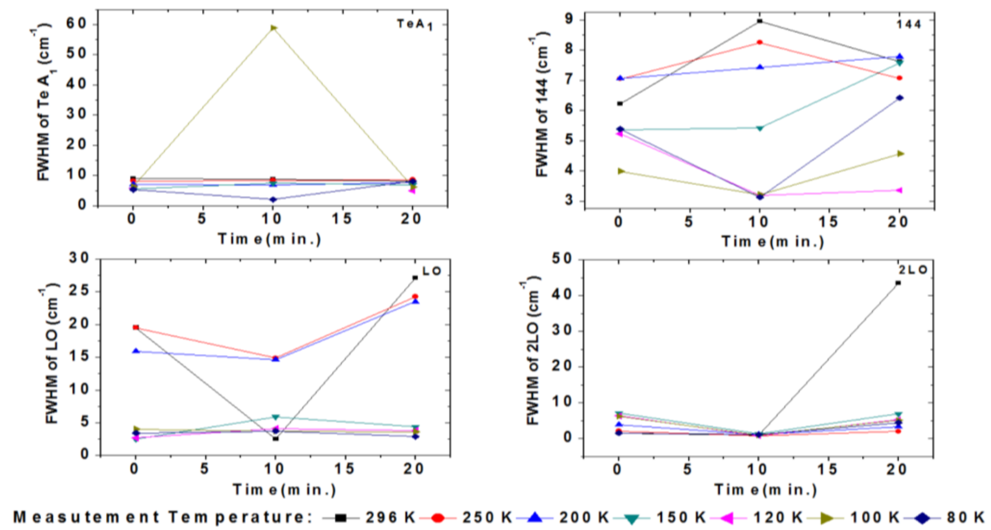

Figure 63. Variation of FWHM value of Te A_1, 144 cm^{-1}, LO and 2LO phonon modes of annealed samples at 420°C.

Variation of I_{TeA1}/I_{LO} ratios decreased after the annealing and I_{TeA1}/I_{LO} ratios decreased when Raman measurement temperature decreased (Figure 64). In this way Te precipitation can be reduced with annealing. This result encouraged other study [28] which concluded the Te peak disappeared after annealing.

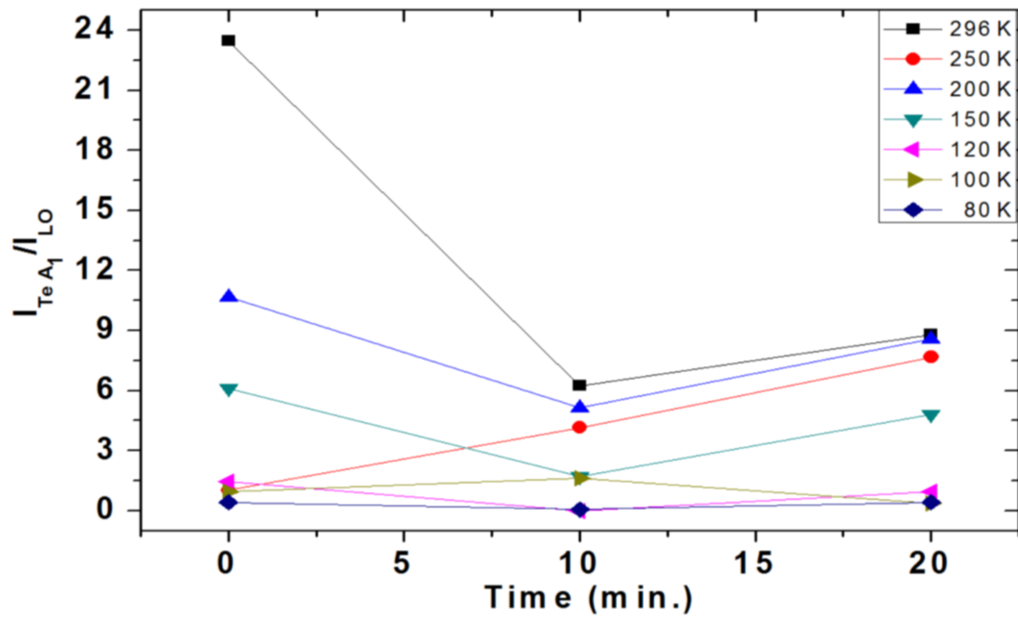

Figure 64. Plot of optic phonon mode's $I_{Te\ A1}/I_{LO}$ ratios as a function of annealing time of annealed at 420ºC.

Variation of I_{144}/I_{LO} ratios decreased after annealing like I_{TeA1}/I_{LO} (Figure 65). In addition this, I_{144}/I_{LO} decreased when Raman measurement temperature decreased. I_{144}/I_{LO} and I_{TeA1}/I_{LO} displayed very similar characteristic, this intensified that 144 peak can be Te E mode.

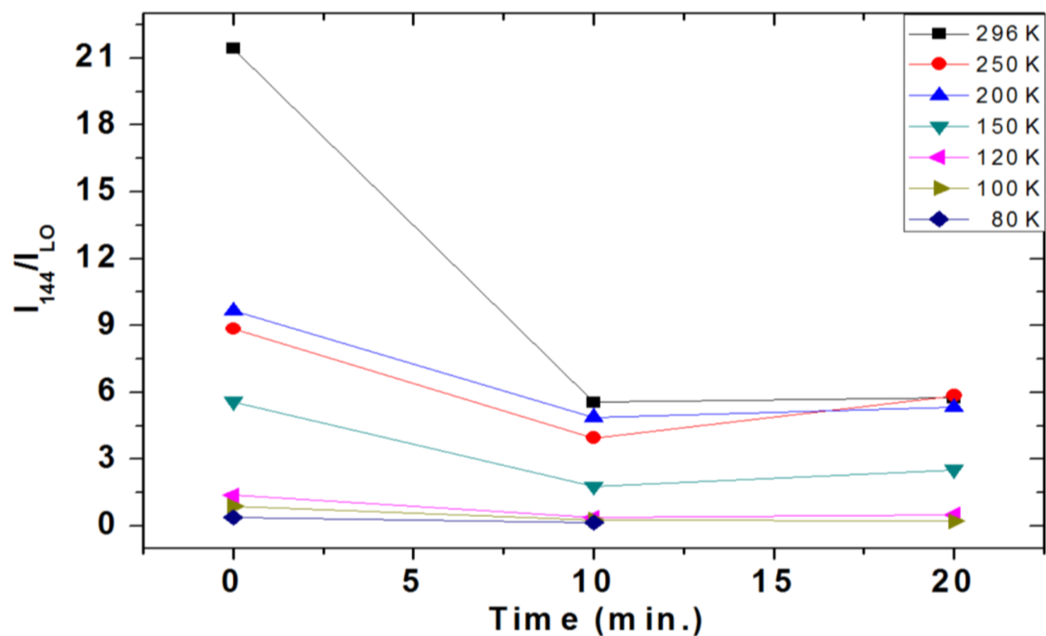

Figure 65. Graph of I_{144}/I_{LO} ratio as a function of annealing time. Raman measurement was done with cooling from 296 K to 80 K.

2LO/LO ratios is illustrated in Figure 66 annealed samples at 420°C. Sample of annealed for 10 min. displayed high ratio of 2LO/LO.

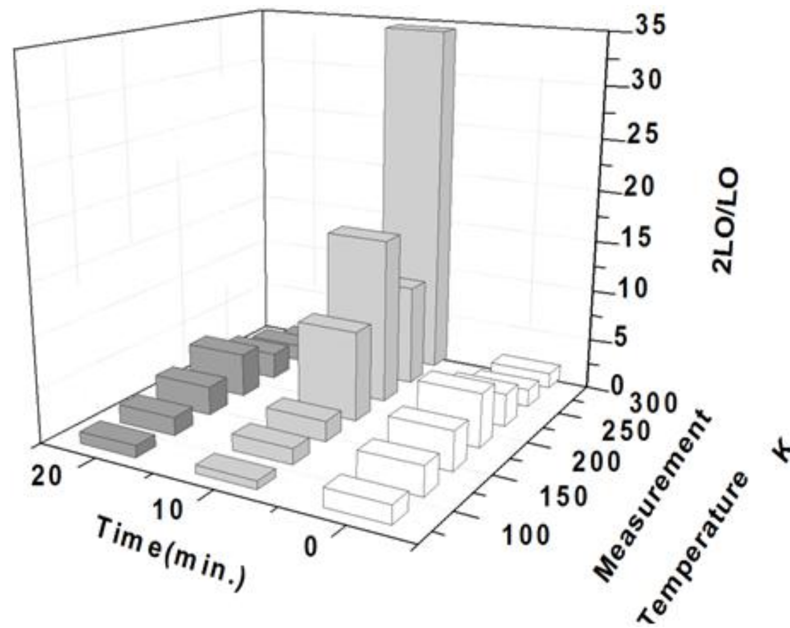

Figure 66. 3D graph of CdTe Raman spectroscopy result's 2LO/LO ratios changing with annealing time and Raman measurement temperature.

3.1.3 Effects of Annealing Cycle

This section includes cyclic annealings. The cyclic annealings were done by using the directly heating and cooling procedures. Annealing temperature was 420°C (0.8 A). Total annealing temperature was kept constant.

Firstly, 420°C temperature was chosen as a starting of evaporation parameter and total annealing time was kept 20 min. Since border of the evaporation was curious and for 20 min. annealed sample's surface is displayed in Figure 67a) SEM micrograph and Figure 68 a) AFM micrograph. Surface roughness increased and this affect was seen in Figure 69 for 1 cycle annealing. Small holes were seen on the surface for 2 cycle annealing for 10min. at 420°C Figure 67 b) and surface roughness was decreased (Figure 69). For 4 and 8 cycle annealing there was no changing on the surface morphology (Figure 67 c) and d)) but surface roughness (Figure 69) decreased with increasing number of cycle comparison with as-grown sample. On the other hand, dislocation density did not decrease (Figure 70 and Figure 71) with cyclic annealing at limit of evaporation temperature for 20min.

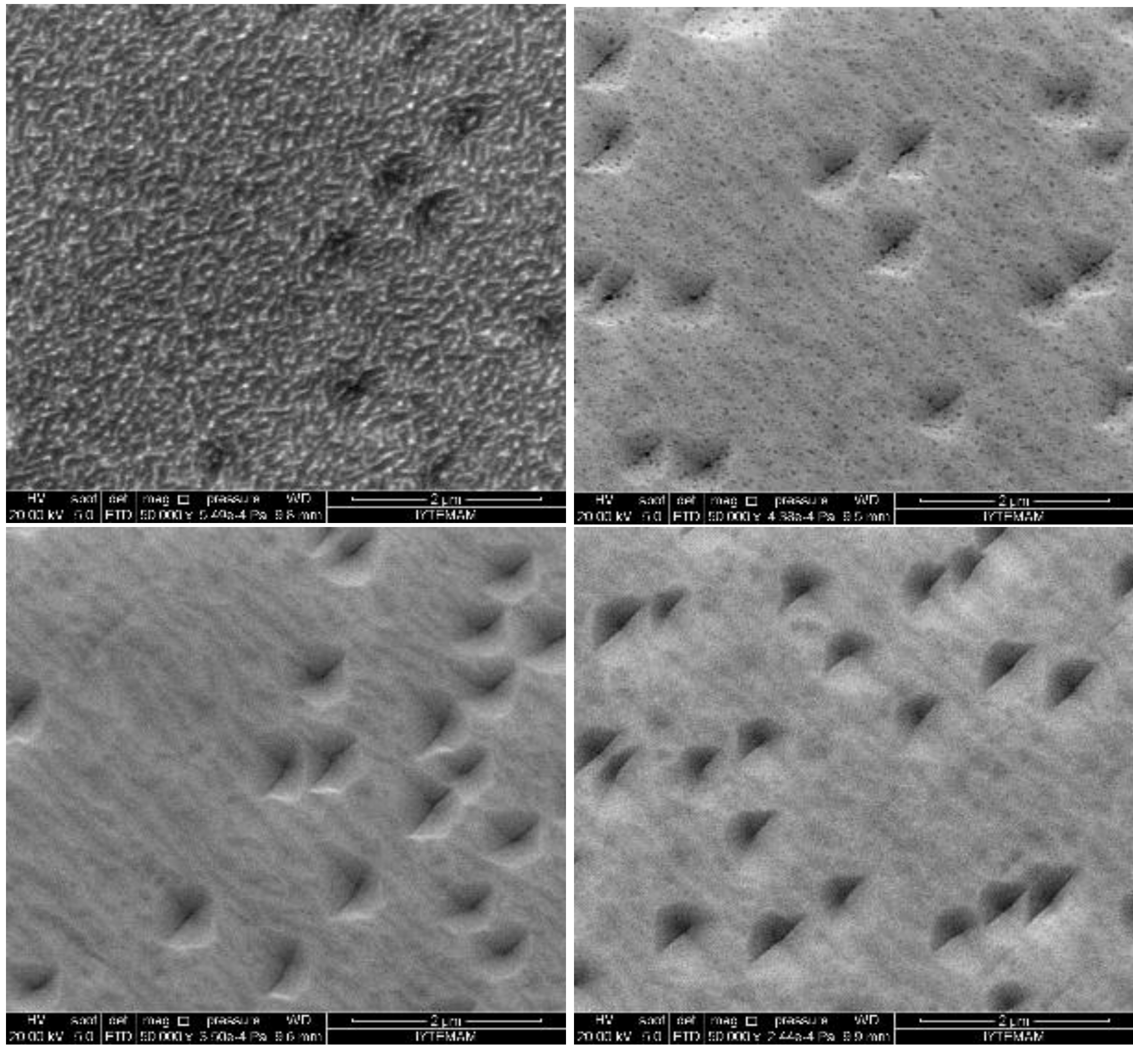

Figure 67. SEM micrograph of cyclic annealed at 420ºC with keeping total anneal time 20 min. a) 1 cycle CT9-2-AN28, b) 2 cycle CT9-2-AN29, c) 4 cycle CT9-2-AN30, and d) 8 cycle CT9-2-AN31 samples.

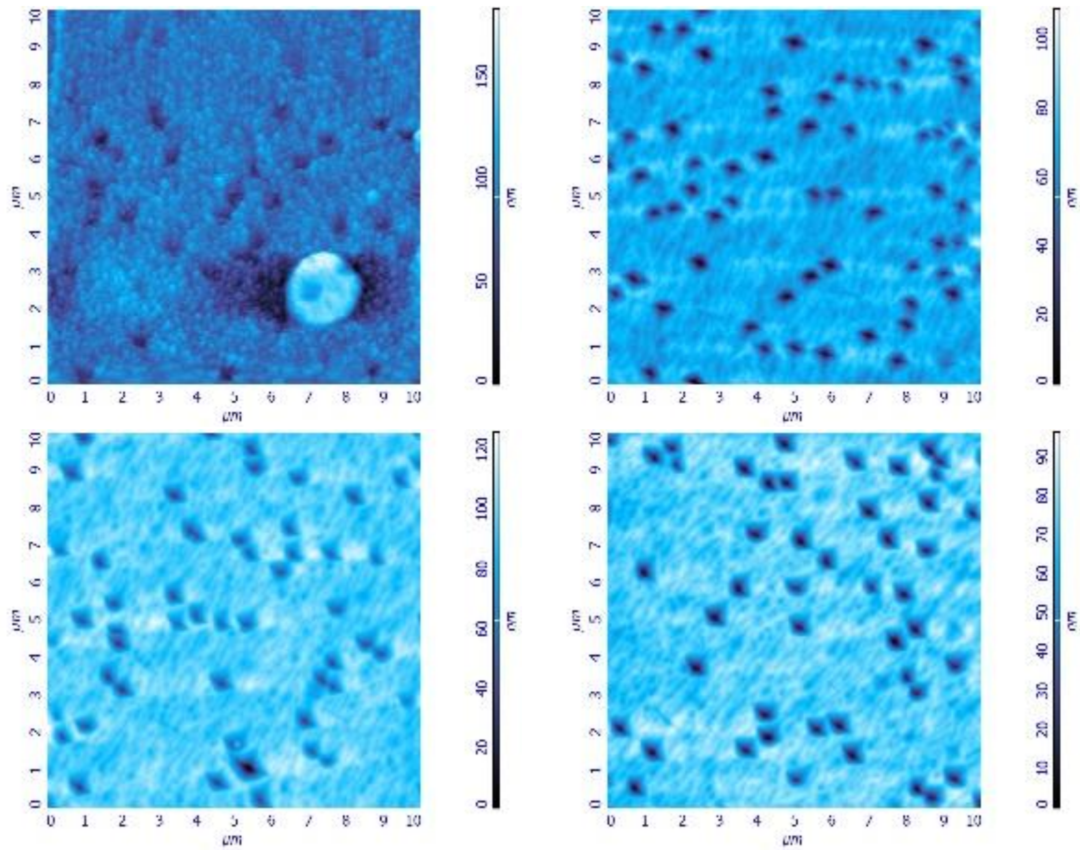

Figure 68. AFM images of cyclic annealed at 420^oC samples from 10x10 um^2 area with keeping total annealing time 20 min. a) CT9-2-AN28 for 1 cycle, b) CT9-2-AN29 for 2 cycle, c) CT9-2-AN30 for 4 cycle and d) CT9-2-AN31 for 8 cycle.

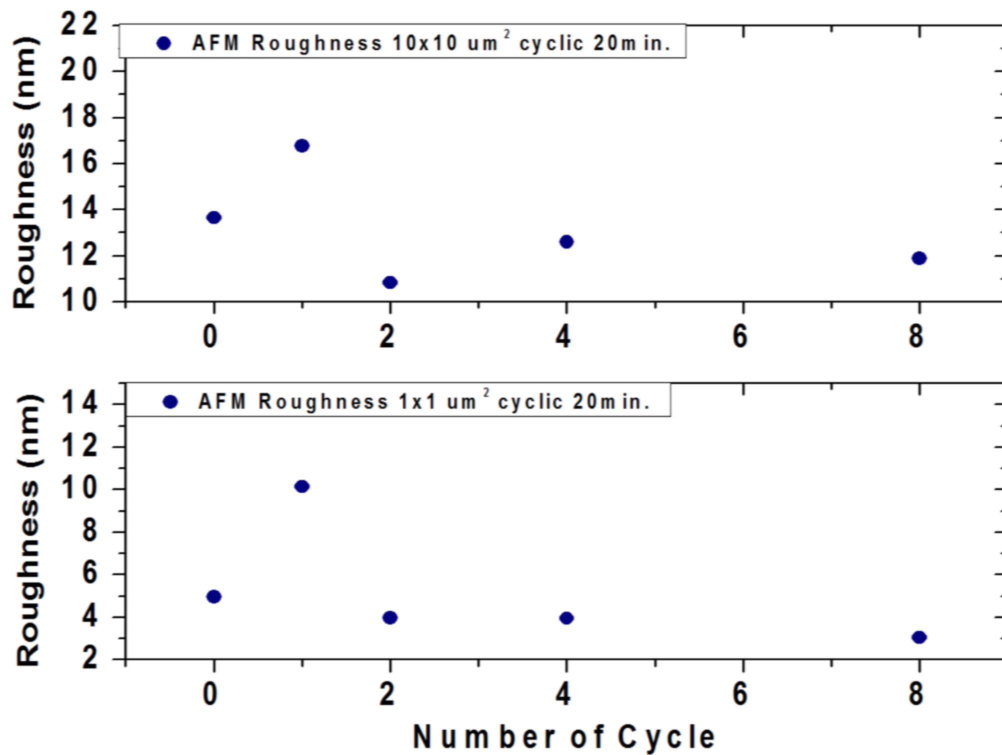

Figure 69. Surface roughness of annealed samples at 420^oC as a function of annealing number of cycle from 10x10 um^2 and 1x1 um^2 area.

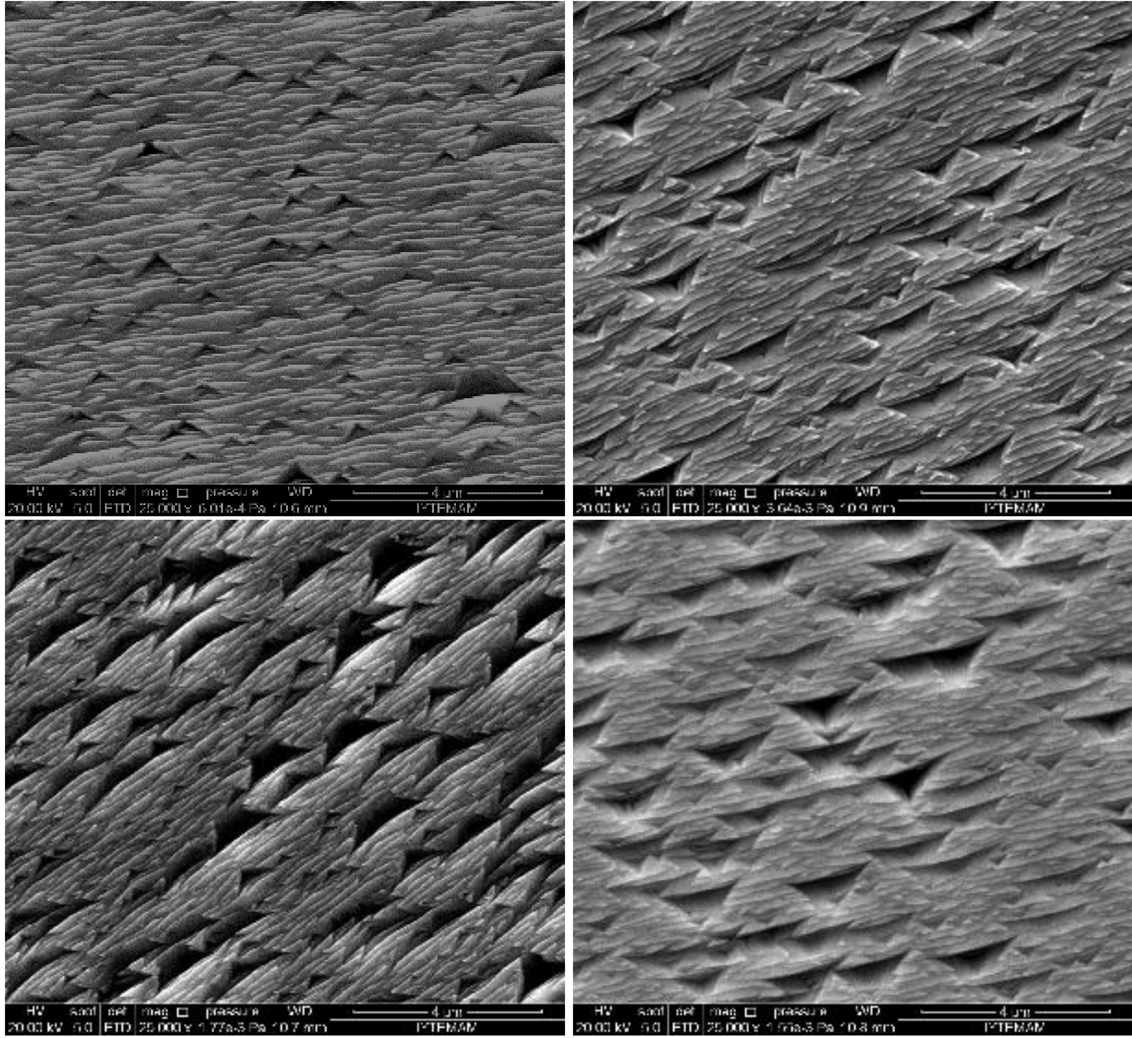

Figure 70. Etched by Everson method for cyclic annealed samples with keeping total time at 20 min. a) CT9-2-AN28-E, b) CT9-2-AN29-E, c) CT9-2-AN30-E and d) CT9-2-AN31-E samples.

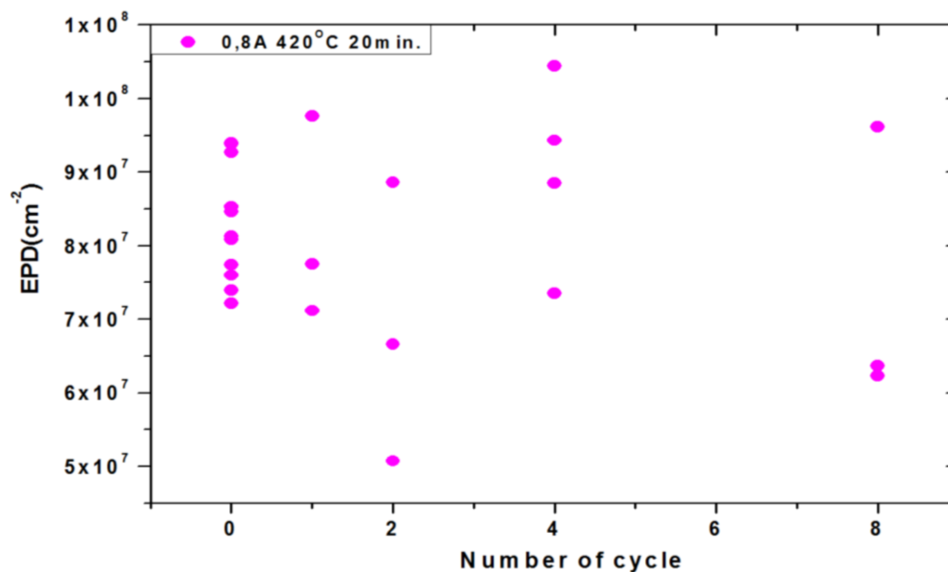

Figure 71. Dislocation densities as a function of annealing cycle. Annealing was at 420ºC and total annealing time was 20 min.

Raman spectra of cycle annealed samples are displayed in Figure 72. Cycle annealed sample's 336 cm^{-1} peak was very sharp and it did not shift with temperature. A cycle annealed sample was given as an example in Appendix A. The 336 cm^{-1} peak can be seen more detailed in Figure 110-Figure 116. At 336 cm^{-1} there might be a peak different from 2LO peak and 2LO peak was embowered by 336 cm^{-1} peak. Peaks shift is displayed in Figure 73. Te A_1 line shifted 5 cm^{-1} from 122 cm^{-1} to 127 cm^{-1} when Raman measurement temperature decreased from 296 K to 80 K. The 144 peak shifted about 3 cm^{-1} from 141 cm^{-1} to 144 cm^{-1}. The LO peak shifted 8 cm^{-1} from 163 cm^{-1} to 171 cm^{-1}. 2LO peak did not shift for annealed during 2 cycle, 4 cycle and 8 cycle according to Raman measurement temperature.

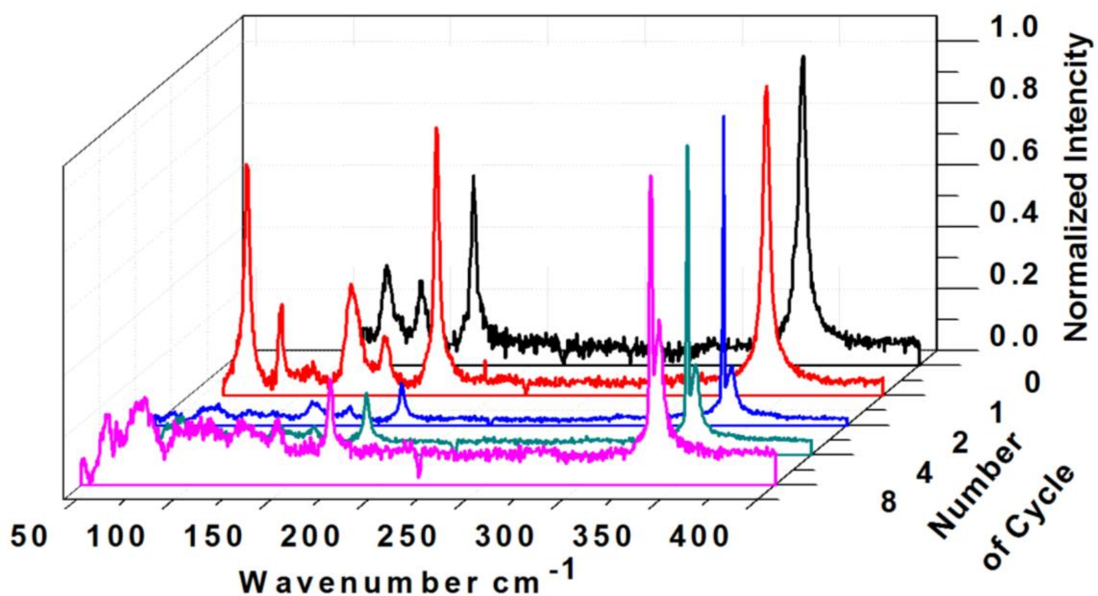

Figure 72. Raman shifts as a function of number of annealing cycle at 420°C. Total annealing time was 20 min. Raman measurement temperature were done at 80 K.

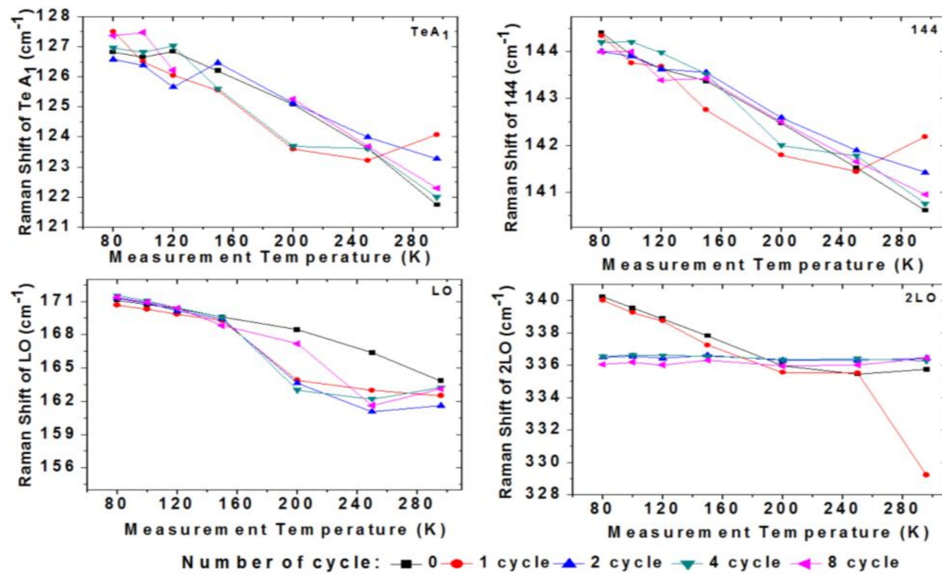

Figure 73. Raman shifts of Te A_1, 144 cm^{-1}, LO and 2LO phonon modes as a function of measurement temperature of cyclic annealed samples at 420 ºC for 20 min total annealing time.

FWHM values of Te A_1 phonons modes variated from 5 cm^{-1} to 10 cm^{-1} but 8 cycle annealed sample's FWHM values variated from 8 cm^{-1} to 25 cm^{-1} (Figure 74). FWHM value of 144 peak variated from 3 cm^{-1} to 9 cm^{-1}. FWHM of LO decreased while Raman measurement temperature decreased. FWHM of 2LO peak after the cycle annealing decreased to nearly 1 cm^{-1} and it did not change with cycle number and Raman measurement temperature.

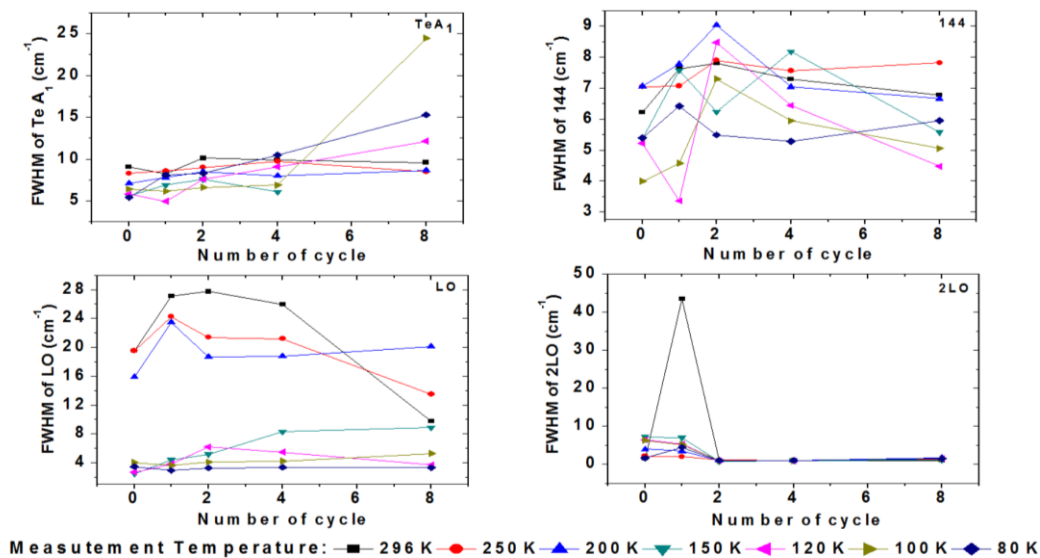

Figure 74. Variation of FWHM value of Te A_1, 144 cm^{-1}, LO and 2LO phonon modes of cyclic annealed samples during 20 min. at 420ºC.

I_{TeA1}/I_{LO} ratio as a function of annealing cycle and Raman measurement temperature is illustrated in Figure 75. I_{TeA1}/I_{LO} decreased when Raman measurement temperature decreased.

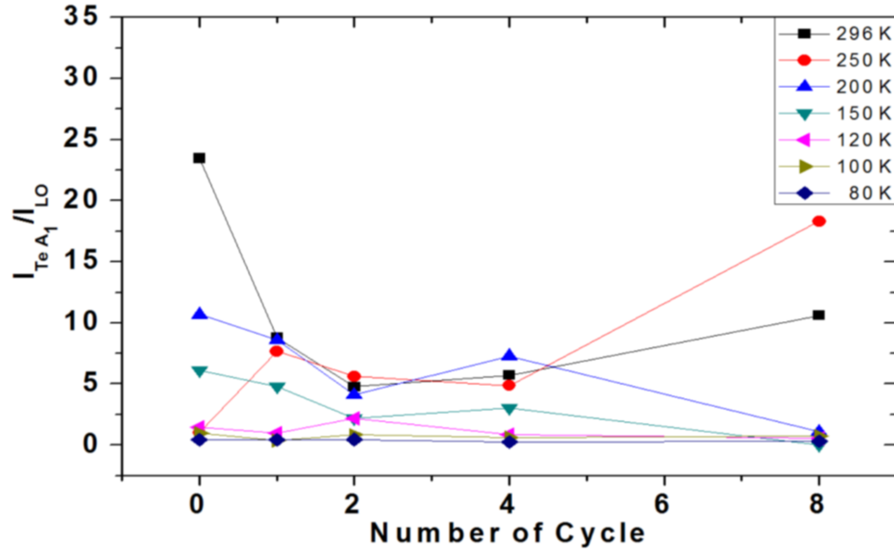

Figure 75. Plot of optic phonon mode's $I_{Te\ A1}/I_{LO}$ ratios as a function of annealing cycle of annealed at 420ºC during 20 min.

I_{144}/I_{LO} ratio as function of annealing cycle and Raman measurement temperature is illustrated in Figure 76. I_{144}/I_{LO} decreased when Raman measurement temperature decreased. I_{144}/I_{LO} ratios were similar with I_{TeA1}/I_{LO}, this result again increased 144 peak could be Te E mode.

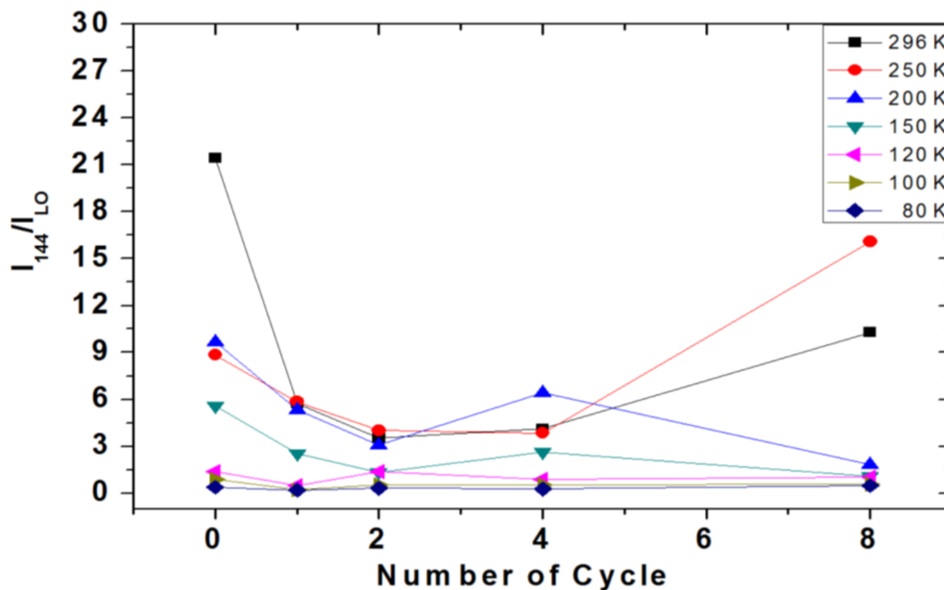

Figure 76. Graph of I_{144}/I_{LO} ratio as a function of annealing cycle. Raman measurement was done with cooling from 296 K to 80 K.

2LO/LO ratios did not display any relation with cycle number or Raman measurement temperature. 2LO/LO ratios increased up to 117 for 4 cycle annealed at 200 K (Figure 77).

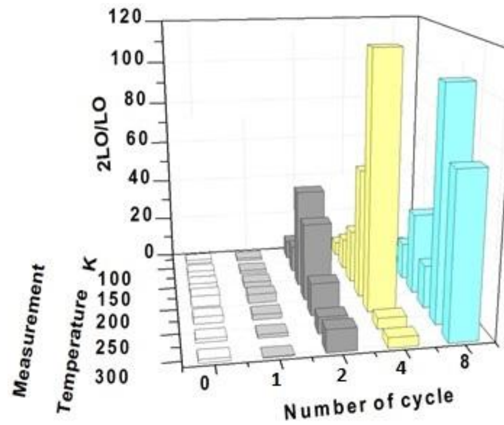

Figure 77. 3D graph of CdTe Raman spectroscopy result's 2LO/LO ratios changing with annealing cycle and Raman measurement temperature.

PL measurements were carried out to investigate Cycle annealed samples at 80 K. Resolution was not good enough to identify peaks. Peak positions was given on the graph in Figure 78 as correct as possible. Near-band-edge states were observed between 1.62-1.55, defect states was observed between 1.52-1.30 [37]. After cycle annealing, defect lines increased. When cycle number increased, defect induced luminescence decreased. Two cycle annealed sample's defect peaks between 1.445 and 1.300 were more intense. Increasing of defects line with annealing showed that the annealing system vacuum conditions was not enough to avoid from contaminations.

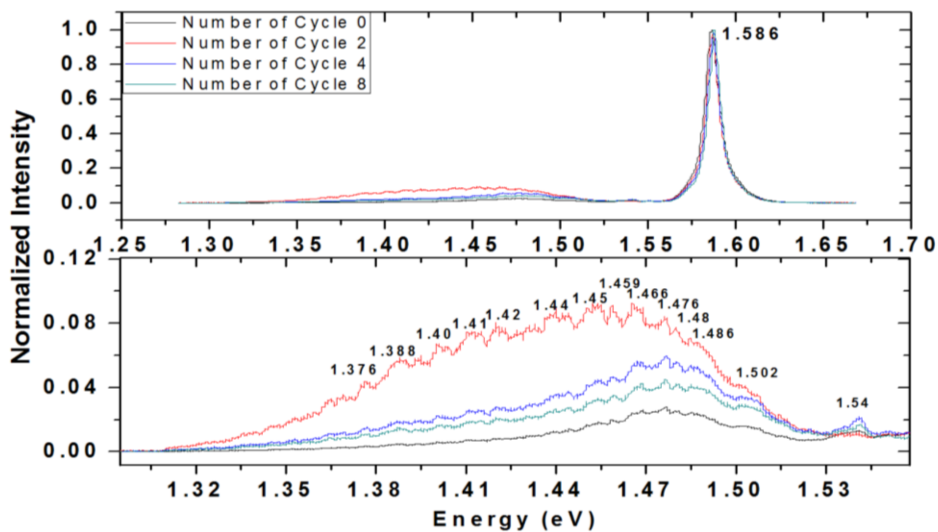

Figure 78. Photoluminescence spectra of cycle annealed samples at 80 K. Total anneal time was 20 min. Laser source was 488 nm.

Next, total annealing time was kept 10 min. for 420ºC and for this parameters 1, 2 and 4 cycle annealing was tried. There was no change with surface morphology, this was seen in Figure 79. AFM images was given in Figure 80 and surface roughness as a function of cycle number in Figure 81. The roughness dropped off with annealing. Dislocation densities decreased when the cycle number increased. However EPD value increased, when cycle was 4. That was shown as a graph in Figure 83 and SEM images was given in Figure 82 which was the EPD values calculated from those.

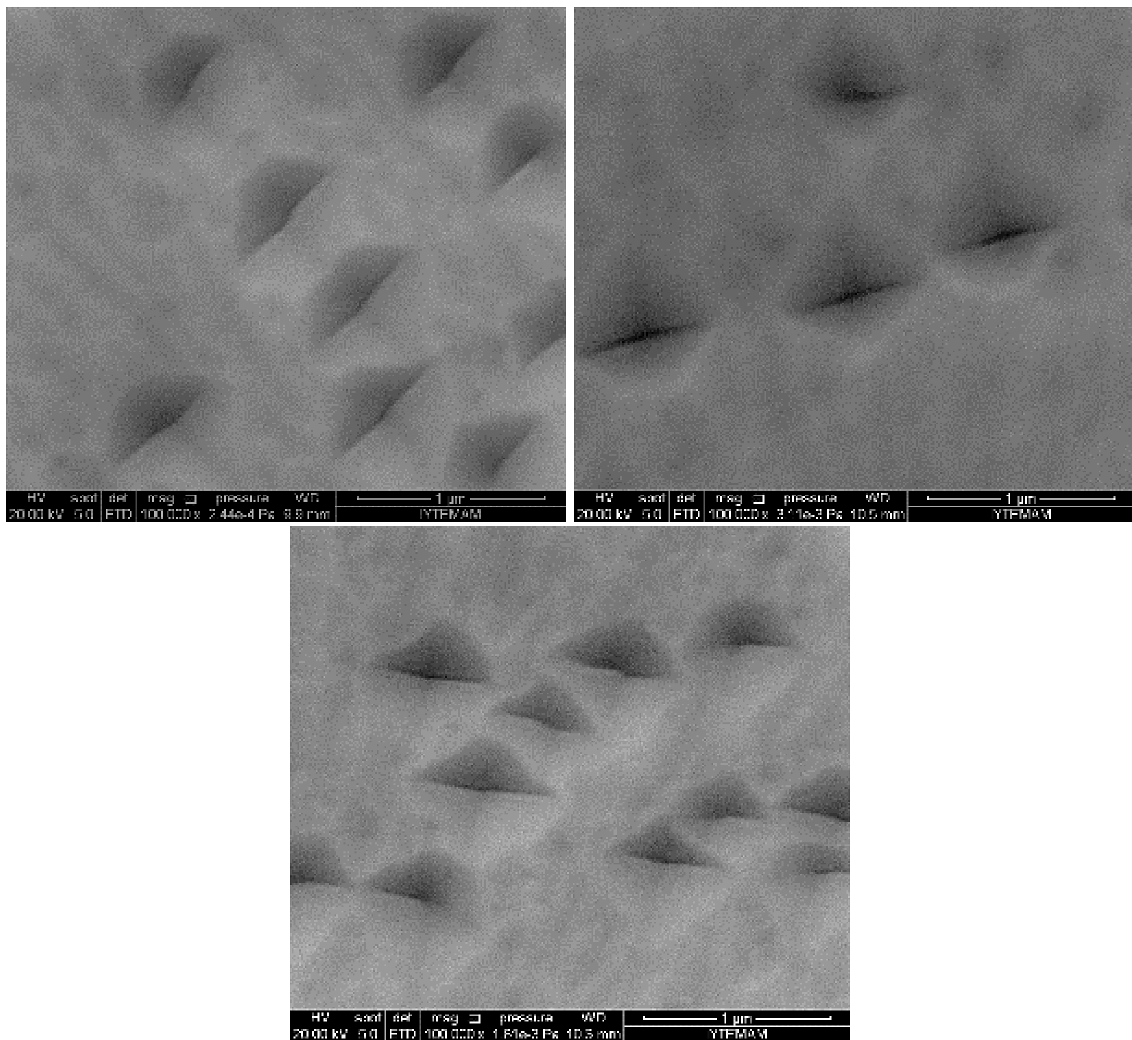

Figure 79. SEM micrograph of cyclic annealed samples at 420ºC with keeping total annealing time 10 min. a) CT9-2-AN32 for 1 cycle, b) CT9-2-AN33 for 2 cycle, and c) CT9-2-AN34 for 4 cycle.

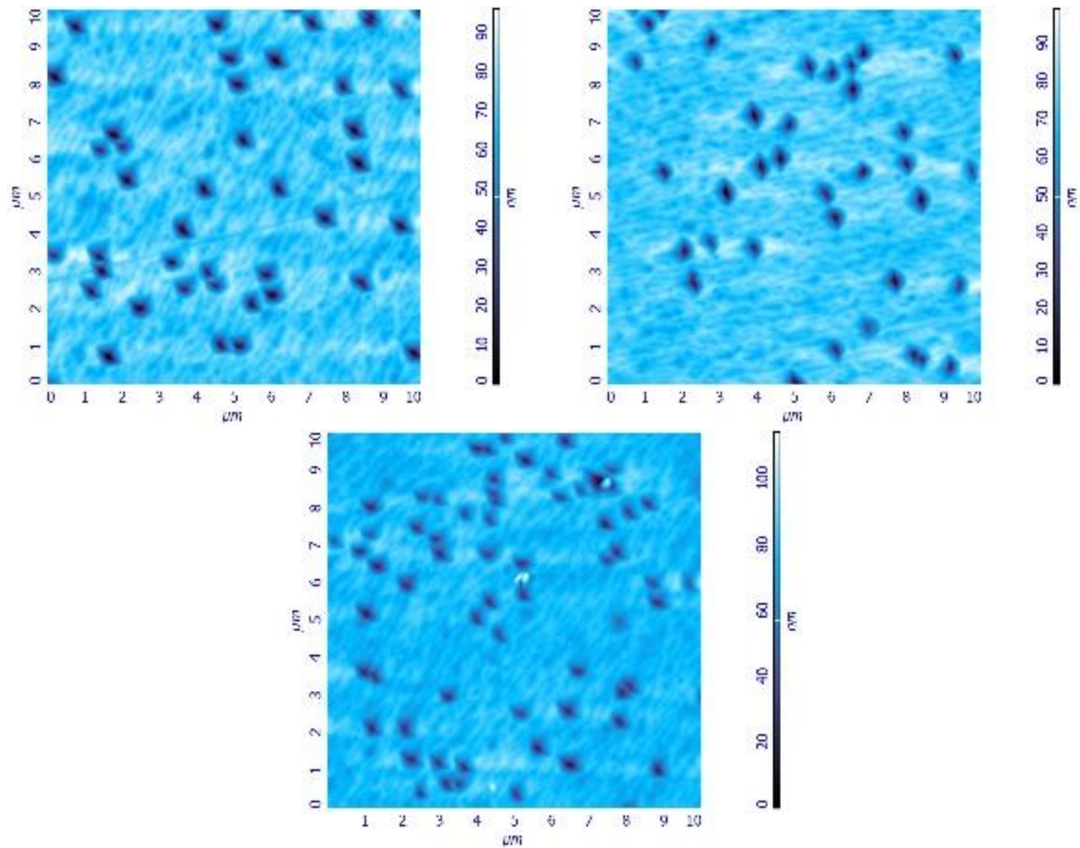

Figure 80. AFM images of cyclic annealed samples at 420ºC with keeping total anneal time 10 min. from 10x10 um^2 area a) CT9-2-AN32 for 1 cycle, b) CT9-2-AN33 for 2 cycle and c) CT9-2-AN34 for 4 cycle.

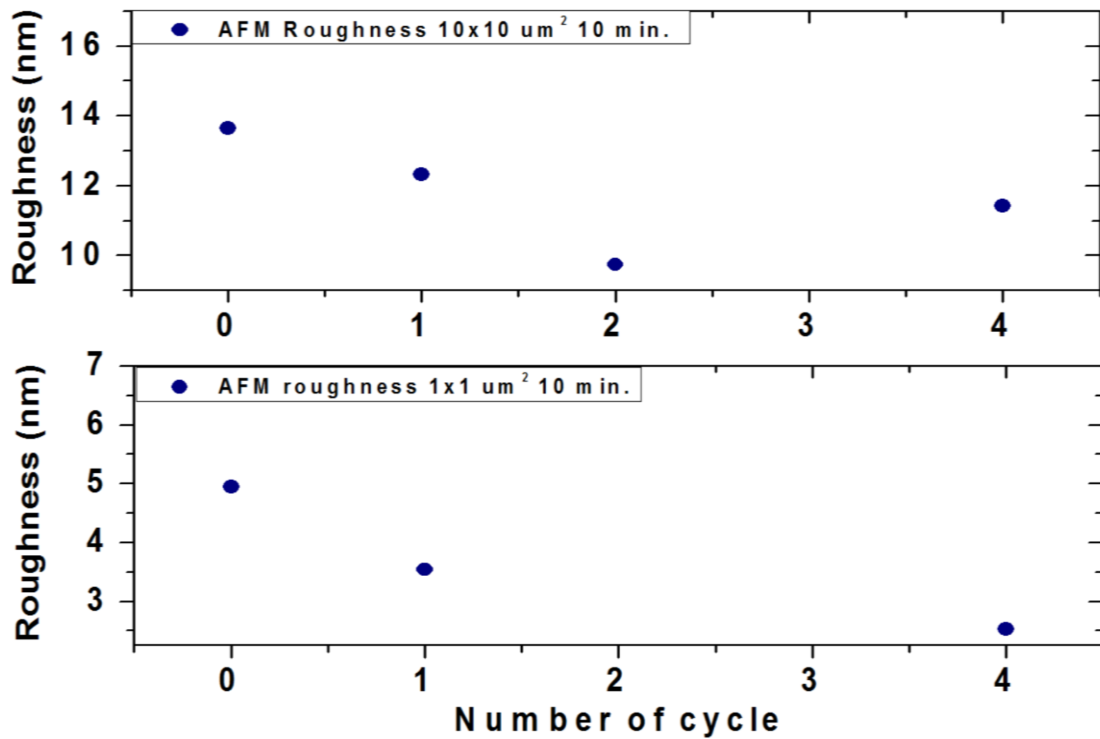

Figure 81. Surface roughness of annealed samples at 420ºC as a function of annealing number of cycle from 10x10 um^2 area.

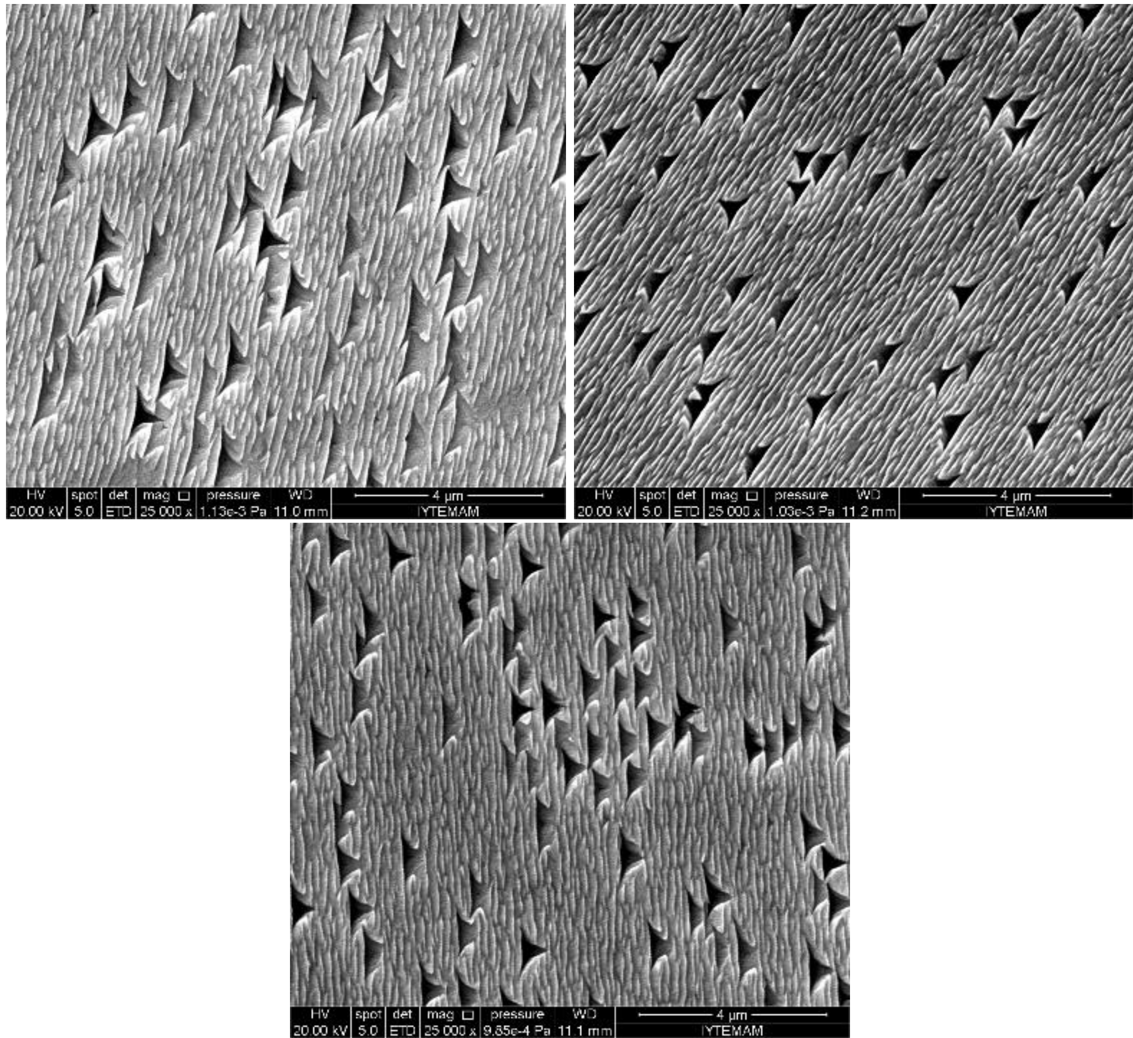

Figure 82. Etched by Everson method for cyclic annealed samples with keeping total time 10 min. a) CT9-2-AN32-E for cycle, b) CT9-2-AN33-E for 2 cycle, and d) CT9-2-AN34-E for 4 cycle.

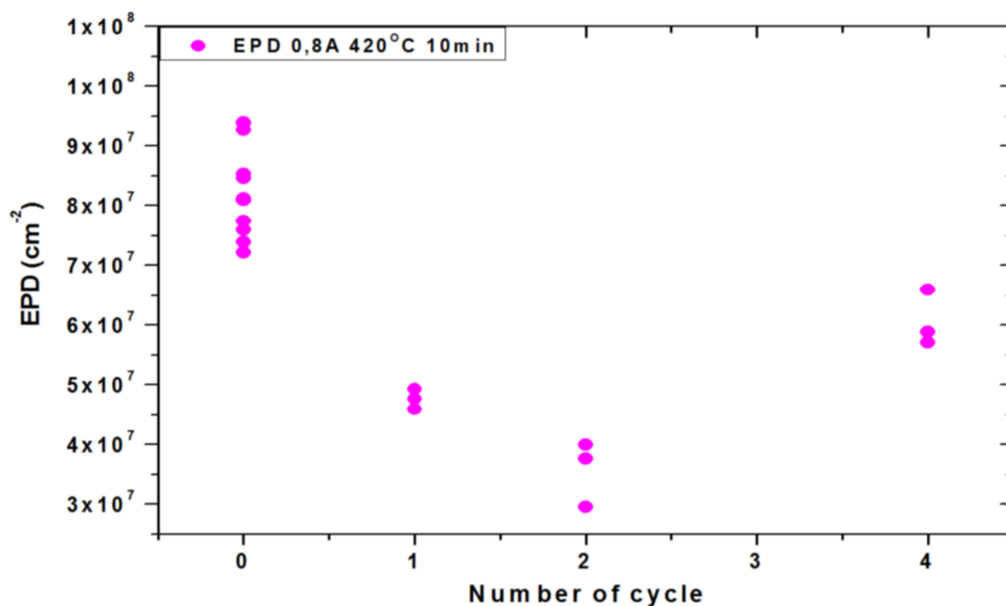

Figure 83. Dislocation densities as a function of annealing time. Annealing was at 420ºC.

Raman spectra is displayed in Figure 84, that total annealing time was 10 min. at 420°C and peak positions is illustrated in Figure 85. Te A_1 mode shifted nearly 4 cm^{-1} to higher wavenumber while decreasing Raman measurement temperature. 144 cm^{-1} peak shifted about 3 cm^{-1} to higher wavenumber while decreasing Raman measurement temperature. LO peak shifted about 6 cm^{-1}. 2LO peak position did not change while decreasing Raman measurement temperature.

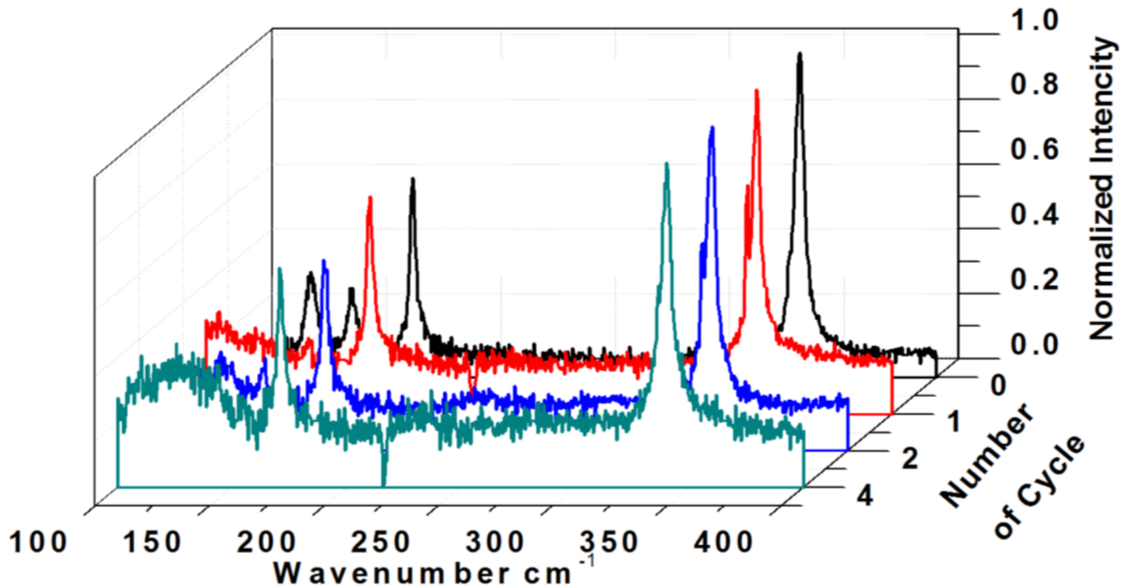

Figure 84. Raman shifts as a function of number of annealing cycle at 420°C. Total annealing time was 10 min. Raman measurement were done at 80 K.

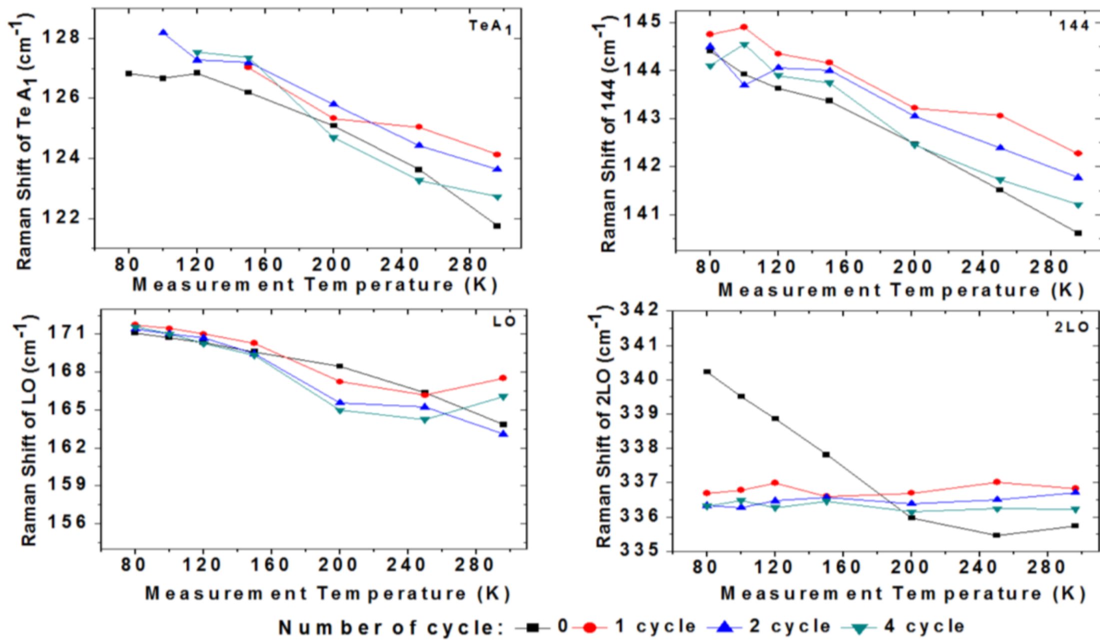

Figure 85. Raman shifts of Te A_1, 144 cm^{-1}, LO and 2LO phonon modes as a function of measurement temperature of cyclic annealed samples at 420 °C for 10 min total annealing time.

FWHM of Te A_1 mode variated from 5 cm^{-1} to 12 cm^{-1}. 144 peak's FWHM variated from 2 cm^{-1} to 9 cm^{-1}. FWHM of LO peak decreased when Raman measurement temperature decreased. FWHM value of 2LO peak decreased after annealing. FWHM value as a function of cycle is displayed in Figure 86.

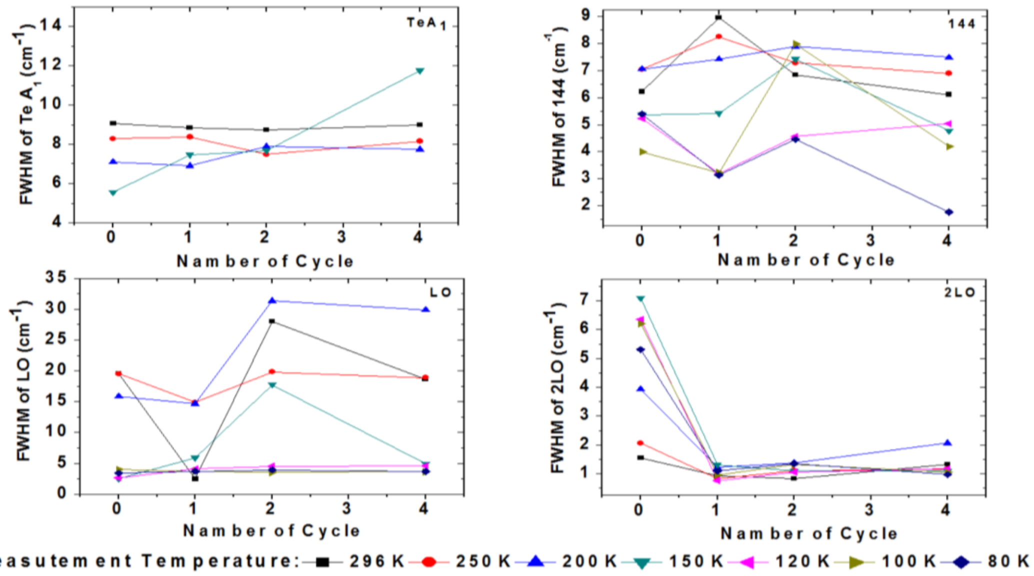

Figure 86. Variation of FWHM value of Te A_1, 144 cm^{-1}, LO and 2LO phonon modes of cyclic annealed samples for 10 min. at 420°C.

I_{TeA1}/I_{LO} ratio decreased after annealing. I_{TeA1}/I_{LO} again decreased when Raman measurement temperature decreased. I_{TeA1}/I_{LO} ratio is displayed in Figure 87 for cycle annealed samples at 420°C.

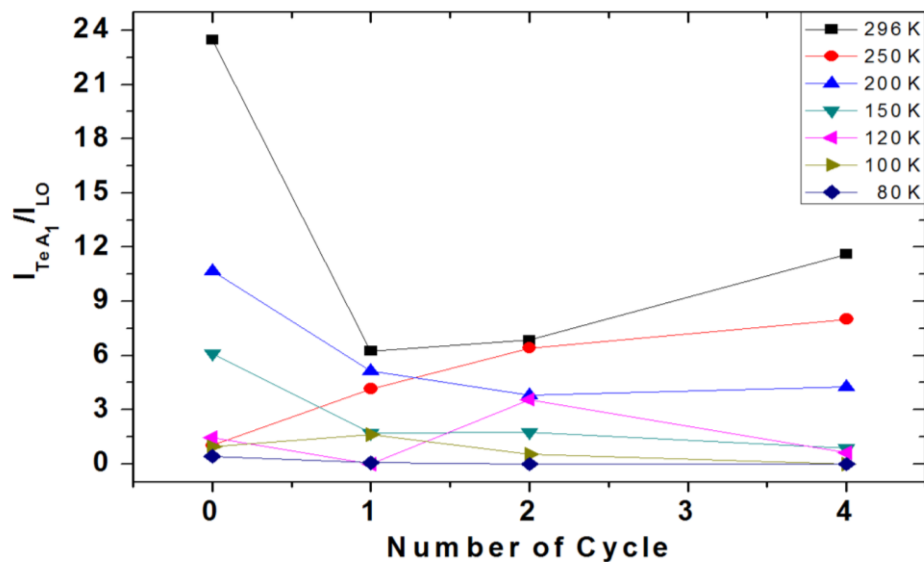

Figure 87. Plot of optic phonon mode's $I_{Te\ A1}/I_{LO}$ ratios as a function of annealing cycle of annealed at 420°C during 10 min.

I_{144}/I_{LO} ratio decreased after annealing. Additionally I_{144}/I_{LO} decreased when Raman measurement temperature decreased. I_{TeA1}/I_{LO} ratio is displayed in Figure 88 for cycle annealed samples at 420ºC (total annealing time was 10min).

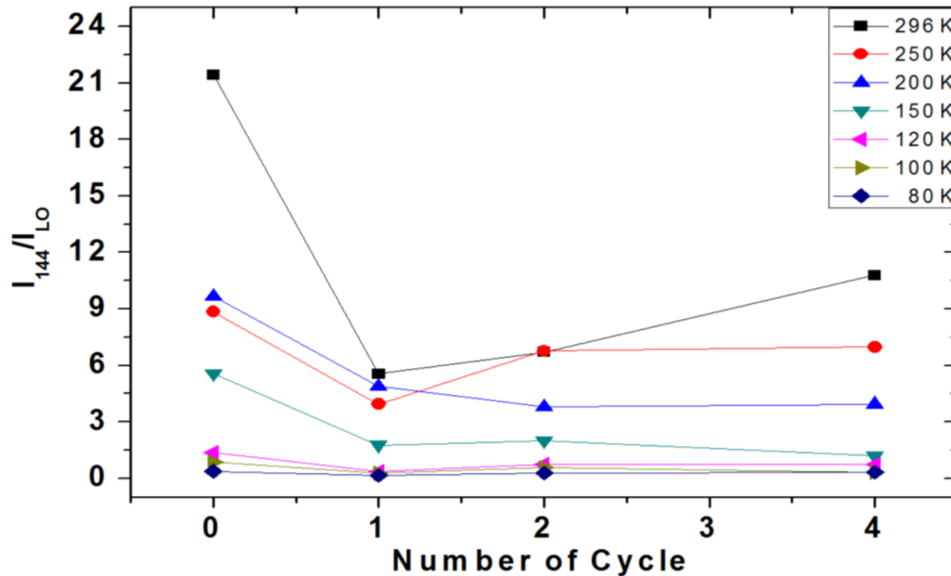

Figure 88 . Graph of I_{144}/I_{LO} ratio as a function of annealing cycle. Raman measurement was done with cooling from 296 K to 80 K.

2LO/LO ratio decreased while increasing cycle number. 2LO/LO also decreased while decreasing Raman measurement temperature. 2LO/LO ratios is displayed in Figure 89.

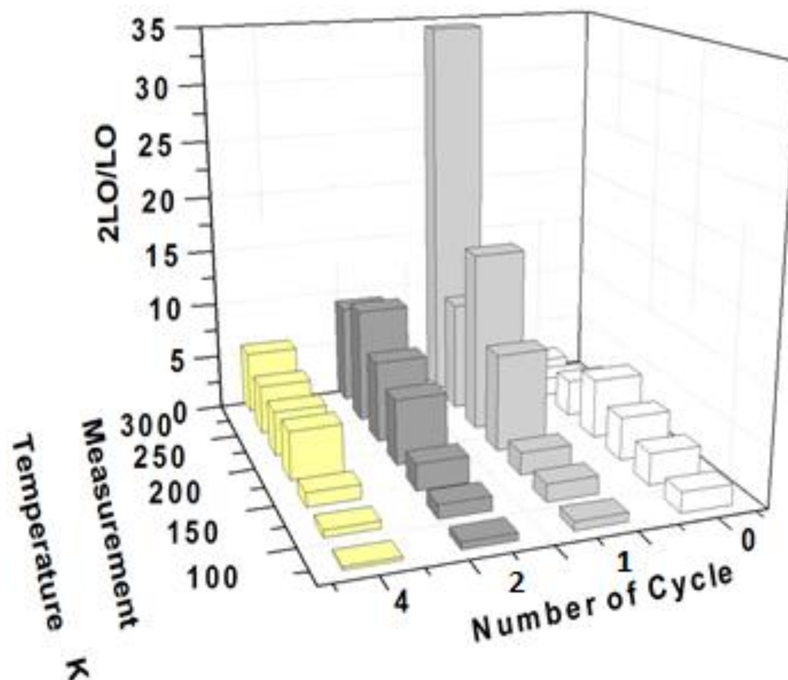

Figure 89. 3D graph of CdTe Raman spectroscopy result's 2LO/LO ratios changing with annealing cycle and Raman measurement temperature.

PL spectra of 10 min. cycle annealed samples is illustrated in Figure 90. The graph at the bottom of Figure 90 displays defect related peaks. Due to lack of vacuum conditions, intensities of defect related lines increased after annealing. Intensity of defects related peaks decreased when cycle number increased from 2 cycle to 4 cycle. Additionally one cycle annealed sample's defect peaks from 1.46 to 1.52 was less intense than four cycle annealed samples but one cycle annealed sample's defect peaks from 1.30 to 1.46 was more intense than four cycle annealed samples.

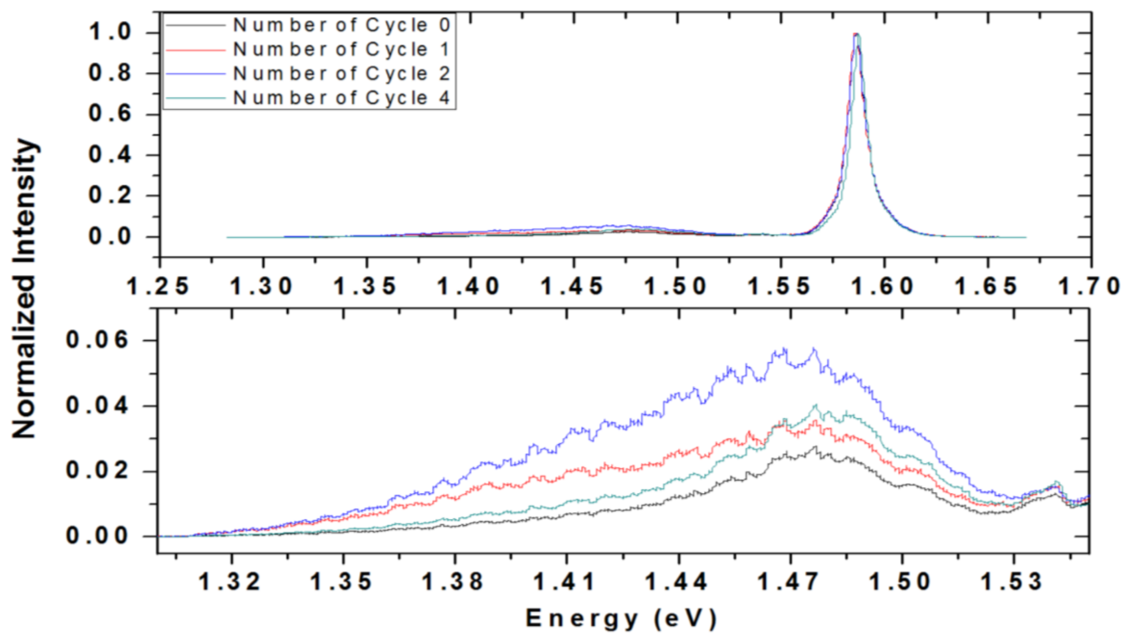

Figure 90. Photoluminescence spectra of cycle annealed samples at 80 K. Total annealing time was 10 min. Laser source was 488 nm.

3.2. Annealing Under Hydrogen Atmosphere

In this section, samples were annealed inside an hydrogen gas environment under 20-10 mTorr vacuum. Hydrogen pressure was fixed at 700 sccm, temperature was fixed at 300°C and time was changed from 6 hours to 48 hours. Surface morphology micrographs were given in Figure 91 for SEM and AFM in Figure 92. Also AFM roughness graph were given in Figure 93 and graph shows that 6 hours and 12 hours annealing gave to the surface decrement of roughness but 48 hours annealing gave the increment to surface roughness. Dislocation density changing with time was given in Figure 94 and Figure 95. After 12 hours annealing, dislocation density increased, however, after 48 hours annealing, dislocation density decreased.

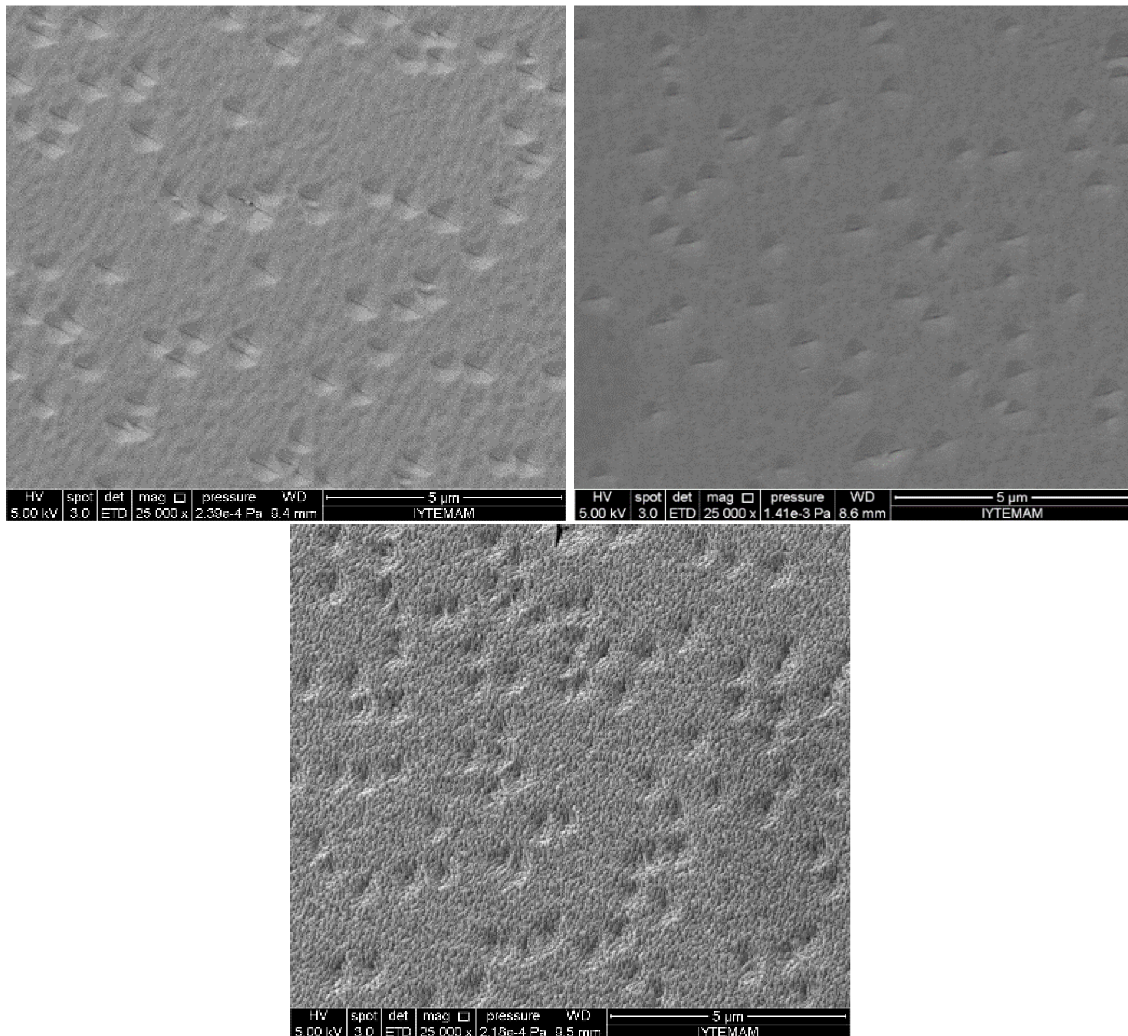

Figure 91. SEM micrograph of annealed samples at 300°C under 700 sccm H_2 atmosphere a) CT9-2-AN14 for 6 hours, b) CT9-2-AN13 for 12 hours and c) CT9-2-AN15 for 48 hours.

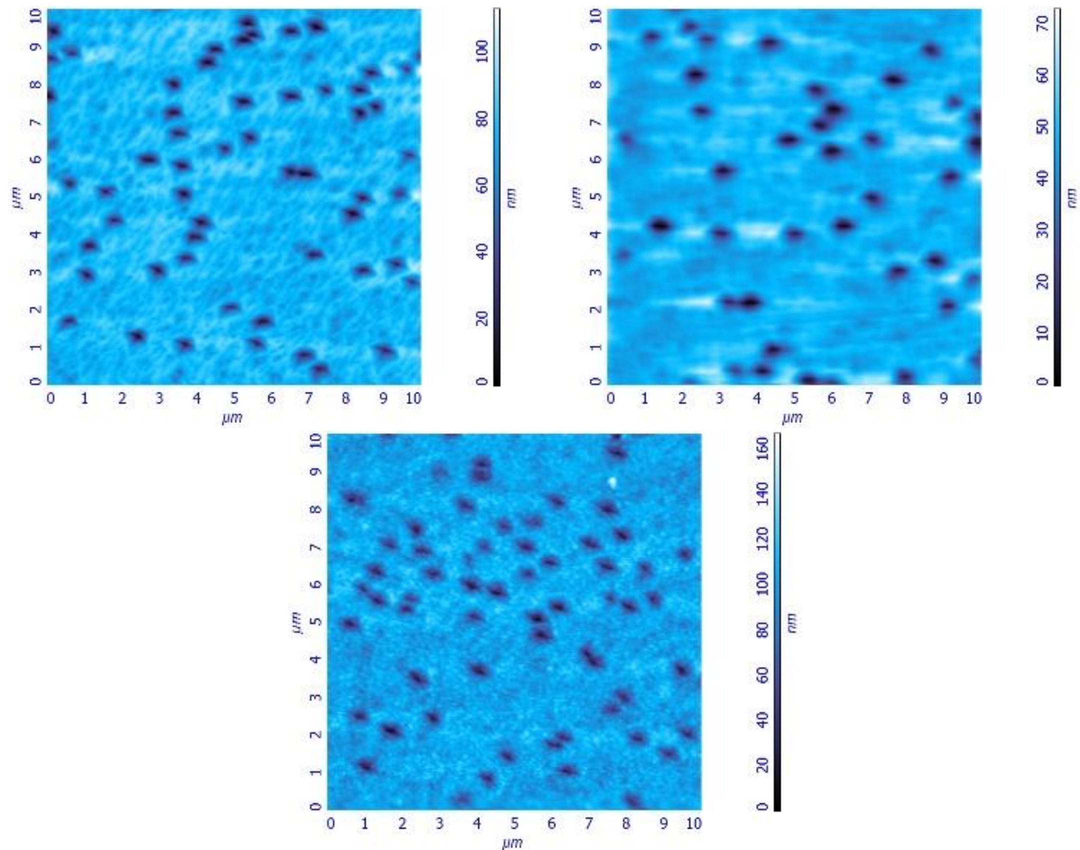

Figure 92. AFM 2D image of annealed samples at 300°C under 700 sccm H_2 atmosphere from 10x10 um^2 area a) CT9-2-AN14 for 6 hours, b) CT9-2-AN13 for 12 hours and c) CT9-2-AN15 for 48 hours.

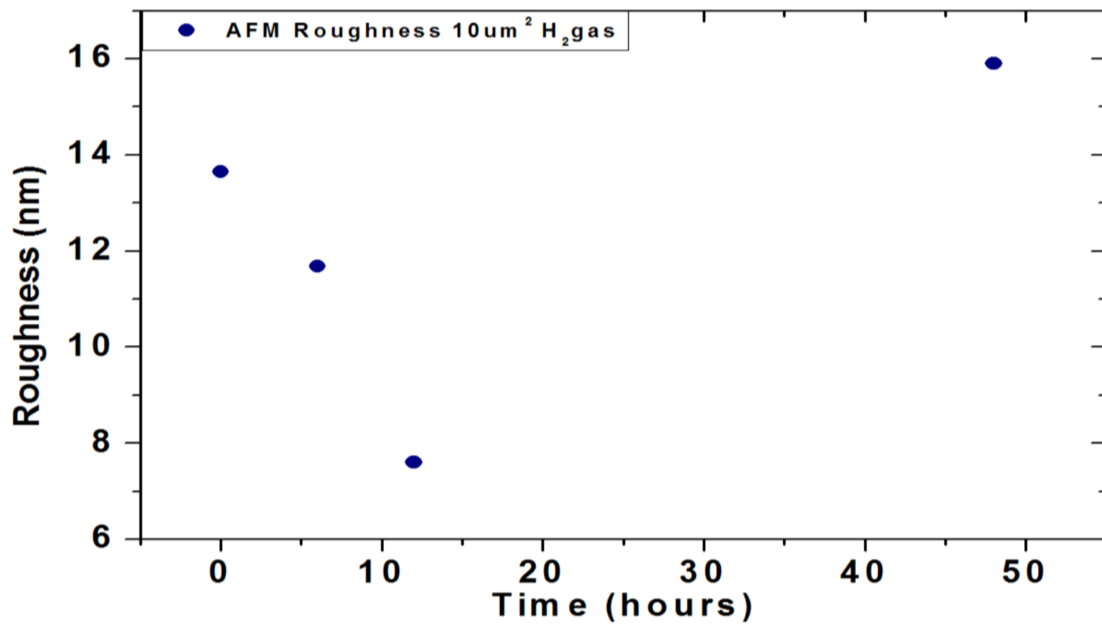

Figure 93. Surface roughness of annealed at 300 °C as a function of annealing temperature from 10x10 um^2 area.

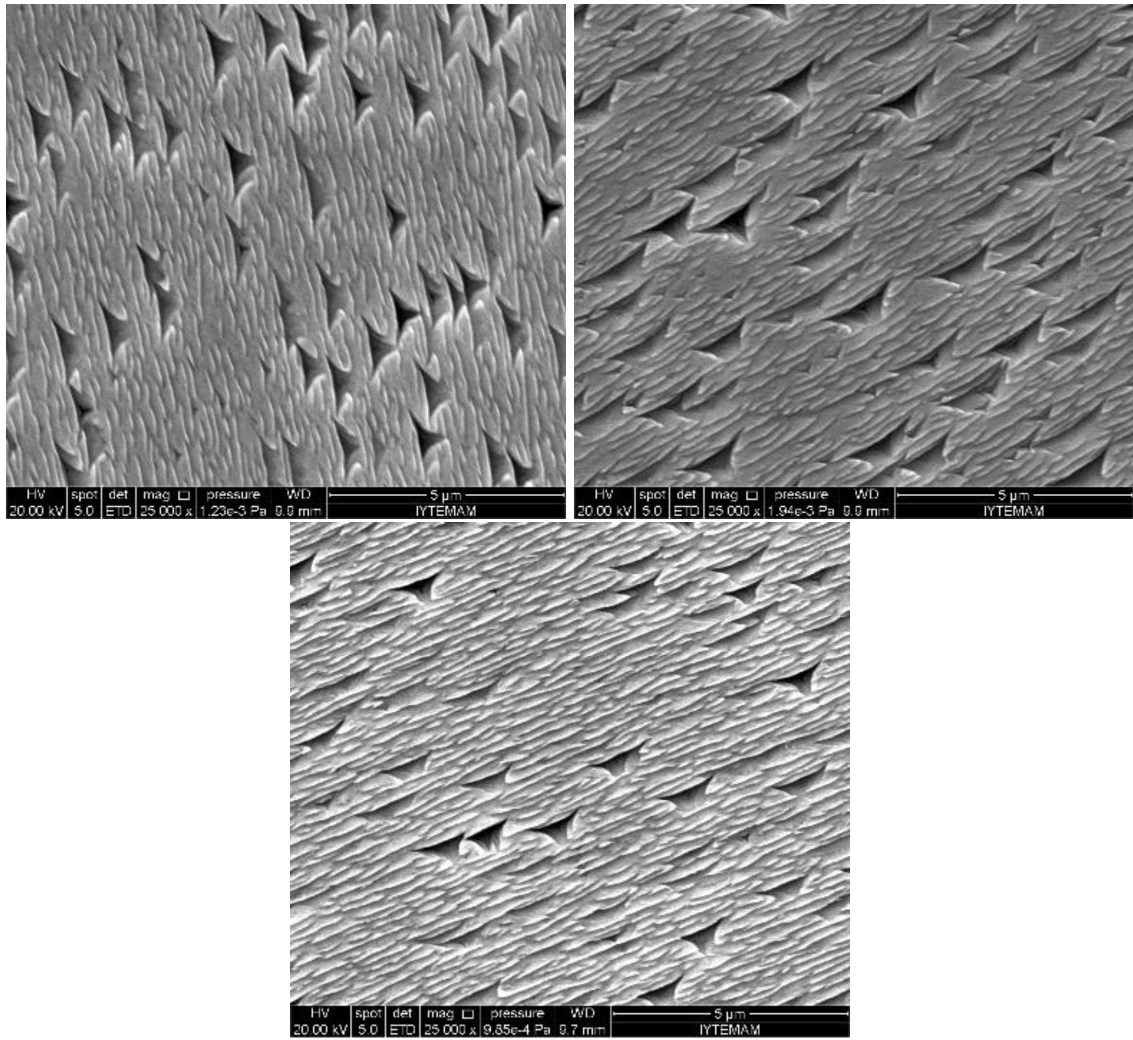

Figure 94. SEM micrograph of Etched samples a) CT9-2-AN14-E, b) CT9-2-AN13-E and c) CT9-2-AN15-E.

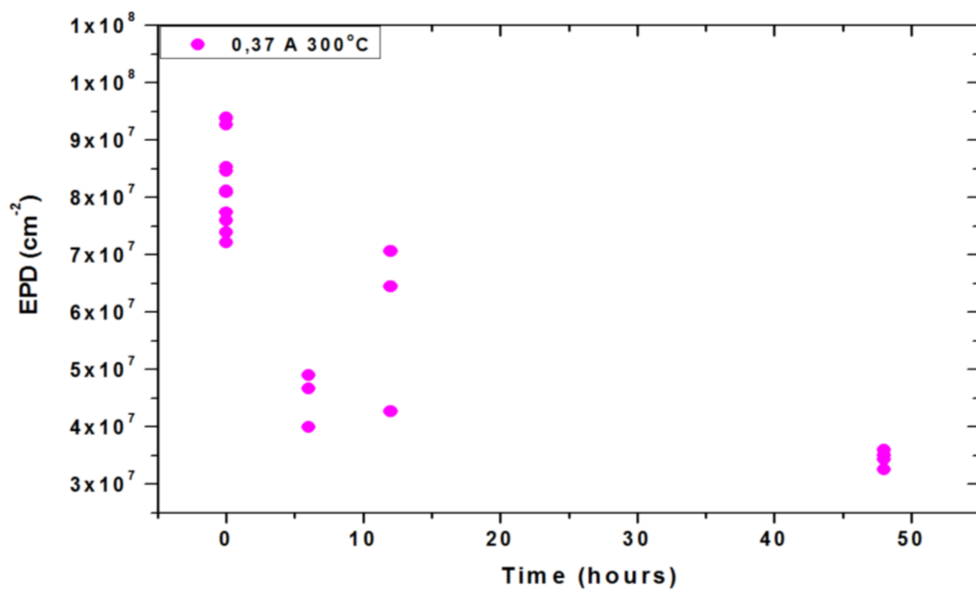

Figure 95. Dislocation densities as a function of annealing time. Annealing was at 300ºC under 700 sccm H_2 atmosphere.

Raman spectra of annealed samples for 6, 12, and 48 hour annealing durations under hydrogen atmosphere, is displayed in Figure 96. Annealed sample during 6 hours has more intense peaks at 72 cm^{-1} and 90 cm^{-1}. The peak positons are presented in Figure 97. Te A_1 mode was shifted by 5 cm^{-1}, 144 peak was shifted by 3 cm^{-1}, and LO mode was shifted by 8 cm^{-1}. 2LO peak of 6 and 12 hours annealed samples shifted from 331 cm^{-1} to 340 cm^{-1} linearly about 9 cm^{-1}. A relation (equation 4) is given for 2LO peak position as a function of temperature (see Figure 117 in appendix a).

$$peak\ position\ of\ 2LO = -0.039T + 342.78 \tag{3.1}$$

Where T is the temperature in kelvins. 2LO peak of as-grown and 48 hours annealed samples changed from 335 cm^{-1} to 340 cm^{-1} about 5 cm^{-1}.

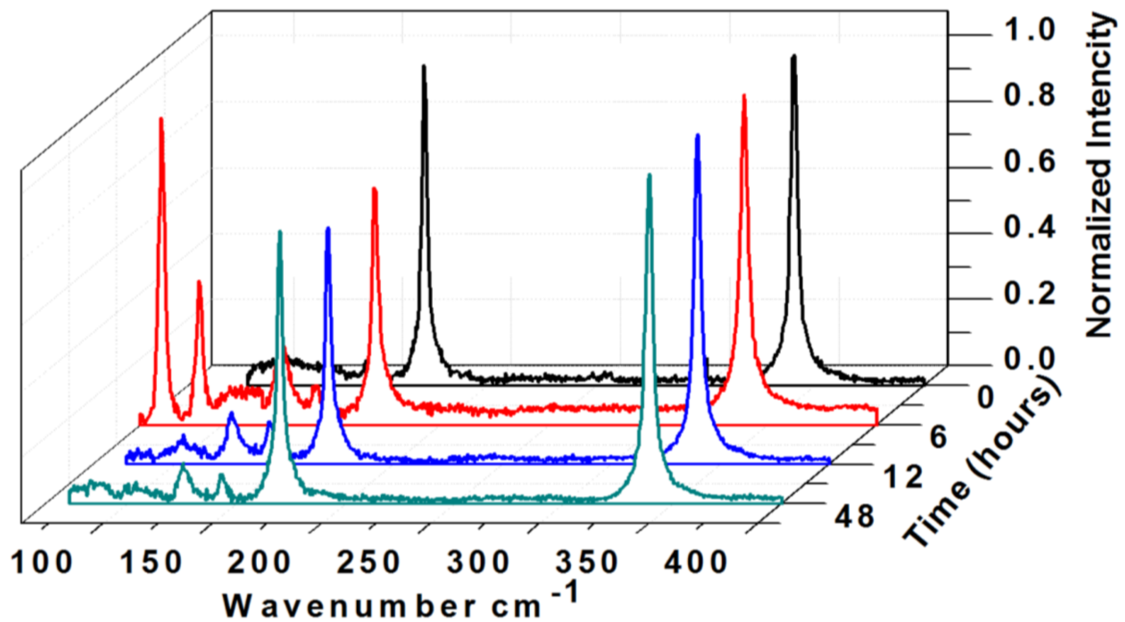

Figure 96. Raman shifts as a function of annealing time of annealed samples at 300°C with 700 sccm H_2 gas. Raman measurements were done at 80 K.

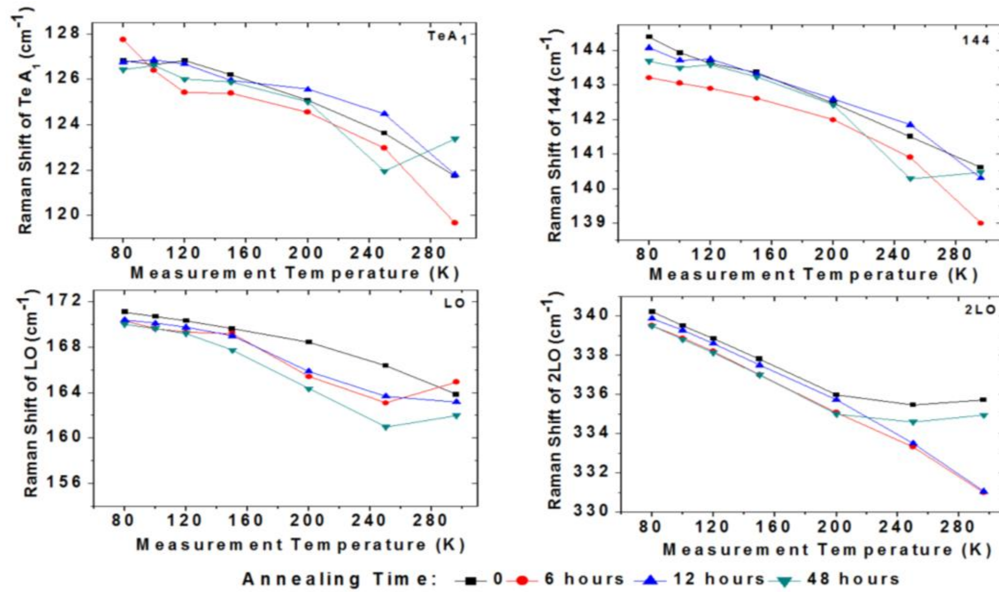

Figure 97. Raman shifts of Te A_1, 144 cm^{-1}, LO and 2LO phonon modes as a function of measurement temperature of annealed samples at 300 ºC under H_2 atmosphere.

FWHM of Raman modes is displayed in Figure 98. FWHM of Te A_1 mode decreased when annealing temperature was decreased and FWHM of Te A_1 increased for the 6 hours annealed samples. FWHM of 144 cm^{-1} peak varied between 2 cm^{-1} and 10 cm^{-1} and there was no relation between the Raman measurement temperature and annealing time. FWHM of LO decreased whit decreased sample temperature. FWHM of LO peak did not change with the annealing time at 80 K, 100 K and 120 K.

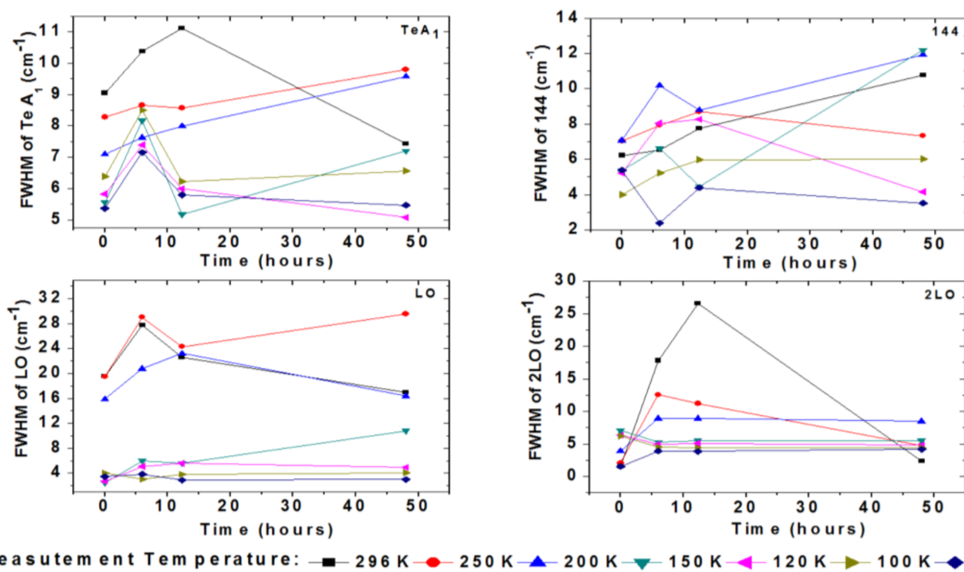

Figure 98. Variation of FWHM value of Te A_1, 144 cm^{-1}, LO and 2LO phonon modes of annealed samples at 300ºC under H_2 atmosphere.

I_{TeA1}/I_{LO} ratio decreased with sample temperature. I_{TeA1}/I_{LO} ratio decreased after the annealing and did not change with annealing time, it was constant at all annealing time (Figure 99).

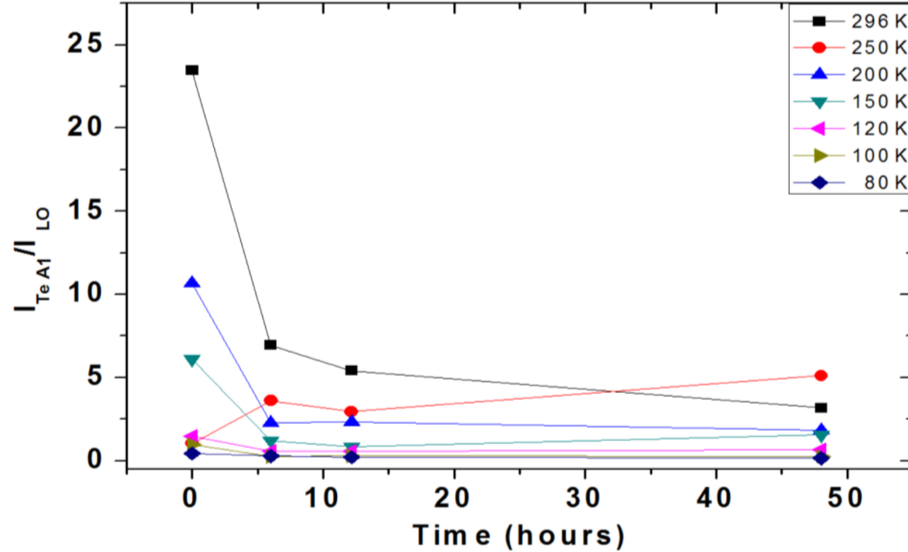

Figure 99. Plot of optic phonon mode's $I_{Te\ A1}/I_{LO}$ ratios as a function of annealing time of annealed at 300°C under H_2 atmosphere.

I_{144}/I_{LO} ratio decreased again with decreasing Raman measurement temperature. I_{144}/I_{LO} ratio was constant when annealing time increased. Similarities of I_{TeA1}/I_{LO} (Figure 100) and I_{144}/I_{LO} ratios verified that there was just Te E mode at 144 cm^{-2} and there was no CdTe TO mode for CT9 sample.

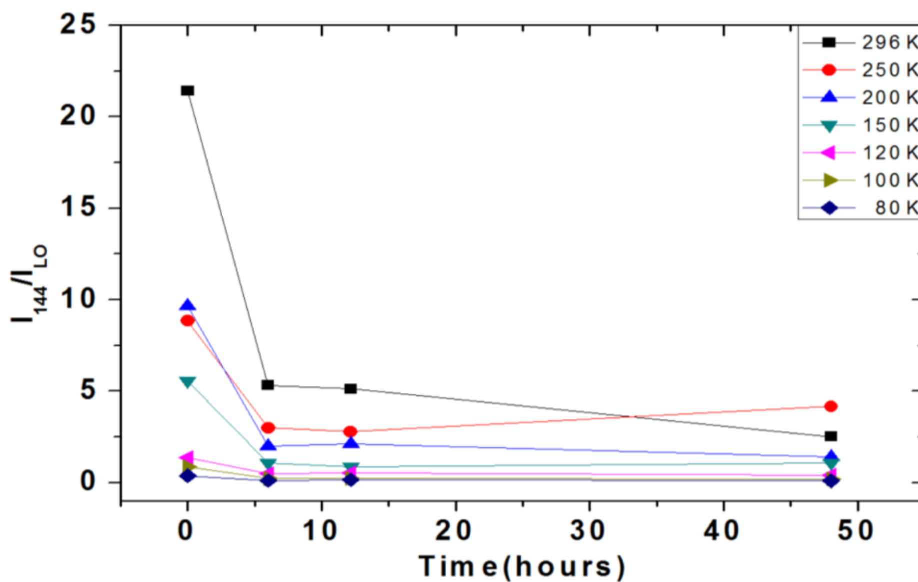

Figure 100. Graph of I_{144}/I_{LO} ratio as a function of annealing time. Raman measurement was done with cooling from 296 K to 80 K.

2LO/LO intensity ratios decreased again with decreasing temperature from 150 K to 80 K (Figure 101). 2LO/LO intensity ratios decreased also with increasing time from 1.77 (as-grown) to 1.27 (48 hours annealed). 1.27 was a near value to 0.93 which is the 2LO/LO ratios value for resonance scattering CdTe sample [27].

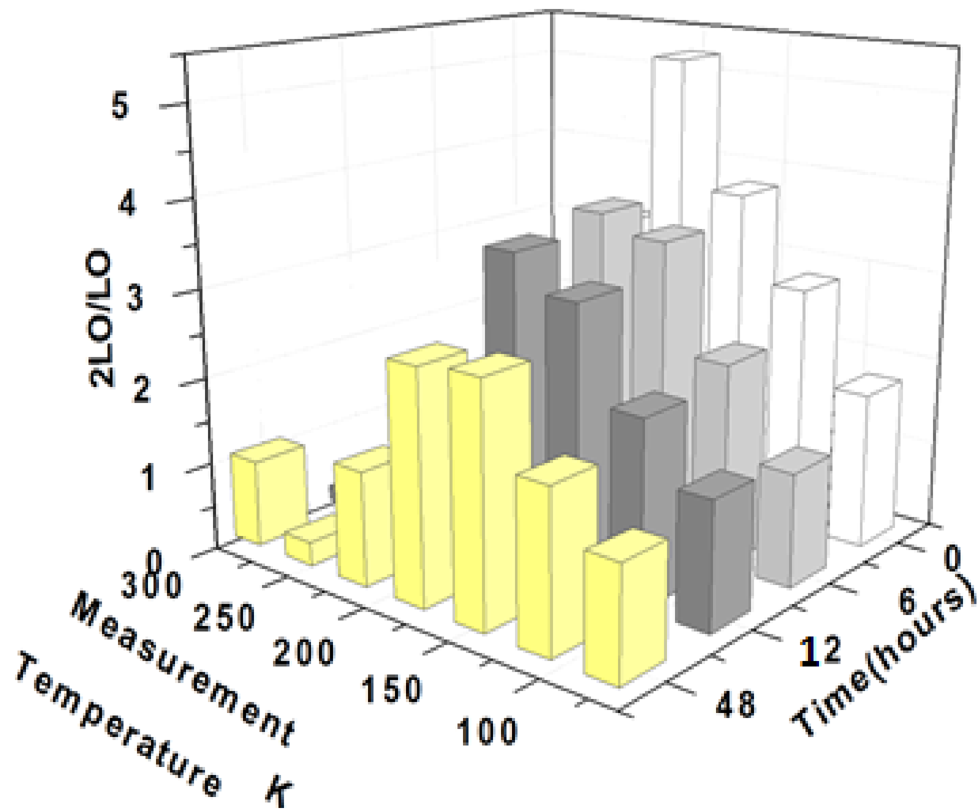

Figure 101. 3D graph of CdTe Raman spectroscopy result's 2LO/LO ratios changing with annealing time and Raman measurement temperature.

CHAPTER 4

CONCLUSIONS

As a conclusion, in this thesis work defects reduction processes in CdTe epilayers grown by MBE was studied. Annealing method is employed to reduce the number of defects. A homemade annealing apparatus was designed. It consists of a quartz tube, a resistive silicon heater and H_2 gas flow controller. The heater and gas flowmeters were calibrated before annealings.

An MBE grown CdTe film was cut into small pieces. Then the pieces were annealed in the homemade apparatus. As parameters, annealing temperature, annealing time, annealing cycle and hydrogen flow were used. The effect of these parameters were analyzed by SEM, AFM, defect decoration etching, and Resonance Raman Scattering and PL measurements.

The surface roughness decreased with increasing cycle number. This shows that cyclic annealing can reduce the surface roughness.

The dislocation density for 5 min. annealed samples were decreased with increasing temperature, 20 min. anneals degrade sample crystal quality, since in general dislocation density decreased with increasing annealing time but dislocation density increased for 20 min. anneals when annealing temperature increased.

2LO/LO ratios decreased when temperature was increased during 5 min. annealing and when annealing time was increased for 300 ^oC and 400 ^oC annealing. In this way, 2LO/LO ratios can be reduce with increasing annealing temperature and annealing time.

Intensity ratios of 144/LO and Te A_1/CdTe LO was similar for all samples. This indicated that 144 corresponded the Te E mode. Additionally CdTe TO phonon mode was not observed for CdTe (211) by incoming resonance scattering.

Peak positions and FWHM values of Te A_1, 144, LO did not yield conclusive results after the annealings. This might be related to sample homogeneity. 2LO peak position as a function of temperature was defined.

According to the PL spectra of our samples there was no reduction defect levels. It was concluded that this was due to the insufficient vacuum conditions during the annealing processes.

This results indicate that improvements can be observed if the annealings are carried out with more homogenous sample.

REFEREENCES

[1] M.A. Kinch, The Future of Infrared; III–Vs or HgCdTe?, Journal of Electronic Materials, 44 (2015) 2969-2976.

[2] A. Rogalski, HgCdTe infrared detector material: history, status and outlook, Reports on Progress in Physics, 68 (2005) 2267-2336.

[3] P.S. Wijewarnasuriya, M. Zandian, D.D. Edwall, W.V. Mclevige, C.A. Chen, J.G. Pasko, G. Hildebrandt, A.C. Chen, J.M. Arias, A.I. Dsouza, S. Rujirawat, S. Sivananthan, MBE P-on-n $Hg_{1-x}Cd_xTe$ Heterostructure Detectors on Silicon Substrates, Journal of Electronic Materials, 27 (1998).

[4] M. Carmody, A. Yulius, D. Edwall, D. Lee, E. Piquette, R. Jacobs, D. Benson, A. Stoltz, J. Markunas, A. Almeida, J. Arias, Recent Progress in MBE Growth of CdTe and HgCdTe on (211)B GaAs Substrates, Journal of Electronic Materials, 41 (2012) 2719-2724.

[5] S.M. Johnson, Effect of dislocations on the electrical and optical properties of long-wavelength infrared HgCdTe photovoltaic detectors, Journal of Vacuum Science & Technology B: Microelectronics and Nanometer Structures, 10 (1992) 1499.

[6] J.D. Benson, S. Farrell, G. Brill, Y. Chen, P.S. Wijewarnasuriya, L.O. Bubulac, P.J. Smith, R.N. Jacobs, J.K. Markunas, M. Jaime-Vasquez, L.A. Almeida, A. Stoltz, U. Lee, M.F. Vilela, J. Peterson, S.M. Johnson, D.D. Lofgreen, D. Rhiger, E.A. Patten, P.M. Goetz, Dislocation Analysis in (112)B HgCdTe/CdTe/Si, Journal of Electronic Materials, 40 (2011) 1847-1853.

[7] S. Farrell, M.V. Rao, G. Brill, Y. Chen, P. Wijewarnasuriya, N. Dhar, D. Benson, K. Harris, Effect of Cycle Annealing Parameters on Dislocation Density Reduction for HgCdTe on Si, Journal of Electronic Materials, 40 (2011) 1727-1732.

[8] S. Simingalam, G. Brill, P. Wijewarnasuriya, M.V. Rao, Low Temperature, Rapid Thermal Cycle Annealing of HgCdTe Grown on CdTe/Si, Journal of Electronic Materials, 44 (2014) 1321-1326.

[9] M. Yamaguchi, M. Tachikawa, Y. Itoh, M. Sugo, S. Kondo, Thermal annealing effects of defect reduction in GaAs on Si substrates, Journal of Applied Physics, 68 (1990) 4518.

[10] Y. Chen, S. Farrell, G. Brill, P. Wijewarnasuriya, N. Dhar, Dislocation reduction in CdTe/Si by molecular beam epitaxy through in-situ annealing, Journal of Crystal Growth, 310 (2008) 5303-5307.

[11] G. Brill, S. Farrell, Y.P. Chen, P.S. Wijewarnasuriya, M.V. Rao, J.D. Benson, N. Dhar, Dislocation Reduction of HgCdTe/Si Through Ex Situ Annealing, Journal of Electronic Materials, 39 (2010) 967-973.

[12] T. Aoyama, K.i. Goto, T. Yamazaki, T. Ito, Silicon (001) surface after annealing in hydrogen ambient, j. vac. sci. technol. a, (1996).

[13] D. Ballutaud , C. Debiemme-Chouvy, A. Etcheberry , p. de Mierry , L. Svob, Reactivity of III-V and II-VI semiconductors toward hydrogen: surface modification and evolution in air Applied Surface Science (1995).

[14] J.H.B. M.S. Han , Y.T. Oh , T.W. Kang , T.W. Kim , Jung In Choi The behavior of the surface charge density in Hg $d, _,Te epilayers due to hydrogenation and annealing Applied Surface Science (1996).

[15] T.W.K. M.D. Kim , T.W. Kim Hydrogenation and annealing effects on the deep levels and acceptor neutralization in p-CdTe, Applied Surface Science (1999).

[16] A. Smekal, Zur Quantentheorie der Dispersion, Naturwissenschaften, 11 (1923) 873-875.

[17] C.V. RAMAN, Ind. J. Phys., (1928) 387.

[18] L.M. G. LANDSBERG, Naturwiss., (1928).

[19] G. Abstreiter, E. Bauser, A. Fischer, K. Ploog, Raman Spectroscopy- A Versatile Tool for Characterization of Thin Films and Heterostructures of GaAs and $Al_xGa_{1-x}As$, Appl. Phys., (1978) 345-352.

[20] S. PERKOWITZ, Optical Characterization of Semiconductors: Infrared, Raman, and Photoluminescence Spectroscop, ACADEMIC PRESS, (1993).

[21] S.H. Shin, J. Bajaj, L.A. Moudy, D.T. Cheung, Characterization of Te Precipitates in Cdte Crystals, Applied Physics Letters, 43 (1983) 68-70.

[22] G. Lucovsky, R.C. Keezer, Infra-red lattice bands of trigonal tellurium and selenium, Solid State Communications, 5 (1967) 439-445.

[23] W. Richter, J.B. Renucci, M. Cardona, Hydrostatic Pressure Dependence of First-Order Raman Frequencies in Se and Te, physica status solidi (b)56 (1973) 223-229.

[24] P.M. Amirtharaj, F.H. Pollak, Raman scattering study of the properties and removal of excess Te on CdTe surfaces, Applied Physics Letters, (1984) 789.

[25] K.J. Mackey, D.R.T. Zahn, P.M.G. Allen, R.H. Williams, W. Richter, R.S. Williams, InSb-CdTe interfaces: A combined study by soft xmray photoemission, low-energy electron diffraction, and Raman spectroscopy, Journal of Vacuum Science & Technology B, (1987) 1233.

[26] A. Lusson, J. Wagner, M. Ramsteiner, Resonant Raman scattering of In^{+} - implanted CdTe and $Cd_{O.23}$ $Hg_{0.77}$ Te, Applied Physics Letters, (1989) 1787.

[27] Z.C. Feng, S. Perkowitz, J.M. Wrobel, J.J. Dubowski, Outgoing multiphonon resonant Raman scattering and luminescence near the $E_0+\Delta_0$ gap in epitaxial CdTe Films, PHYSICAL REVIEW B, 39 (1989).

[28] N.V. Sochinskii, M.D. Serrano, E. Dieguez, F. Agullorueda, U. Pal, J. Piqueras, P. Fernandez, Effect of Thermal Annealing on Te Precipitates in Cdte Wafers Studied by Raman-Scattering and Cathodoluminescence, Journal of Applied Physics, 77 (1995) 2806-2808.

[29] D. Nam, H. Cheong, A.S. Opanasyuk, P.V. Koval, V.V. Kosyak, P.M. Fochuk, Raman investigation on thin and thick CdTe films obtained by close spaced vacuum sublimation technique, P hys. Status Solidi C, (2014) 1515-1518.

[30] www.k-space.com, in.

[31] www.axt.com, in.

[32] L. van Laake, A.J. Hart, A.H. Slocum, Suspended heated silicon platform for rapid thermal control of surface reactions with application to carbon nanotube synthesis, The Review of scientific instruments, 78 (2007) 083901.

[33] Germer T A, Haegel N M and Haller E E 1986 J. Appl. Phys. 60 1055.

[34] A.S. Pine, G. Dresselhaus, Raman Spectra and Lattice Dynamics of Tellurium, PHYSICAL REVIEW B, 4 (1971) 356-371.

[35] G.A.N. Connell, R.J. Nemanich, C.C. Tsai, Interference enhanced Raman scattering from very thin absorbing films, Applied Physics Letters, (1980).

[36] E. Bilgilisoy, S. Özden, E. Bakali, M. Karakaya, Y. Selamet, Characterization of CdTe Growth on GaAs Using Different Etching Techniques, Journal of Electronic Materials, (2015).

[37] J. Olvera, O. Martínez, J.L. Plaza, E. Diéguez, Luminescence effects of ion-beam bombardment of CdTe surfaces, Journal of Luminescence, 129 (2009) 941-944.

APPENDIX A. MORE RAMAN SPECTRA

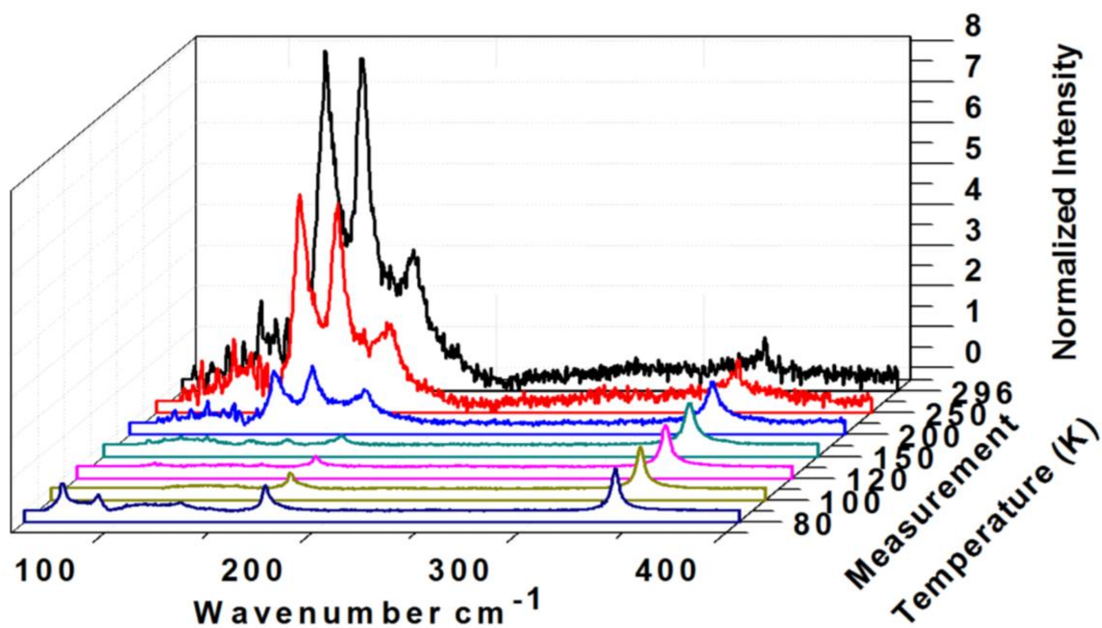

Figure 102. Temperature dependent Raman spectra of CT9-2-AN20.

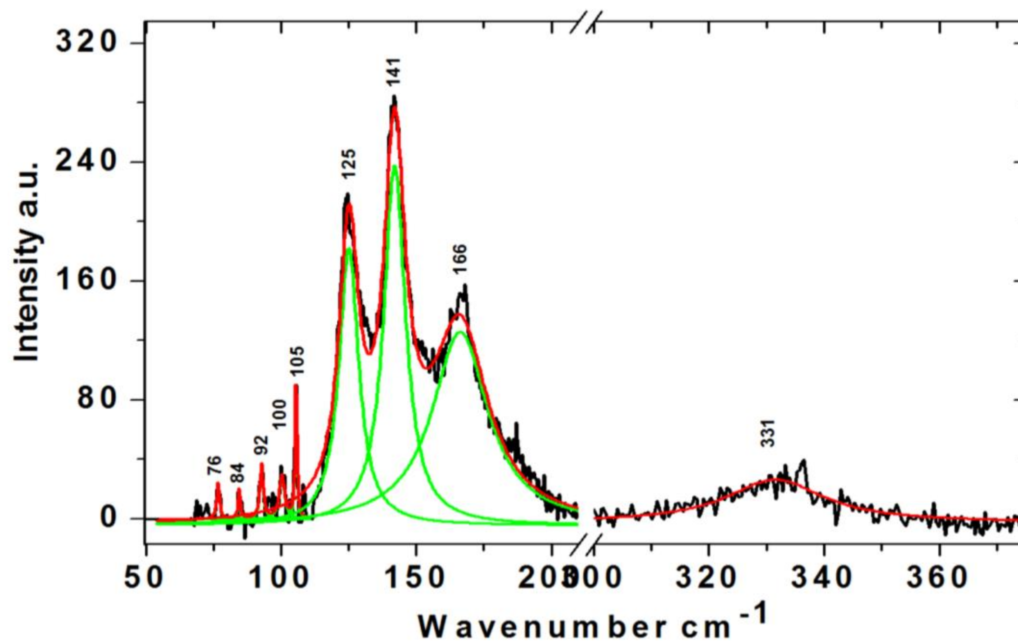

Figure 103. Raman spectrum ofCT9-2-AN21 at 296 K.

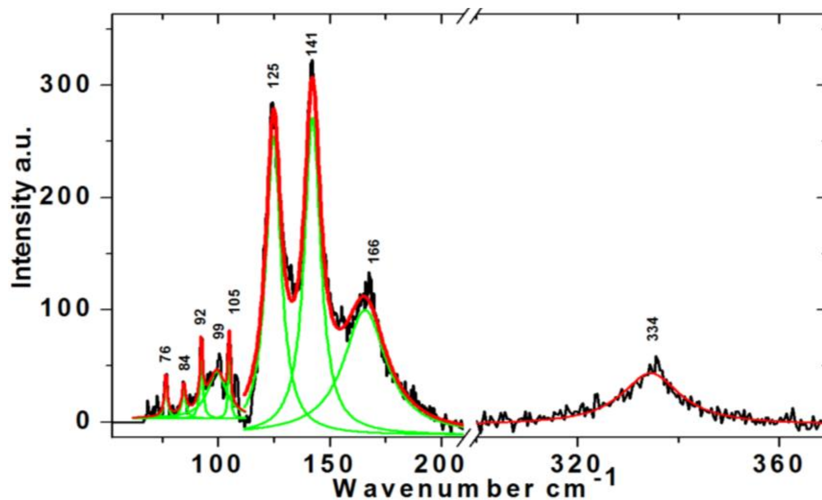

Figure 104. Raman spectrum ofCT9-2-AN21 at 250 K.

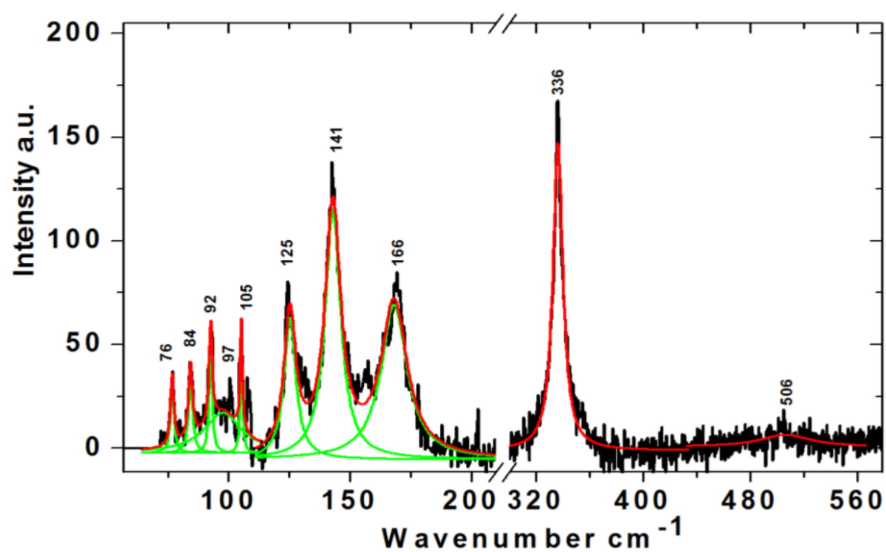

Figure 105. Raman spectrum ofCT9-2-AN21 at 200 K.

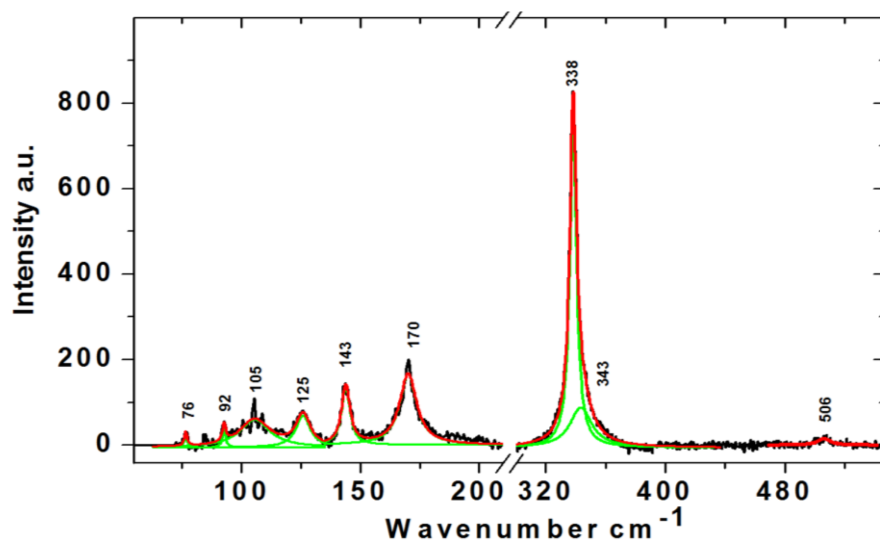

Figure 106. Raman spectrum ofCT9-2-AN21 at 150 K.

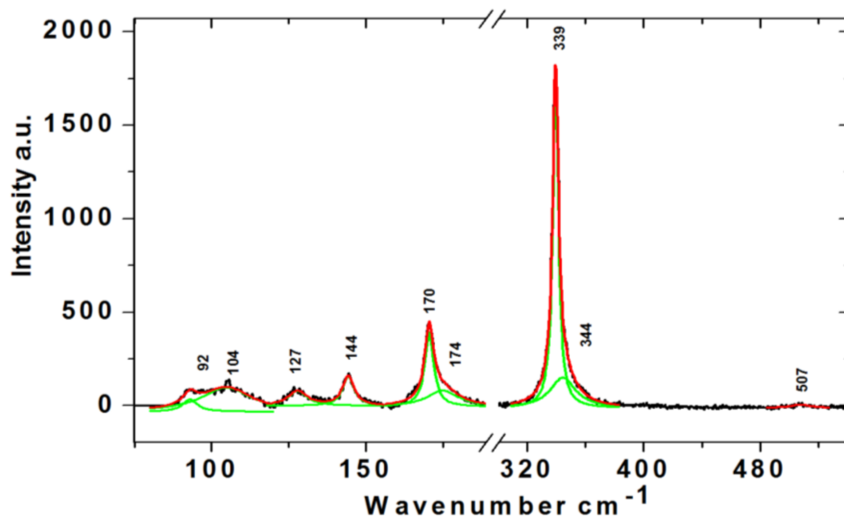

Figure 107. Raman spectrum ofCT9-2-AN21 at 120 K.

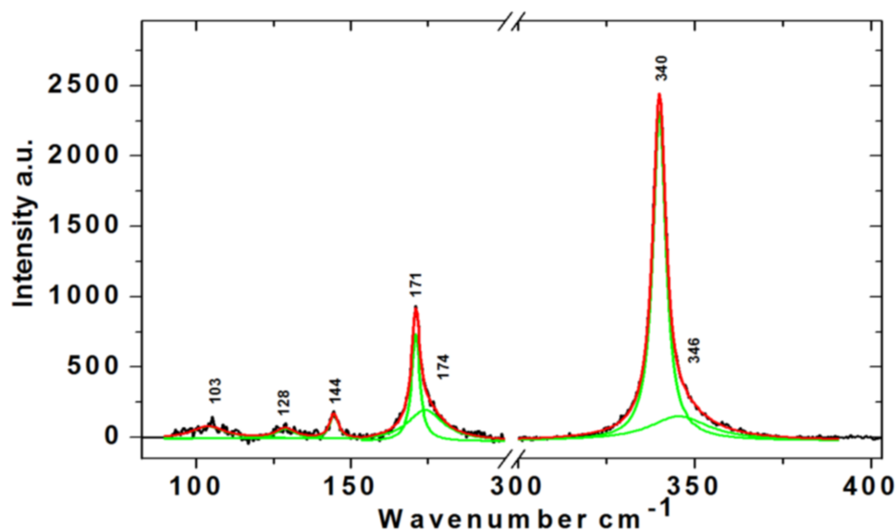

Figure 108. Raman spectrum ofCT9-2-AN21 at 100 K.

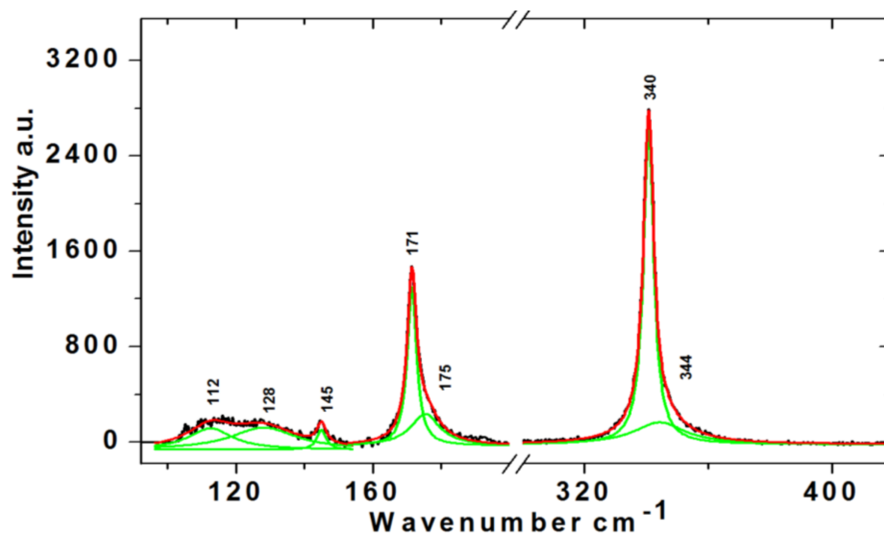

Figure 109. Raman spectrum ofCT9-2-AN21 at 80 K.

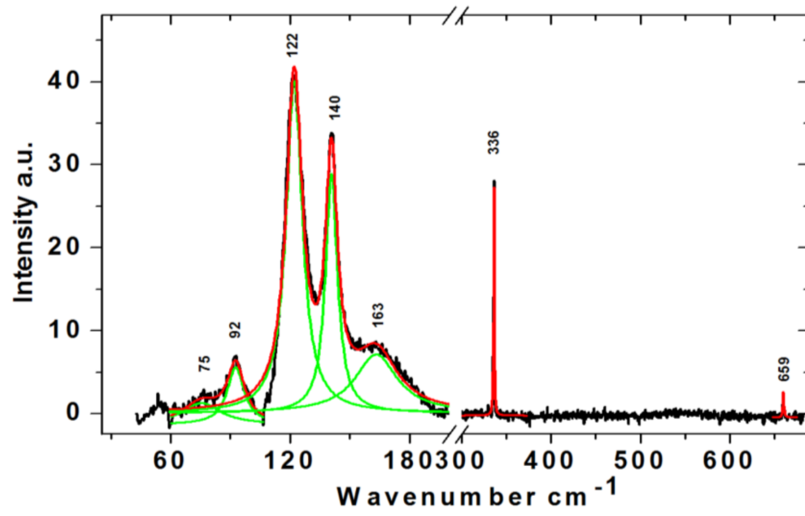

Figure 110. Raman spectrum ofCT9-2-AN30 at 296 K.

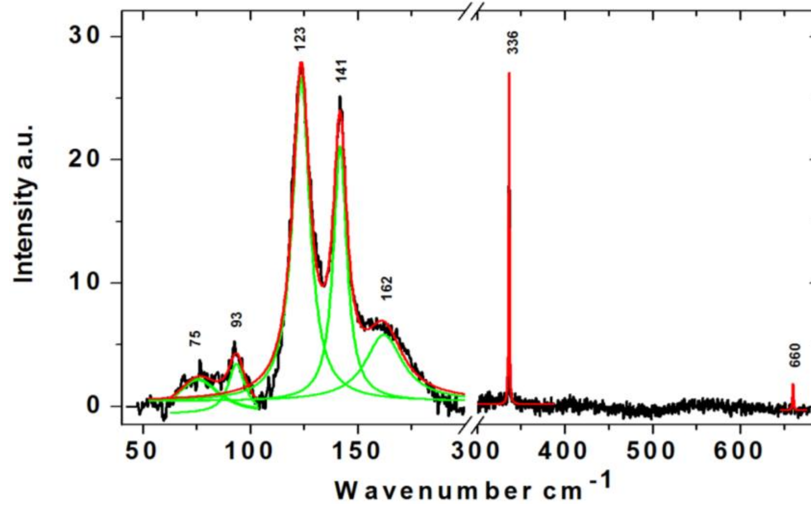

Figure 111. Raman spectrum ofCT9-2-AN30 at 250 K.

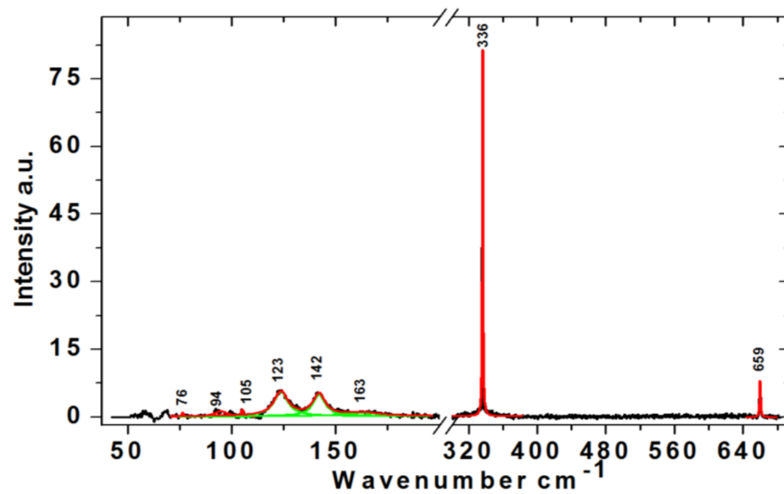

Figure 112. Raman spectrum ofCT9-2-AN30 at 200 K.

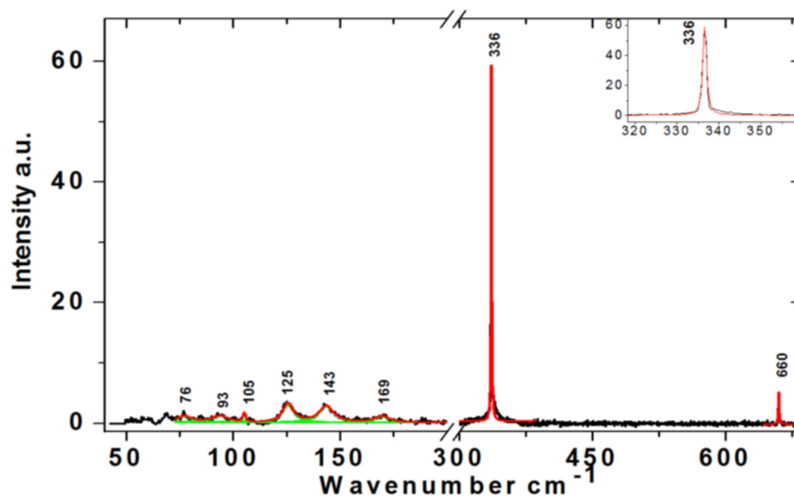

Figure 113. Raman spectrum ofCT9-2-AN30 at 150 K.

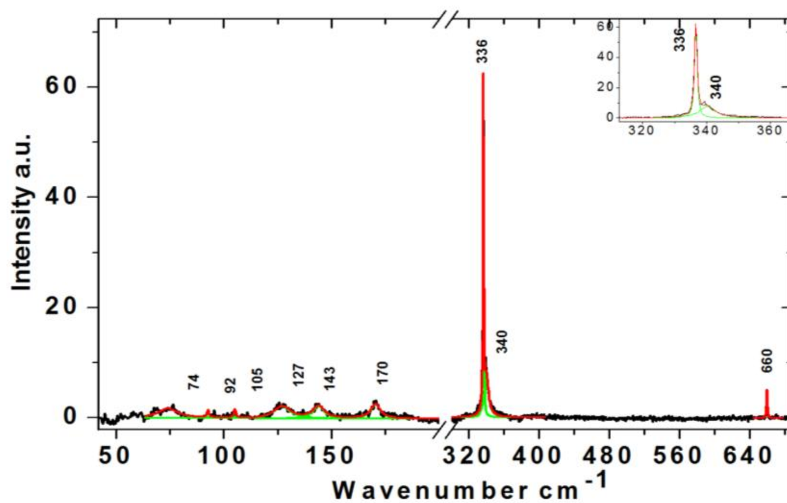

Figure 114. Raman spectrum ofCT9-2-AN30 at 120 K.

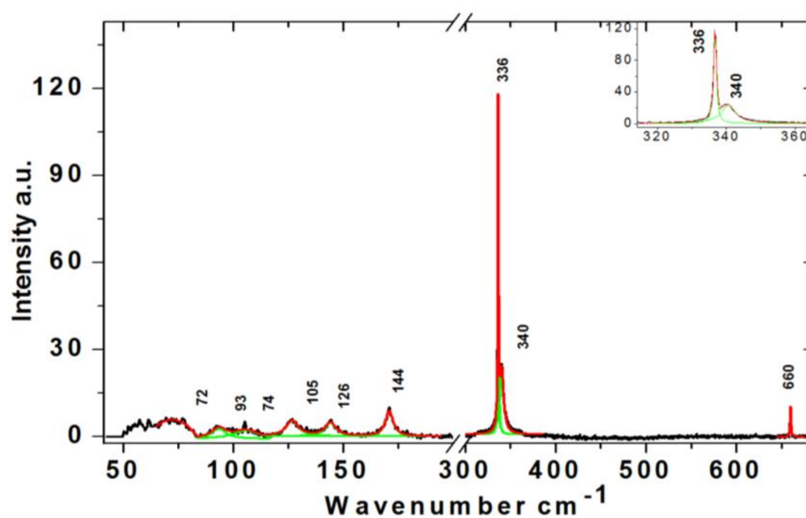

Figure 115. Raman spectrum ofCT9-2-AN30 at 100 K.

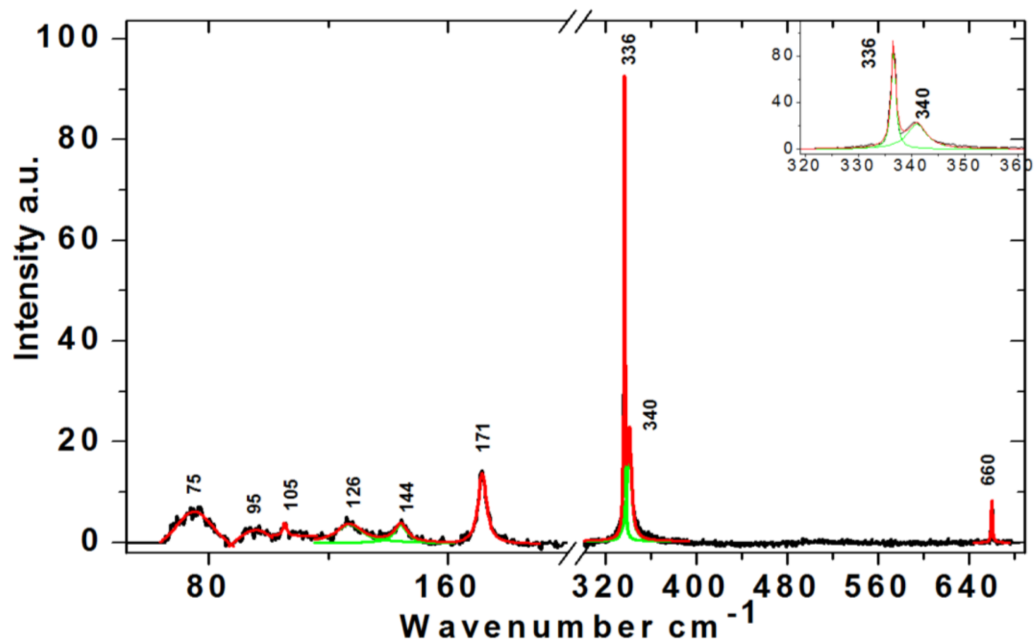

Figure 116. Raman spectrum ofCT9-2-AN30 at 80 K.

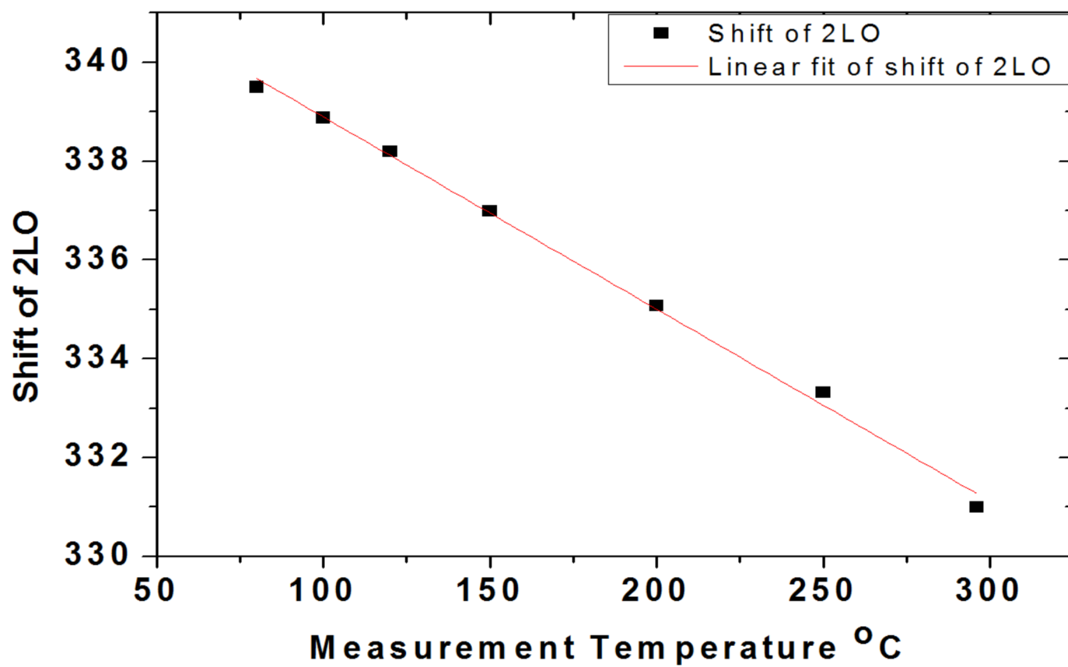

Figure 117. Raman Shift of 2LO mode of CT9-2-AN14.